A DIAGNOSTIC STUDY OF A MIDLATITUDE FRONTAL SQUALL LINE

Xin Lin

Colorado State University

DEPARTMENT OF ATMOSPHERIC SCIENCE

PAPER NO. 510

A DIAGNOSTIC STUDY OF A MIDLATITUDE FRONTAL SQUALL LINE

by

Xin Lin

Department of Atmospheric Science
Colorado State University
Fort Collins, CO 80523

Fall 1992

Atmospheric Science Paper No. 510

ABSTRACT

A DIAGNOSTIC STUDY OF A MIDLATITUDE FRONTAL SQUALL LINE

Heat, moisture and momentum budgets of a squall line that occurred in the central United States on 26-27 June 1985 are investigated throughout its developing, mature and dissipating stages. The slow propagating behavior of the squall line made the 26-27 June data set unique since it covers a large fraction of the squall line life cycle, much longer than previous diagnostic studies. Budget studies have been performed at six different times at time intervals of 90 minutes using OK PRE-STORM (Oklahoma-Kansas Preliminary Regional Experiment for STORM-Central) rawinsonde data. Secondary circulation forcing and frontogenetical/frontolytical effects are also computed to evaluate the importance of diabatic effects using diagnosed heating/cooling distributions.

The squall line was followed by a low-level cold front and was characterized by a narrow stratiform region and an intermediate asymmetric feature during the early stages. The flow pattern normal to the line was generally similar to previous squall line studies except that a low-level rear inflow associated with the cold front was superimposed upon expected squall line FTR/RTF (front to rear/rear to front) flows. The midlevel RTF flow was quite weak well behind the squall line during the developing and mature stages and significantly strengthened during the dissipating stage, suggesting that the stratiform region plays an important role in RTF flow development.

A convergence band resulting from system RTF and FTR flows extended rearward from low levels near the leading edge up to the rear of the system. During the developing and mature stages, peak convergence was located at low levels around the leading edge. At the dissipating stage, midlevel convergence behind the convective region intensified as

stratiform region developed, while low level convergence near the leading edge gradually weakened.

During the developing stage, a narrow vertical band of upward motion corresponding to a narrow convective line was present around the leading edge over Oklahoma. Moderately strong compensating downward motion occurred behind and ahead of the system. A wide band of upward motion was noticed over Kansas where stratiform and convective regions co-existed. The squall line became symmetric during its later stages. A low-level mesoscale downdraft developed as the stratiform region developed. Weak convergence and downward motion took place near tropospause above the squall line system.

Both Q_1 and Q_2 showed tilted structure when the stratiform region developed, as did the ω field. Distinct profiles are found for the convective and stratiform regions respectively, similar to previous diagnostic results. The system-averaged heating peak Q_1 was located at middle levels between 500 and 550 hPa throughout the evolution, much lower than the 10-11 June case. The moisture sink Q_2 clearly showed the evolutional contribution from the convective and stratiform regions at different stages. A single drying peak, which resulted from the convective region, was evident at low levels around 700 hPa through most of the developing and early mature stages. Midlevel drying feature during the early stages may probably be induced by two possible mechanisms: (1) midlevel drying generated by the trailing stratiform region, and (2) vertical eddy transport of water vapor within the convective region. During the late mature and dissipating stages, a double-peak structure became very pronounced, suggesting that mixture of convective and stratiform drying may be the causal mechanism at these stages. At later stage, a single drying peak resulting from the stratiform region was present at middle levels around 475 hPa.

During the developing and mature stages, the squall line had little effect on the geopotential height field. At the late mature and dissipating stages, a pronounced mesoscale low was present within the stratiform region. It was also followed by a mesohigh. The couplet of the mesolow and mesohigh may explain most of the dramatic strengthening of the rear inflow at the back edge of the squall line during the dissipating stage. In the convective region, the line-normal momentum flux was generally negative, along with negative wind

shear present above 600 hPa, the momentum flux transport was upgradient throughout most of its evolution, consistent with other studies. In the stratiform region during the dissipating stage, the momentum flux became positive and the flux transport appeared to be downgradient.

The contribution of diabatic heating/cooling effect to secondary circulation forcing and frontogenetical/frontolytical effects is investigated using diagnosed Q_1 data. Different from "dry convection" cases, the contribution of the diabatic effect to secondary circulation forcing above the low-level cold front within the system was one order of magnitude larger than the geostrophic stretching deformation and geostrophic shearing deformation terms, suggesting the important role the diabatic effect played in mesoscale circulation at middle and upper levels. At low levels around the cold front, the three terms contributed nearly equally to the forcing. In the frontogenesis equation, although the differential diabatic effect was one order of magnitude larger than the confluence term above the front, it was strongly opposed by the tilting term. Therefore, although the low-level cold front contributed to triggering the intense convection within the squall line, any feedback to frontogenesis appeared to be small. At low levels during the system developing stage, frontogenetical effect was present around and ahead of the leading edge and frontolytical effect behind. But at the dissipating stage, weak frontogenetical effect only occurred in a small region within the frontal zone, with frontolysis took place ahead and behind. This feature may help to explain why the movement of both the low level cold front and the squall line increased during the early stages and decreased rapidly and almost ceased at the dissipating stage.

ACKNOWLEDGEMENTS

I would like to express my sincere gratitude to my advisor, Professor Richard H. Johnson, for his guidance, encouragement and support during the past two years. Without his invalueable advice and thoughtful comments, the paper would not have been completed. Thanks also goes to my other committee members, Prof. Steven Rutledge and Prof. Bogusz Bienkiewcz.

I would also like to thank my colleagues, James Bresch, William Gallus, Scot Loehrer and Bob Falvey, for many helpful discussions and comments.

Finally, thanks to Gail Cordova for help in the final preperation of the manuscript.

This research was supported by the National Science Foundation, under Grant ATM-9013112.

TABLE OF CONTENTS

LIST OF FIGURES

Chapter 1

INTRODUCTION

Deep convection in tropical areas constitutes the major heat source in the global general circulation, as pointed out by Riehl and Malkus (1958). Observations show that deep convection is usually organized into mesoscale features characterized by groups or bands of convective cloud systems (e.g., Houze 1977; Zipser 1977; Leary and Houze 1979; Johnson 1980; Leary and Houze 1980; Houze and Cheng 1981; Johnson and Young 1983; Gamache and Houze 1982 and 1983; Houze and Rappaport 1984). Within midlatitude storm systems, similar features have also been noticed for a long time (Houze and Hobbs 1982; Houze et al. 1990). Along with the development of techniques of numerical weather prediction, many attempts have been made to delineate the contribution of these mesoscale convective systems to the large scale circulation using large scale observational data.

Since Yanai et al. (1973) proposed the computational methods for Q_1 (the apparent heat source) and Q_2 (the apparent moisture sink), which relate the unresolvable cumulus scale effect to large scale environmental variables, many budget studies have been performed over different parts of the world to study the details of interaction between deep cumulus convection and the large scale environment (e.g., Lewis 1975; Thompson et al. 1979; Johnson and Young 1983; Johnson 1984; Chong et al. 1987; Frank and McBride 1989; Gallus and Johnson 1991; etc).

In the earlier studies, due to temporal and spatial limitations of data, only the collective heating and moistening effects of many MCSs (mesoscale convective systems) were evaluated (Reed and Recker 1971; Nitta 1972a; Yanai et al. 1973). The time and area-averaged heating profiles showed condensational heating throughout the troposphere, representing the sum of both convective scale and mesoscale precipitation components.

With more field experiments, denser sounding networks and more advanced instruments, it was gradually noticed that MCSs could be properly partitioned into a convective region and a stratiform region (Houze 1977; Zipser 1977; Leary and Houze 1979; Houze et al. 1980; Johnson 1980; Leary and Houze 1980; Gamache and Houze 1982; Houze 1982; Johnson 1984).

The vertical heating and moistening profiles display distinct differences between the convective region and the stratiform region. As Houze (1982) pointed out, the total effect of the stratiform precipitation processes on the large-scale budget is heating of the middle to upper troposphere, where latent heating in the mesoscale updrafts is the dominant effect, and cooling in the lower troposphere, where melting and mesoscale downdraft evaporation dominate. Johnson and Young (1983), using Winter MONEX sounding data, calculated the heat and moisture budgets of tropical mesoscale anvil clouds. They observed that the composite heating profile showed a heating peak in the upper troposphere near 350 hPa and a cooling peak in the lower troposphere near 700 hPa. The heating can be mainly attributed to condensation and deposition in the anvil, while the cooling is due to evaporation and melting. The moisture budget showed a drying maximum in the upper troposphere coincident with the heating peak and a moistening maximum in the lower troposphere near 800 hPa. Many observational studies of tropical and middle latitude cases support their findings although the levels of peak heating and drying are a little different from case to case (Houze 1989; Gallus and Johnson 1991).

Frank and McBride (1989) compared the heating and moistening profiles of cloud clusters in AMEX and GATE. They divided the entire process into five stages: initial, growth, maximum intensity, early decay and late decay. The analyses showed that GATE systems tend to have maximum heating at low levels in their early stages, with the levels of maximum heating rising to the upper troposphere in later stages when convection weakens and stratiform rain becomes dominant. AMEX systems have their maximum heating at middle levels, with small upward shifting of the level of maximum heating throughout the entire process. The difference is hypothesized by Frank and McBride (1989) to be due to stratiform rain forming earlier in the life cycles of the AMEX systems than in the GATE systems.

A number of field experiments have been carried out in tropical and subtropical regions which have provided data for vertical motion, heat and moisture budget studies: the 1974 GARP Atlantic Tropical Experiment (GATE), the 1979 Monsoon Experiment (MONEX), the 1987 Australia Monsoon Experiment (AMEX), the 1987 Equatorial Mesoscale Experiment (EMEX), the 1987 Taiwan Area Mesoscale Experiment (TAMEX), and the 1988-1990 Down Under Doppler and Electricity Experiment (DUNDEE). Field experiments enabling such studies at midlatitudes have been fewer in number (e.g. the 1979 Atmospheric Variability Experiment – Severe Environmental Storm and Mesoscale Experiment). The 1985 OK PRE-STORM (Oklahoma-Kansas Preliminary Regional Experiment for STORM-Central) experiment (Cunning 1986) provided a valuable dataset to allow extensive studies of middle latitude mesoscale convective systems.

Squall line systems, as one common type of mesoscale convective systems in both tropics and midlatitudes, receive much attention. This is because the structure of squall lines is usually relatively simple and regular compared to other types of MCS (Houze et al. 1990). Some squall lines are highly two-dimensional, which is much conducive to 2-D modeling studies and may provide a good reference comparison. Most squall line cases consist of convective and stratiform regions. The convective region, characterized by strong vertical motion throughout the troposphere and intense convective rain, is usually located at the leading edge of the mesoscale convective system and is about 30 $\sim$ 50 km wide. The stratiform region, also called the mesoscale anvil (Brown 1979), usually defined as widespread cloud trailing the convective region of a squall line and extending from near the melting level to the upper troposphere, is characterized by light, continuous stratiform precipitation. However, its width may vary from case to case. Some squall lines also exhibited leading anvil structures.

Rutledge et al. (1988), using single-Dopplar radar data, studied the 10-11 June PRE-STORM squall line. Their analysis showed four contrasting airflows within the squall line: a surface front-to-rear flow behind the leading edge, a rear-to-front inflow at midlevels sloping down to the surface at the leading edge, a front-to-rear flow originating at low levels in front of the leading edge and extending to the upper levels in the stratiform region and a rear-to-front flow at upper levels of the convective region driven by divergence. This structure is similar to those found in tropical cases, although the system rear inflows were a little stronger in the midlatitude case.

Gallus and Johnson (1991) did a comprehensive heat and moisture budget analysis during the late mature through the dissipating stages of the 10-11 June PRE-STORM case. This intense midlatitude squall line was characterized by a fast propagation speed and an extensive stratiform region. The convective region and the stratiform region were quite well resolved compared to other budget studies. They found that the Q_1 distribution had heating peaks between 300 and 400 hPa in the convective and stratiform regions. Cooling in the stratiform region was most intense just behind the back edge of stratiform echo around 550 hPa. The drying effect peaked at lower levels than the heat source in the convective region, and moistening was most intense around 700 hPa in the stratiform region. The magnitudes of ascent and descent in the stratiform region weakened and the axes became increasingly sloped over time from the late mature to the dissipating stages, as did the heat source and moisture sink. Precipitation rates calculated from the integration of heat and moisture budgets yielded results in reasonable agreement to the observed rates. However, due to the fast moving character of the MCS, the squall line remained within the PRE-STORM sounding network only for a short time and only the late mature to decaying stages were studied.

In the past, although many studies have been performed on the heat and moisture budgets of tropical and midlatitude convective systems, research done on the systems' momentum budget from a dynamical view point was not common. One of the main reasons was the existence of large observational errors and coarse resolution of mesoscale rawinsondes. The errors may produce unreliable results when calculating the pressure gradient force (Fankhauser 1974), which always plays an important role in the system evolution.

Sanders and Emanuel (1977) first used mesoscale rawinsonde data to study a momentum budget of a middle latitude squall line. The pressure gradient force was obtained as a residual and compared to the results calculated hydrostatically from real geopotential height data. Good agreement was found, indicating the reliability of the pressure gradient force calculated directly from geopotential height data. By comparing each momentum budget component within the system normal to the squall line, they found cumulus eddy flux transports to be as large as the pressure gradient force and generally opposing each other during the system evolution.

LeMone (1983), using aircraft data, investigated the momentum budget of a line of tropical cumulonimbi. The vertical transport of horizontal momentum normal to the squall line was found to be countergradient and tended to increase the vertical shear of the horizontal wind during evolution, contrary to the predictions of mixing-length theory. But the vertical transport of horizontal momentum parallel to the line was downgradient.

Smull and Houze (1987) and Lin et al. (1990) using dual-Dopplar radar data studied an Oklahoma squall line and a subtropical squall line during TAMEX, respectively. Both of their results supported LeMone's finding that the vertical transports of horizontal momentum normal to the squall line tended to increase vertical shear of the horizontal wind.

Another squall line momentum budget using dense mesoscale rawinsonde sounding data during PRE-STORM was performed by Gallus and Johnson (1992). They noticed that strong front-to-rear pressure gradient acceleration resulted from a mesolow existing at middle levels within the stratiform region of the system. By studying the evolution of the pressure gradient force, Coriolis force, acceleration term and turbulent transport term, they found that the turbulent stress term generally opposed the large pressure gradient acceleration and was responsible for most rear-to-front acceleration in the convective region. In the stratiform region, the balance within the system was maintained by the pressure gradient force and Coriolis acceleration during the dissipating stage. Both line-normal and along-line momentum fluxes were found to be countergradient within the squall line.

Most of the previous squall line budget studies were performed either over large temporal and spatial scales or at a specific stage of the system evolution. Studies on the longer period of a life cycle of a squall line are quite rare. On 26-27 June 1985 during the PRE-STORM experiment, a squall line followed by a low-level cold front passed through the PRE-STORM network. It was characterized by slow movement and exhibited evolutional features from the developing and mature to the dissipating stages within the network. Compared with other midlatitude budget studies (Lewis, 1975; Sanders and Paine 1975; Fritsch et al. 1976; McNab and Betts 1978; Ogura and Chen 1977), it provided a much more complete data set over the life cycle of a MCS. This squall line showed a complicated three-dimensional intermediate asymmetric pattern (Manning, 1991) and demonstrated both similar and different environmental conditions and structural features compared to many previously observed cases and idealized simulations of linearly oriented MCSs. Moreover, the low-level cold front following the convective system may have imposed important forcing effects on the evolution of this long-lived squall line system (Trier et al. 1991).

In this study, heat, moisture and momentum budget analyses have been performed at six different times for the 26-27 June MCS. Particular emphasis will be placed on the spatial and temporal evolution of mesoscale heating, moistening, and the force balance within the squall line from the developing and mature, to the dissipating stages, and on the interaction between the low-level cold front and the squall line system. Attention will also be given to the comparison of the vertical heating and moistening profiles with other tropical and midlatitude squall line systems in terms of the positions and magnitudes of the heating and moistening peaks. The budget-integrated rainfall rates at each time will also be compared with observed surface rainfall rates to check the validity of the budgets.

Chapter 2

BUDGET EQUATIONS

2.1 Heat and moisture budget equations

Budget equations for Q_1 (the apparent heat source) and Q_2 (the apparent moisture sink) (Yanai et al. 1973), with modifications to account for ice effects (Gallus and Johnson 1991), are defined by:

$$\begin{aligned} Q_1 \equiv \frac{\partial \bar{s}}{\partial t} + \bar{\mathbf{v}} \cdot \nabla \bar{s} + \bar{\omega} \frac{\partial \bar{s}}{\partial p} = \quad & Q_R + L_v(\bar{c} - \bar{e}) + (L_v + L_f)(\bar{d} - \bar{s_*}) \\ & + L_f(\bar{f} - \bar{m}) - \nabla \cdot \overline{s'\mathbf{v}'} - \frac{\partial}{\partial p}\overline{s'\omega'} \end{aligned} \tag{2.1}$$

$$\begin{aligned} Q_2 \equiv -L_v \left(\frac{\partial \bar{q}}{\partial t} + \bar{\mathbf{v}} \cdot \nabla \bar{q} + \bar{\omega} \frac{\partial \bar{q}}{\partial p} \right) = \quad & L_v(\bar{c} - \bar{e}) + L_v(\bar{d} - \bar{s_*}) + \\ & L_v \nabla \cdot \overline{q'\mathbf{v}'} + L_v \frac{\partial}{\partial p}\overline{q'\omega'} \end{aligned} \tag{2.2}$$

where s=c_pT+gz is the dry static energy; q the specific humidity; Q_R the radiative heating rate; L_v and L_f the latent heats of vaporization and fusion; c, e, d, s_*, f and m the condensation, evaporation, deposition, sublimation, freezing and melting rates, respectively. The overbars refer to roughly 50 km × 50 km area averages, where primes denote sub-grid deviations from the horizontal area average. Q_1 is a measure of radiative heating, latent heating from net condensation and ice phase changes, and the convergences of the vertical and horizontal eddy transports of sensible heat. Although the horizontal eddy flux is usually neglected in large scale budget studies, it may be important in budget studies of squall lines (Gallus and Johnson 1991). Rutledge and Houze (1987) found in their diagnostic modeling study that the hydrometeor transport from the convective region into the stratiform region may account for 20 % of the precipitation in the stratiform region, and also more importantly, the 20 % account the other 80 % to fallout, which suggests the possible importance of horizontal eddy transport. However, there is no method to directly assess the importance of this term. Similarly, Q_2 is a measure of the net condensation and the horizontal and vertical convergences of the eddy moisture transports.

Integration of Eqs. (2.1) and (2.2) from p_T (cloud top pressure) to p_s (surface pressure) gives the precipitation rates P_0 diagnosed from the heat and moisture budgets (Yanai et al. 1973). Integration of (2.1) gives:

$$\begin{aligned} P_0 = \; & \frac{1}{gL_v}\int_{p_T}^{p_s}(Q_1 - Q_R)dp - \frac{(L_v + L_f)}{gL_v}\int_{p_T}^{p_s}(\bar{d} - \bar{s_*})dp \\ & + \frac{1}{gL_v}\int_{p_T}^{p_s}\nabla\cdot\overline{s'\mathbf{v}'}dp - \frac{L_f}{gL_v}\int_{p_T}^{p_s}(\bar{f} - \bar{m})dp - \frac{S_0}{L_v} \end{aligned} \tag{2.3}$$

and (2.2) gives:

$$\begin{aligned} P_0 = \; & \frac{1}{gL_v}\int_{p_T}^{p_s}Q_2 dp - \frac{1}{g}\int_{p_T}^{p_s}(\bar{d} - \bar{s_*})dp \\ & + \frac{1}{g}\int_{p_T}^{p_s}\nabla\cdot\overline{q'\mathbf{v}'}dp + E_0 \end{aligned} \tag{2.4}$$

where the second and the third terms on the right-hand side of each equation represent water production by net deposition and the net convergence of the horizontal eddy flux, respectively. They are usually considered to be small in budget studies due to possible large cancellation within the integrating volume. The fourth term in Eq. (2.3), which represents the net melting effect in the volume, is also considered to be small. Since there is a long time sequence of data in this case, the surface sensible heat flux term S_0 and surface evaporation term E_0 could be large during the afternoon (2100 to 0000 UTC). Unfortunately, they could not be obtained from available data. However, due to large cloud cover during these times, these two surface terms might be small and will be neglected. The two terms should be small for midlatitude convection at night (Gallus and

Johnson 1991) from 0130 to 0430 UTC and can be neglected compared with the large magnitudes obtained from the integration of Q_1 and Q_2.

A more general form of the precipitation rate can be written as:

$$P = P_Q + P_x + P_\sigma \tag{2.5}$$

where P represents the actual rainfall rate; P_Q the rainfall rate calculated from the volume integration of Q_1 or Q_2, which can be directly diagnosed from large scale data; P_x the combination of volume integrations of net ice phase changes, convergence terms of horizontal eddy flux and surface terms, which can not be determined directly from conventional sounding data; and P_σ the errors resulting from data grid selection, smoothing scheme, distribution of sounding stations and hydrometer storage, etc. The discrepancy between P (the actual precipitation rate) and P_Q (the calculated precipitation rate) can be explained by the temporal and spatial variation of $(P_x + P_\sigma)$.

2.2 Momentum budget equation

The momentum budget, similar to the work done by Sanders and Emanuel (1977) and Gallus and Johnson (1992), will focus on the evolution of the components of the wind normal to the squall line.

The momentum budget equation (Sanders and Emanuel 1977) is given by:

$$\bar{X} \equiv \frac{\partial \bar{u}}{\partial t} + \bar{u}\frac{\partial \bar{u}}{\partial x} + \bar{v}\frac{\partial \bar{u}}{\partial y} + \bar{\omega}\frac{\partial \bar{u}}{\partial p} + \frac{\partial \bar{\phi}}{\partial x} - f\bar{v} = -\frac{\partial}{\partial p}\overline{(\omega' u')} \tag{2.6}$$

The acceleration term, pressure gradient force, and Coriolis force are calculated using gridded data of height and wind velocity, while the turbulent force is determined as a residual, $\bar{X}$. Those terms normal to the squall line are evaluated to investigate their temporal and spatial evolution.

2.3 Computational methods

Spatial and temporal derivatives are calculated using a finite centered difference method. Vertical velocities are calculated by integrating the mass continuity equation. Due to errors resulting from wind measurements, the divergence calculation has large accumulated errors in the upper troposphere. A method proposed by O'Brien (1970) is used to adjust the vertical distribution of divergence and vertical velocity and make them satisfy continuity for the whole volume. Vertical velocities at the surface (975 hPa) and at the top (125 hPa) are set to zero. In their study of the 10-11 June 1985 case, Gallus and Johnson (1991) found that the influence of the topography on the calculation of the vertical velocity in the PRE-STORM area is very small and can be neglected when compared to the large magnitudes of the updraft and downdraft within the squall line system. Hence, topography is not considered in computing the vertical velocity in this case.

Chapter 3

DATA AND ANALYSIS METHODS

3.1 The PRE-STORM field experiment

During May and June of 1985, the Oklahoma-Kansas Preliminary Regional experiment for STORM-Central was performed over the Great Plains. One of its main objectives was to examine the detailed structure of midlatitude mesoscale convective systems occurring over the central U.S, which usually have large contributions to the annual precipitation in this region. The PRE-STORM observational mesonetwork is illustrated in Figure 3.1. Abundant data from various facilities, including NWS rawinsondes, supplemental rawinsondes, surface mesonets, radars and wind profilers, were collected.

3.2 Upper air data and compositing technique

In this study, PRE-STORM rawinsonde data from the NWS and supplemental sounding stations were extensively used to perform heat, moisture and momentum budget calculations from 2100 UTC 26 June to 0430 UTC 27 June at intervals of 90 minutes.

There are eight rawinsonde-release times at 90-min intervals used in this case. In order to decrease data spacing and better resolve the structural details of the squall line, a compositing technique was used in the budget calculations over three-hour periods centered at six different times (1930, 2100, 2230, 0000, 0130, 0300 UTC) ranging from the developing and mature to the dissipating stages. Under the assumption of a quasi-steady state squall line over 3-h intervals, the data at different times for one station can be moved

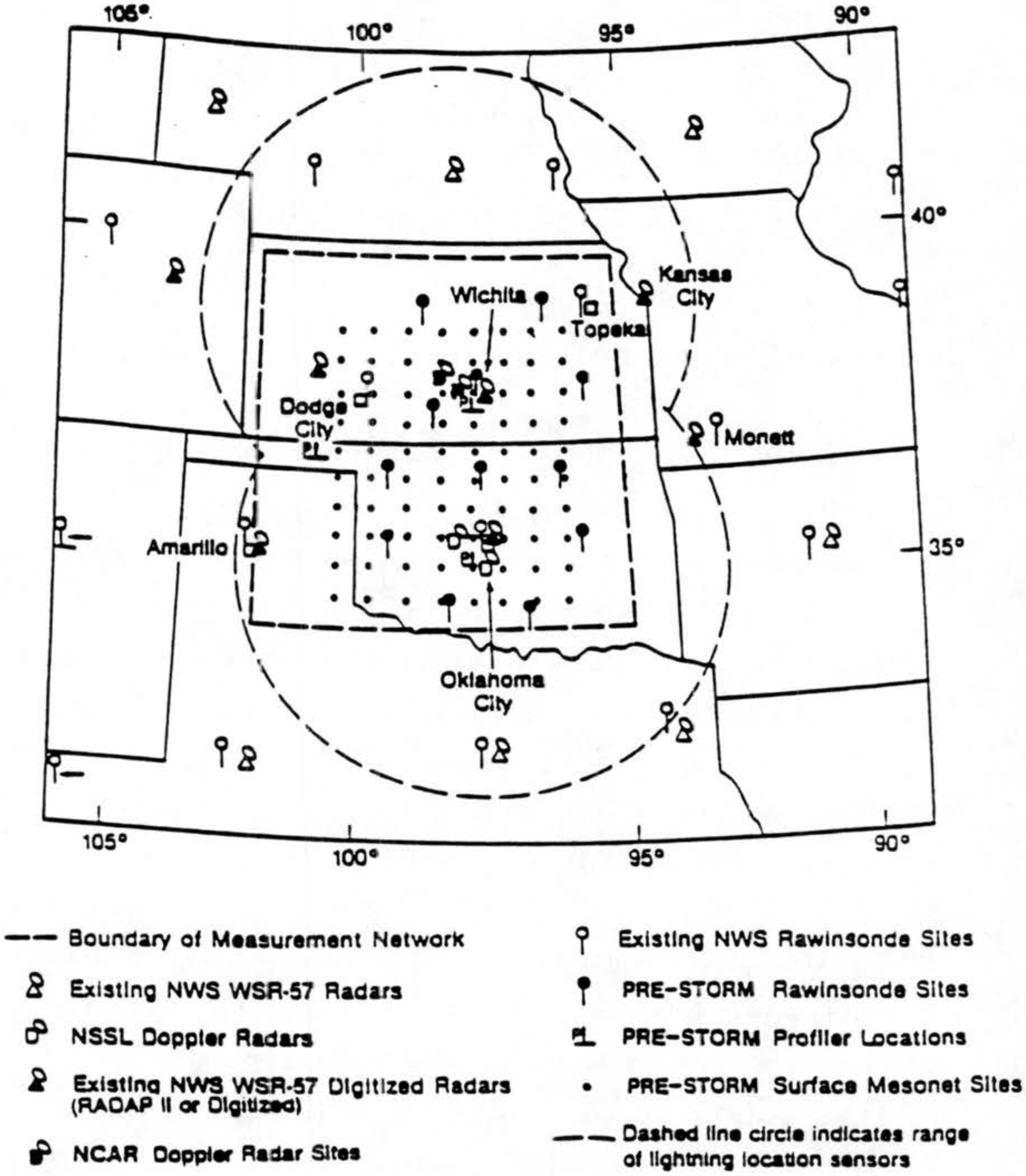

Figure 3.1: The OK PRE-STORM observational mesonetwork (from Cunning, 1986).

a distance ahead of or behind the actual position at centered times according to the average propagation speed of the system. Thus, data at different times can be incorporated into a specific time with more sounding data available for the budget study. The method to determine the estimated propagation speeds of the squall line is similar to that of Gallus and Johnson (1991). They found that the best velocity to use for compositing over the entire PRE-STORM region was the average movement of the central axis, leading edge, and back edge of the radar echo over each three hour period. The reason is that the movement of the stratiform region is usually slower than that of convective region. Figures 3.2a, b and c show the positions of the leading edge, back edge and central axis at eight different times based on low-level radar reflectivity data from Wichita, KS, and Oklahoma City, OK. It is noticed that although the leading edge and the back edge were not very regular, they both moved south-eastward. The movement of the leading edge over Oklahoma was faster than that over Kansas, while the speed of the back edge was almost the same over the two regions. Fig. 3.2c clearly shows that the propagation speed of the central axis gradually increased during the developing and mature stages and then rapidly decreased in the dissipating stage.

Table 3.1 presents the average direction and speed of movement of the squall line system at eight different times over Kansas and Oklahoma. From 1930 to 2230 UTC, the average direction of the squall line was towards 132° and the average speed was about 5.0 m s^{-1} over Kansas and 7.0 m s^{-1} over Oklahoma. The speed gradually increased from 0000 to 0130 UTC. The maximum propagation speed was found at 0130 UTC. Over Kansas the average speed was 6.3 m s^{-1}, whereas over Oklahoma it was 8.6 m s^{-1}. The average movement of the squall line system during the mature stage in this case is smaller than that of the 10-11 June squall line which had an average speed of 14 m s^{-1} from the mature to the dissipating stages (Rutledge et al. 1988; Gallus and Johnson 1991). Although the 26-27 June squall line underwent a three-dimensional, asymmetric evolution from the developing and mature to the dissipating stages, the relatively brief three-hour interval used for compositing is assumed to adequately satisfy the assumption of steady state. The speed of the system decreased rapidly during the dissipating stage from about

THE LEADING EDGE

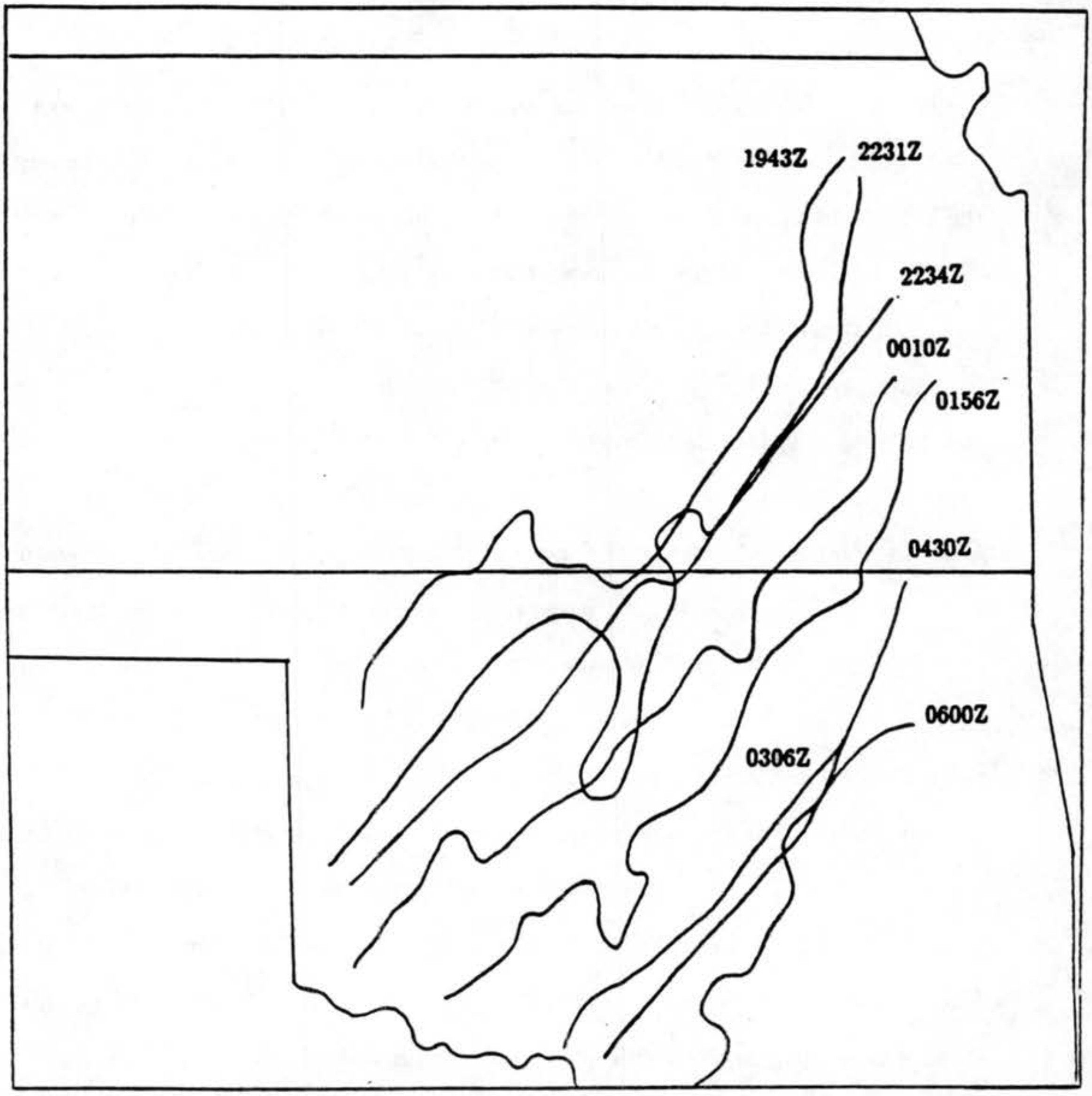

Figure 3.2: The positions of the leading edge, back edge and central axis determined from low-level radar echo at eight different times. a) the leading edge, b) the back edge, c) the central axis.

THE BACK EDGE

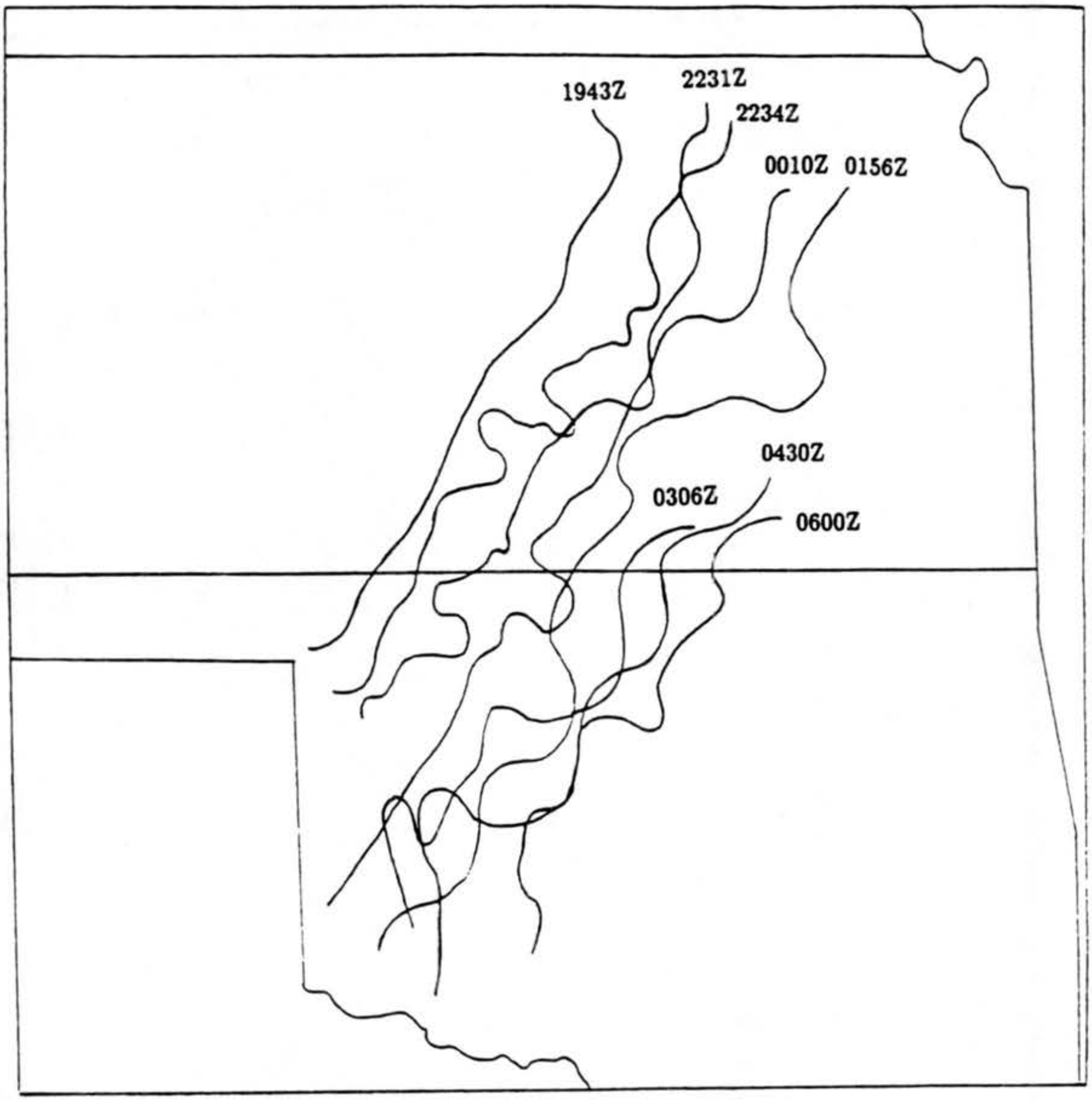

Figure 3.2: Continued.

THE CENTRAL AXIS

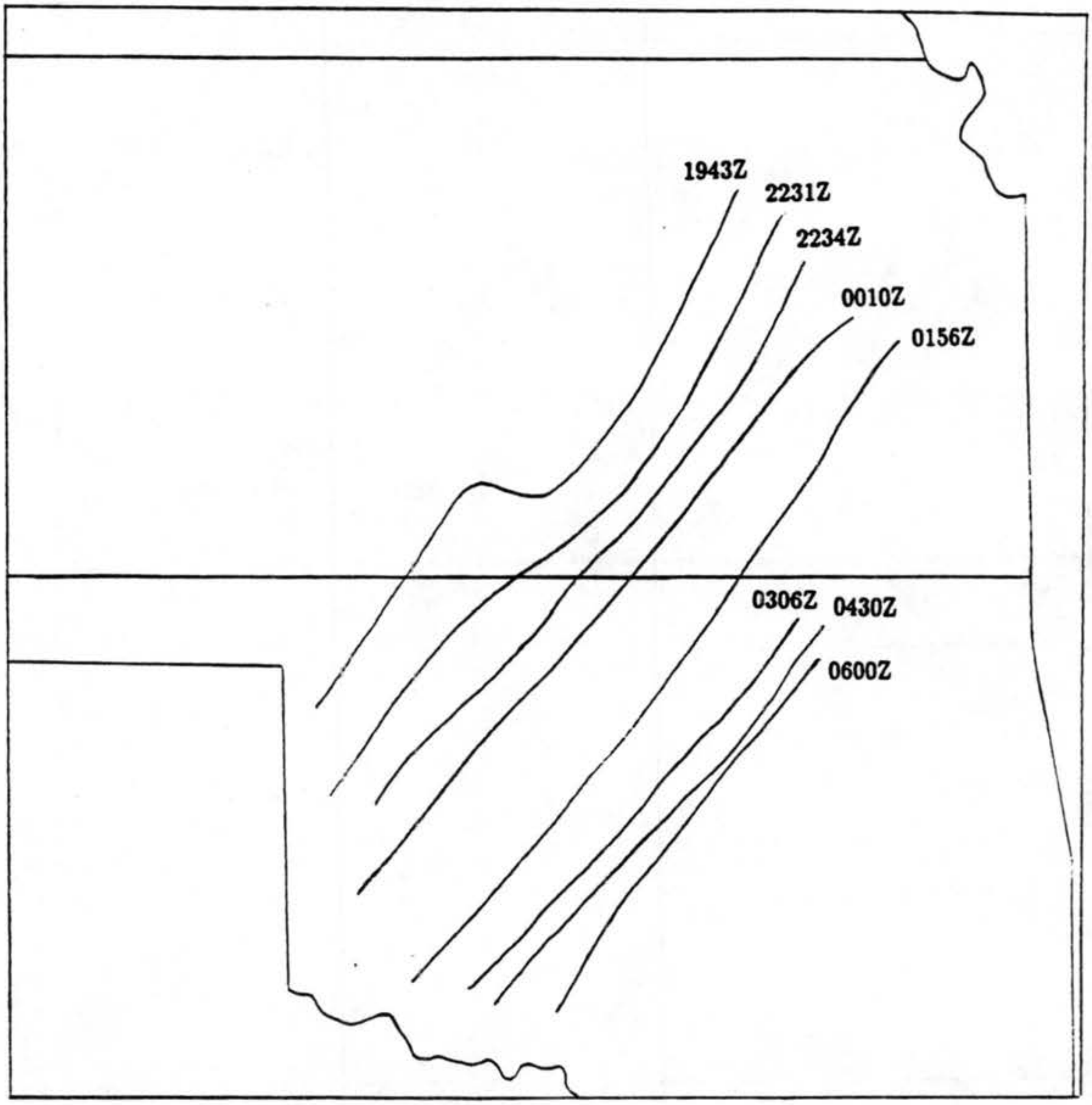

Figure 3.2: Continued.

5.0 m s^{-1} at 0300 UTC to 3.4 m s^{-1} at 0430 UTC and 1.0 m s^{-1} at 0600 UTC. Due to the character of stagnant movement at 0430 and 0600 UTC, the compositing technique was not appropriate to be applied at these two times due to potentially unrealistic strong gradients in the analyzed fields.

Time	Direction	Moving Speed (m s^{-1})	
		Kansas	Oklahoma
1930 Z	132°	4.6	7.0
2100 Z	132°	4.5	7.5
2230 Z	132°	5.5	7.2
0000 Z	132°	5.8	8.0
0130 Z	132°	6.3	8.6
0300 Z	132°	5.0	6.0
0430 Z	130°	3.4	3.4
0600 Z	130°	1.0	1.0

Table 3.1: The average direction and speed of movement of the 26-27 June squall line.

The sounding stations within the PRE-STORM rawinsonde network have an average spacing of about 160 km from each other (See Fig. 3.1). After the compositing technique was applied, the average spacing between stations decreased and the total number of sounding stations available for objective analysis at individual times increased from about fifteen to more than thirty except at 0430 and 0600 UTC. Although Barnes and Sieckman (1984) defined slow-moving squall lines as having speeds < 3 m s^{-1} and fast-moving squall lines as having speeds > 7 m s^{-1}, the 26-27 June squall line is considered as a slow-moving line compared with many previously studied fast-moving cases generally having average propagation speeds exceeding 10 m s^{-1}. This slow propagating feature made the 26-27 June data set unique due to the long sequence of data within the PRE-STORM sounding network from the developing and mature to the dissipating stages. Most of the previous diagnostic studies relating the role of heating and moistening of squall lines to the large scale environment were based on sounding data at a specific stage of the system. Due to the limitation of sounding coverage and number of sounding stations, usually only one or two times were studied. In this budget study, with the advantage of a much longer sequence of data, particular attention will be given to the temporal and spatial evolution of the squall line system.

3.3 Treatment of upper air data

For this budget analysis, sounding data were vertically interpolated from 975 hPa to 125 hPa at intervals of 25 hPa. Smaller vertical intervals were tested and yielded similar budget results. Hydrostatic and horizontal checks were performed to eliminate erroneous sounding data. The PRE-STORM region slopes downward from west to east and the lower pressure levels usually intersected the surface. To compensate for terrain effects and not cause large gradients near the surface in the budget calculations, u, v wind components and the specific humidity data at pressure levels underground are assigned values the same as the values at the surface. The values and their derivatives or derived variables underground at grid points are set to zero during budget integrations. For stations at higher elevations above 975 hPa, height and temperature are interpolated from other data points during the objective analysis, while for stations at relative low elevation above 975 hPa, temperature were equal to the surface value at each pressure level underground and height data were determined by applying the hypsometric equation. Balloon drift was also considered during data processing. A 1-2-1 smoothing scheme was used to filter out small scale disturbances in the vertical.

3.4 Objective analysis

The domain selected in the budget study is from 94°W to 102°W and from 33°N to 40°N. A Barnes objective analysis scheme (Barnes 1964) in spherical coordinates was used to interpolate the sounding data onto a 0.5° by 0.5° grid. Radar maps showed that from 1930 to 2230 UTC, the entire width of the squall line was about 90 km. The width increased to 110 km from 0000 to 0130 UTC and reached 150 km during the dissipating stage (0300 to 0600 UTC). Due to the slow movement and the narrowness of the squall line, the composited rawinsonde stations were not evenly distributed. The average distances between sounding stations ranged from 50 km to 90 km at lower levels. A filter response of about fifty percent at 100 km was selected at levels below 400 hPa. Due to the missing data at higher levels, the average station spacing increased and the response function was selected to represent a horizontal scale of about 200 km above 400 hPa. Unlike the 10-11 June case which had a 160 km wide trailing stratiform region, both the convective and stratiform regions in the 26-27 June case were about 40 $\sim$ 60 km wide during the developing and mature stages; therefore, the stratiform region was not as accurately represented by the objective analysis scheme as in the 10-11 June case. Because smaller-scale motions could not be resolved and the features in both the convective region and the stratiform region were smoothed into each other and into the environment, some diagnostic variables such as the vertical motion might suffer large underestimation. Ogura and Liou (1980) and Kuo and Anthes (1984) pointed out this common problem in mesoscale analysis. During the dissipating stage, the horizontal extent of the stratiform region increased to 100 km, so that its structural details could be better resolved during that stage.

3.5 Radar maps and surface data

Although the budget study emphasizes the upper air sounding data, radar maps and surface rainfall data were also used.

Radar reflectivity maps from the NWS WSR-57 radars located at Wichita, Kansas, and Oklahoma City, Oklahoma, provided a good time evolution of the reflectivity patterns of the 26-27 June squall line from the developing and mature to the dissipating stages. The convective and stratiform regions were separated according to radar reflectivity.

The surface rainfall rates and cumulative rainfall data were obtained from the NSSL SAM and NCAR PAM-II surface observational networks. Subjective analyses were performed to contour the precipitation rate at different times and to compare with the diagnosed rates from the vertically-integrated budgets.

Chapter 4

MESOSCALE STRUCTURE

The 26-27 June squall line was a slow moving, long-lived mesoscale convective system with a narrow stratiform region. It remained within the PRE-STORM network for most of its developing, mature and dissipating stages. A cold front was following the squall line and moving from northwest to southeast. The 0000 UTC 27 June 500 hPa analysis (Figure 4.1) shows that a strong upper-level trough was located west of the PRE-STORM region and would move slowly eastward. During the entire process, the pre-frontal squall line system swept slowly through the PRE-STORM network and left a large amount of precipitation. Since this squall line had many differences from the typical symmetric, fast-moving squall lines, which have often been studied, the aim of this chapter is to show the spatial and temporal evolution of the relative wind field, divergence and vertical velocity from the developing and mature to the dissipating stages and to compare them to typical symmetric cases.

4.1 Squall line history

Before 2100 UTC 26 June, the mesoscale convective system was somewhat disorganized. Figure 4.2a shows the composited low-level radar reflectivity at 1825 UTC. The system can be divided into three distinct components (Trier et al. 1991): A 50-70-km-wide prefrontal squall line, a narrow rainband coincident with the surface cold front and a series of deep convective rainbands and cells that formed in advance of the prefrontal squall line. The frontal rainband and the pre-squall deep convective rainbands and cells were nearly parallel to the prefrontal squall line. With the passage of time, the entire squall line

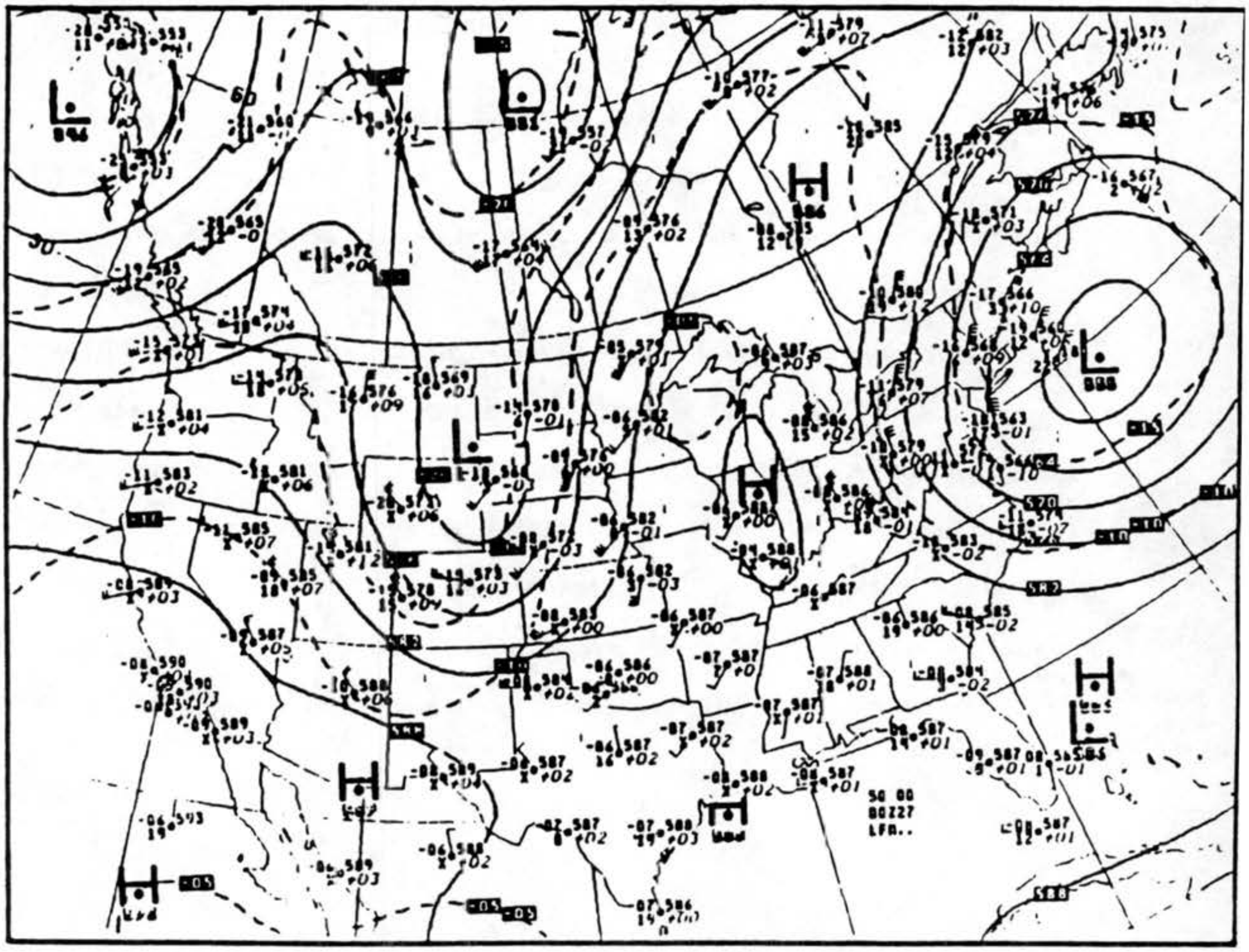

Figure 4.1: NMC 500 hPa analysis for 0000 UTC 27 June 1985. Isotherms (5 °C intervals) dashed, geopotential height contours (6 m intervals) solid. Conventional plotting model is used.

system gradually organized. The cold front and frontal rainband slowly caught up with the prefrontal squall line and in the meantime the reflectivity of the squall line increased during this time, especially over the Oklahoma region. The deep convective rainbands and cells ahead of the prefrontal squall line also slowly merged with the squall line and redefined the leading edge of the MCS. At 2131 UTC (Fig. 4.2b), the system became a nearly solid squall line, although some part of it still indicated organizing features.

During the intensive analysis from 2100 UTC 26 June to 0430 UTC 27 June (Figs. 4.2b-g), the portion of the 26-27 June squall line over Kansas had distinct differences from the part over the Oklahoma region. The radar echo over Kansas was dominated by low reflectivity, indicating stratiform precipitation from 2100 to 0400 UTC, except that during the early stage, there was a $10 - 20$ km wide convective region at the leading edge. After 0400 UTC, most of the radar echo over the Kansas region dissipated. The Kansas portion of the squall line showed systematic evolution from the mature to the dissipating stages.

The part of the squall line over Oklahoma exhibited intense developing features of the squall line during early times, as compared to the nearly late mature to the dissipating stages over Kansas. From 2100 to 0000 UTC (Figs. 4.2b, c and d), it had higher radar reflectivity and the convective region was equal to or larger than the area occupied by the stratiform region. During this time interval, this segment of the squall line can be defined as at its developing and early mature stages. Beginning from 0130 UTC (Fig. 4.2e), the width of the stratiform region gradually increased from about $30 - 40$ km to nearly 100 km at later times. The width of the convective region decreased to about $30 - 40$ km. At 0300 and 0430 UTC, the enhanced reflectivity pattern (not shown here) showed a clear separation of the convective region, the stratiform region and the transition region over Oklahoma, indicative of the late mature to the dissipating stages. After 0430 UTC 27 June, the movement of the squall line nearly ceased but its dissipation continued significantly longer.

Newton and Fankhauser (1964) first investigated the evolution of asymmetric squall line cases. They found that new convection usually develops on the south ends of squall lines and older thunderstorms dominate the northern ends of lines, which is similar to the

(a) 1825 UTC

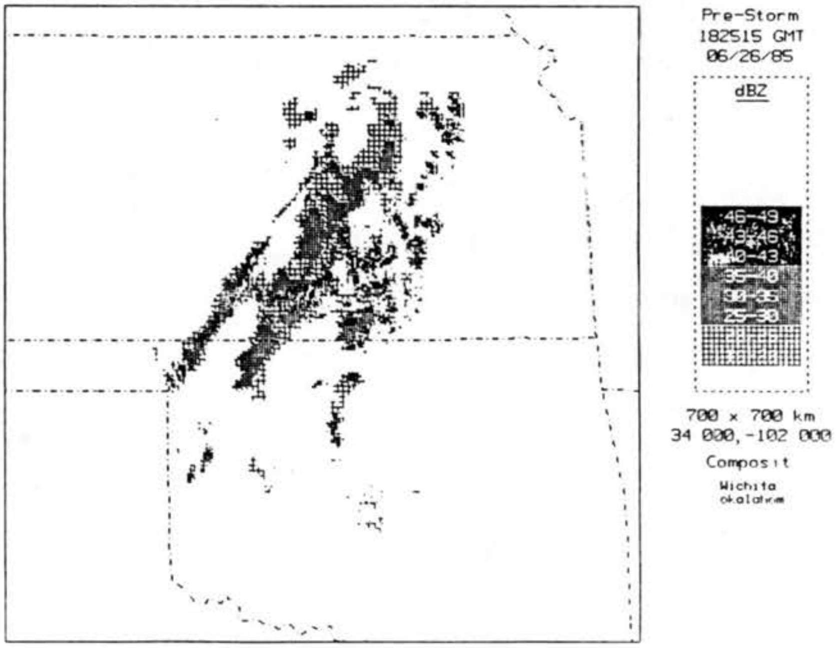

(b) 2131 UTC

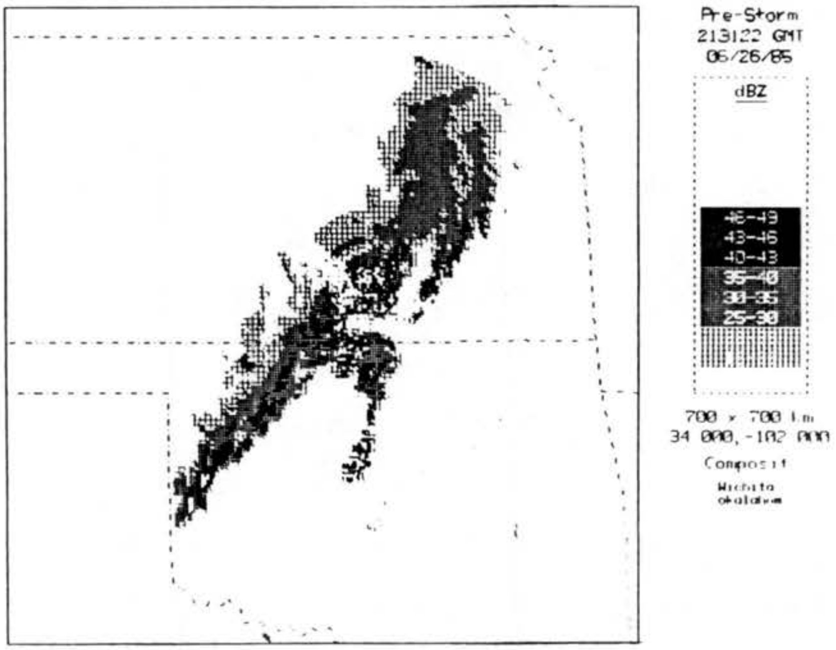

Figure 4.2: Composited low-level reflectivity patterns during the life time of the 26-27 June squall line. a) 1825 UTC, b) 2131 UTC, c) 2234 UTC, d) 0010 UTC, e) 0134 UTC, f) 0306 UTC, g) 0430 UTC, h) 0600 UTC.

(c) 2234 UTC

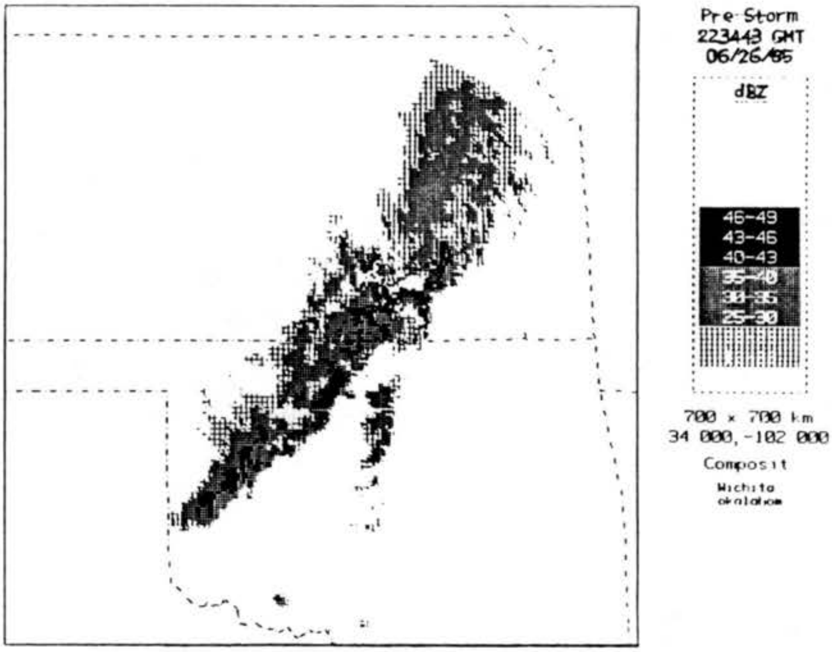

(d) 0010 UTC

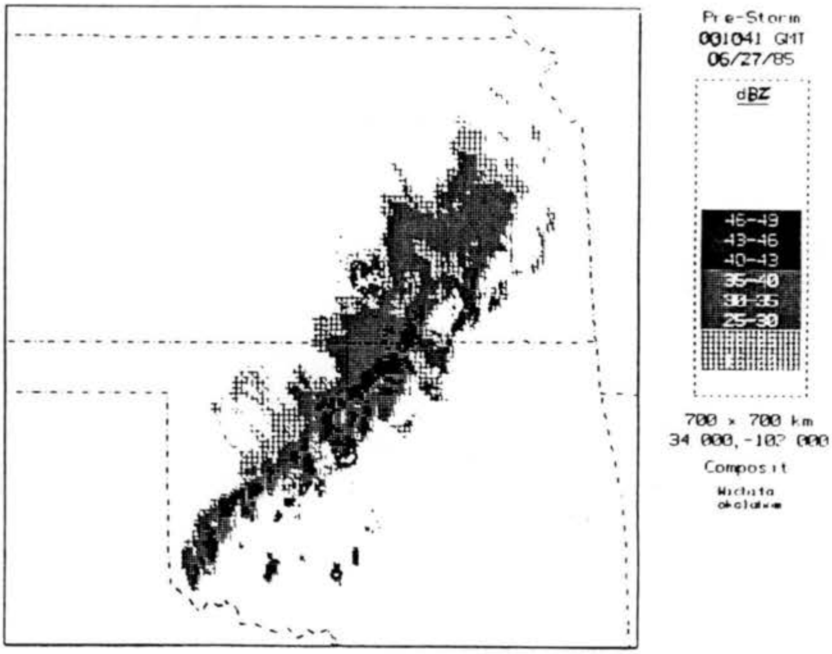

Figure 4.2: Continued.

(e) **0134 UTC**

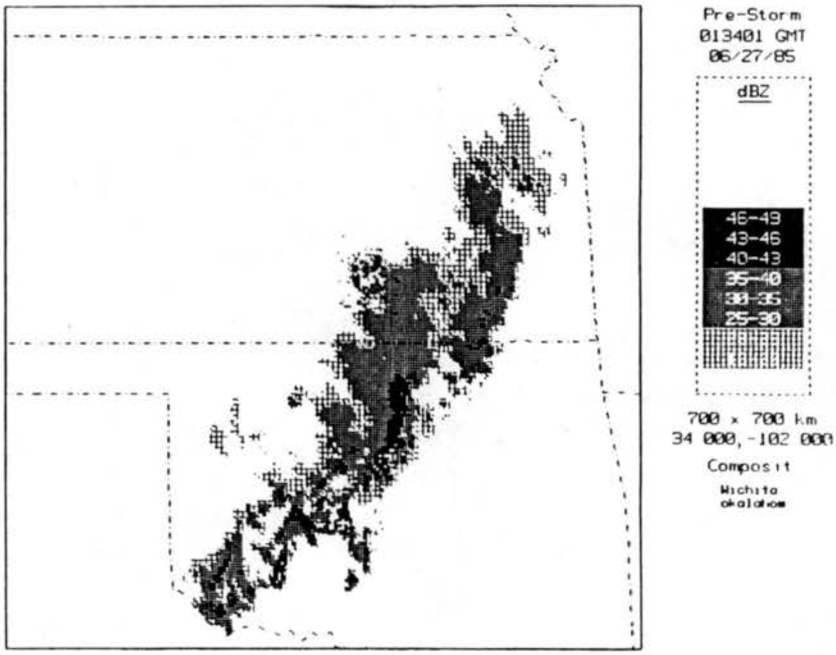

(f) **0306 UTC**

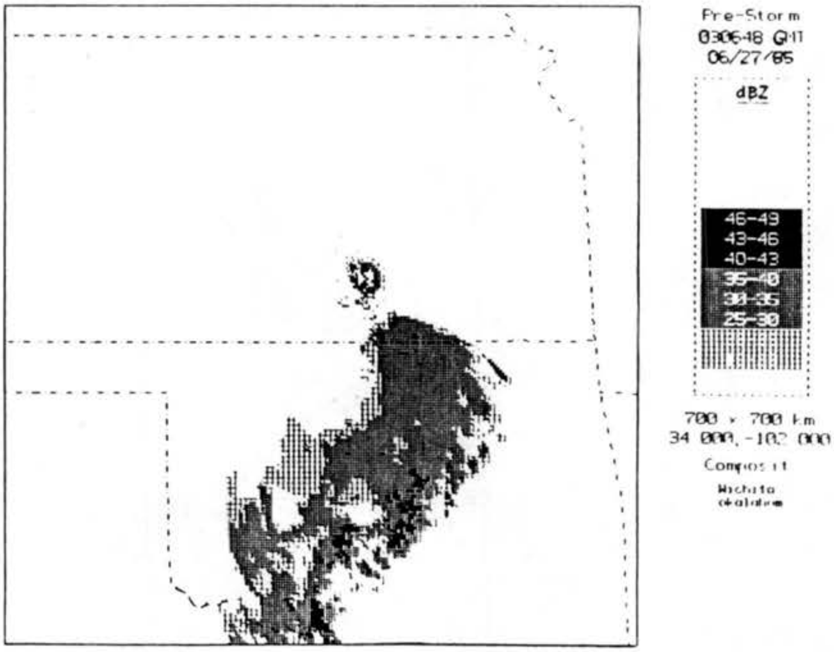

Figure 4.2: Continued.

(g) 0430 UTC

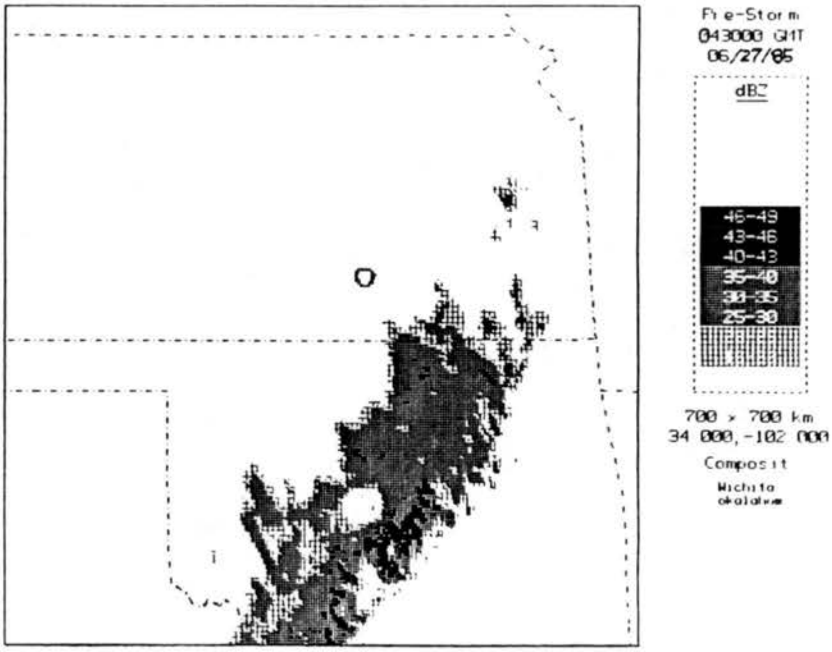

(h) 0600 UTC

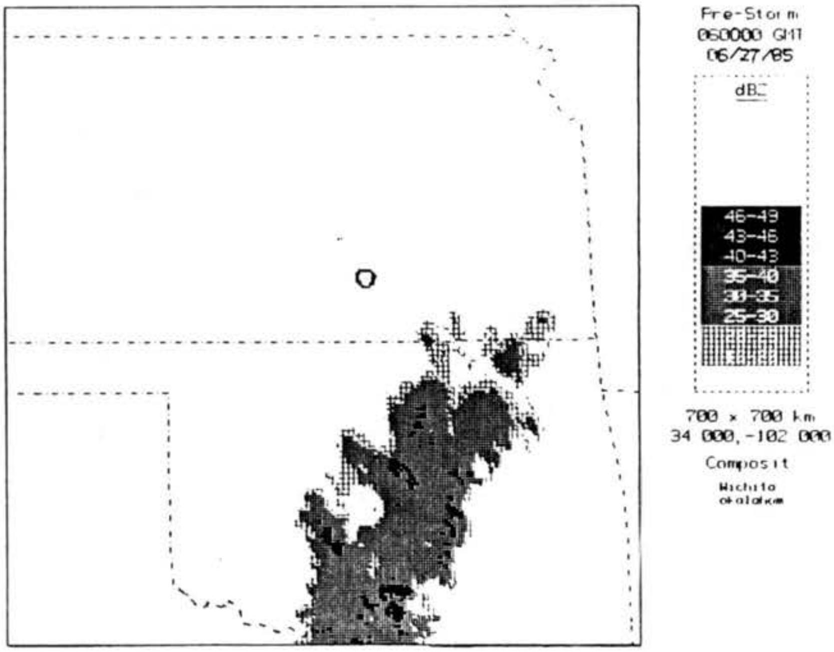

Figure 4.2: Continued.

26-27 June squall line during its early stages. They also noticed that an extensive stratiform precipitation area is not typically found in this type of squall line, except possibly on the north end. Houze et al. (1990) further defined the symmetric and asymmetric cases according to a climatological study of mesoscale organization of springtime rainstorms in Oklahoma. In the symmetric case, the convective line shows no preference for the most intense cells to be found at any particular location along the line while the stratiform region has its centroid located directly behind the center of the convective line. In the asymmetric case, the convective line is stronger on its southern, southwestern, or western end, while the centroid of the stratiform region is biased toward the north, northeast, or east end of the line. Their results indicated that the asymmetric cases are almost as common as symmetric cases over the Great Plain region. The 26-27 June PRE-STORM squall line, according to their definition, can be attributed to an intermediate asymmetric pattern during the developing and mature stages and a more symmetric pattern during the decaying stage.

In this study, radar reflectivity is used to divide the entire system into the convective region and the stratiform region, although sometimes the two are quite difficult to distinguish. The convective region is defined as the region with reflectivities exceeding 35 dBZ and the stratiform region with lesser values. The transition region only appeared at 0300 and 0430 UTC on enhanced radar reflectivity maps. It was very narrow and can not be resolved by PRE-STORM network, so it is not studied in this case.

Since the squall line exhibited asymmetric features in this case and the widths of the stratiform and convective regions varied at different times and in different regions, the vertical cross sections were constructed using a method somewhat different from that used by Ogura and Liou (1980) and Gallus and Johnson (1991). In this study, slabs ($\sim$ 50 km wide) were selected to be normal to the squall line instead of along the squall line. Therefore, one slab will represent a single cross section normal to the squall line. This method makes it easy to study the three dimensional features of a MCS. The system-averaged or region-averaged vertical cross sections can be easily determined by averaging these slabs normal to the squall line. Careful consideration was taken in order not to average values at single grid points twice.

4.2 Relative wind

The system-averaged vertical cross sections of relative wind normal to the squall line from 2100 UTC 26 June to 0430 UTC 27 June are shown in Figure 4.3 at 90-minute intervals. The relative velocity is obtained by subtracting the average movement of the system from grided wind data normal to the line.

At 2100 UTC (Fig. 4.3a), front-to-rear flow is quite evident ahead of the system. The peak value (about 12.0 m s^{-1}) was slightly above 900 hPa and was much weaker than that found in the 10-11 June case (nearly 24.0 m s^{-1} at 900 hPa) (Gallus and Johnson 1991). The front-to-rear flow sloped upward toward the rear of the system with speeds exceeding 24.0 m s^{-1} over 200 km behind the leading edge between 250 and 300 hPa, similar to that of the 10-11 June case (about 28.0 m s^{-1} at 250 hPa).

The front-to-rear jet decreased rapidly at upper levels from 200 km behind the system toward the leading edge and reached its minimum (nearly 4.0 m s^{-1}) at 200 hPa just ahead of the leading edge. Rutledge et al. (1988), using radar data, found in the 10-11 June case that there was a rear-to-front flow which resulted from cloud top divergent outflow at upper levels ahead of the leading edge. Although almost no rear-to-front flow was found at this position in this case, there was a minimum of front-to-rear flow and that can be attributed to the divergent outflow aloft.

The most pronounced difference from the 10-11 June squall line is at low levels between 950 and 800 hPa behind the leading edge: There was a strong rear-to-front flow (maximum was 7.2 m s^{-1}) induced by the cold front. There was also a middle level environmental rear-to-front flow that can be observed near 600 hPa. At this time, it was similar to the 10-11 June case, but was with rather weak values (less than 4.0 m s^{-1}), and did not extend downward into the system.

Relative wind at 2230 and 0000 UTC (Figs. 4.3b and c) showed similar patterns to that of 2100 UTC, except that the lower branch of the rear-to-front flow gradually extended forward to within 50 km of the leading edge. This behavior is likely a reflection of the fact that the cold front moved a little faster than the squall line. However, the

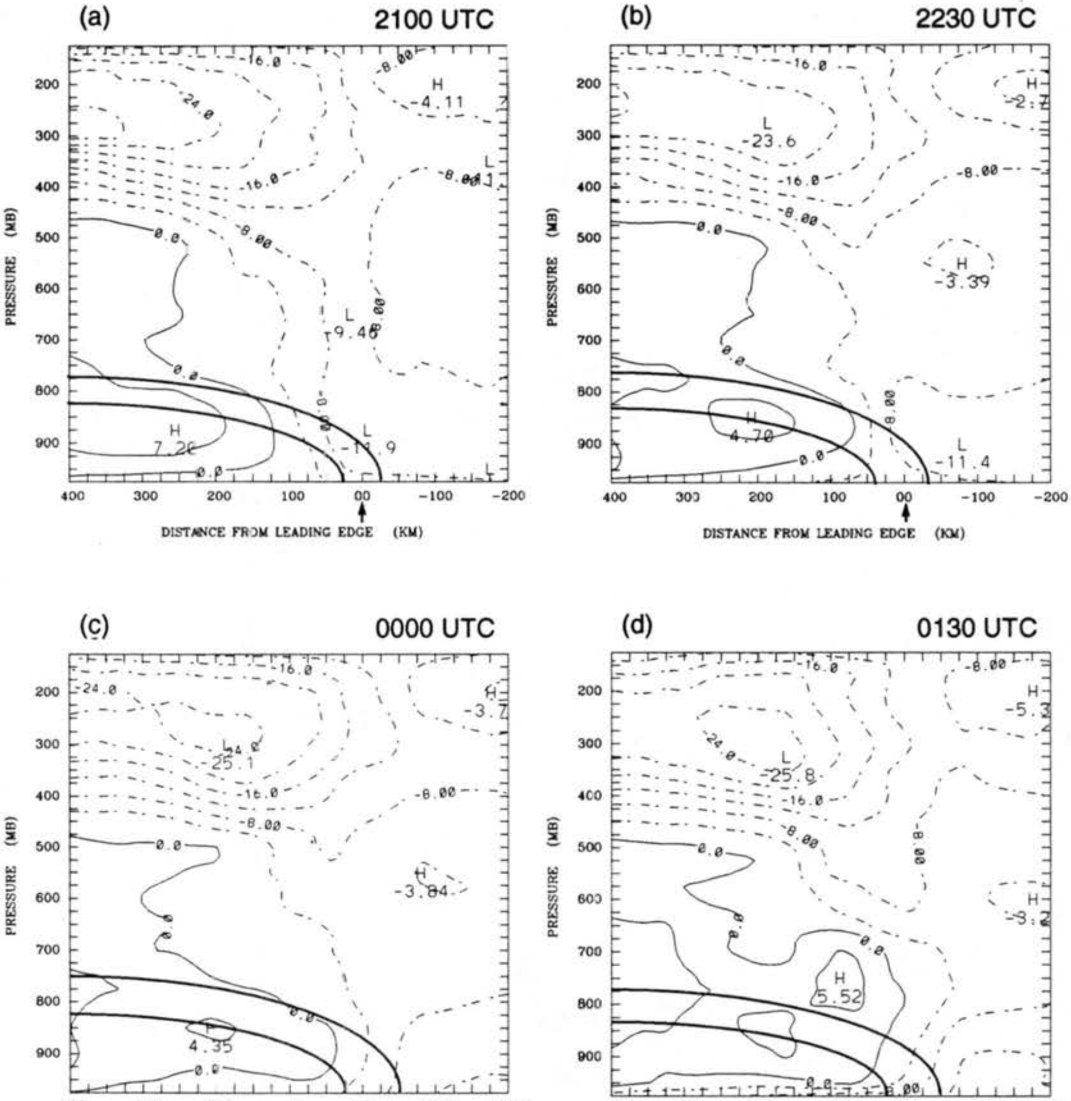

Figure 4.3: Relative wind (in m s^{-1}) normal to the squall line. a) 2100 UTC, b) 2230 UTC, c) 0000 UTC, d) 0130 UTC, e) 0300 UTC, f) 0430 UTC. Positive values indicate flow from rear to front (left to right). Heavy solid lines approximately delineate the low-level frontal zone. Arrow denotes the leading edge.

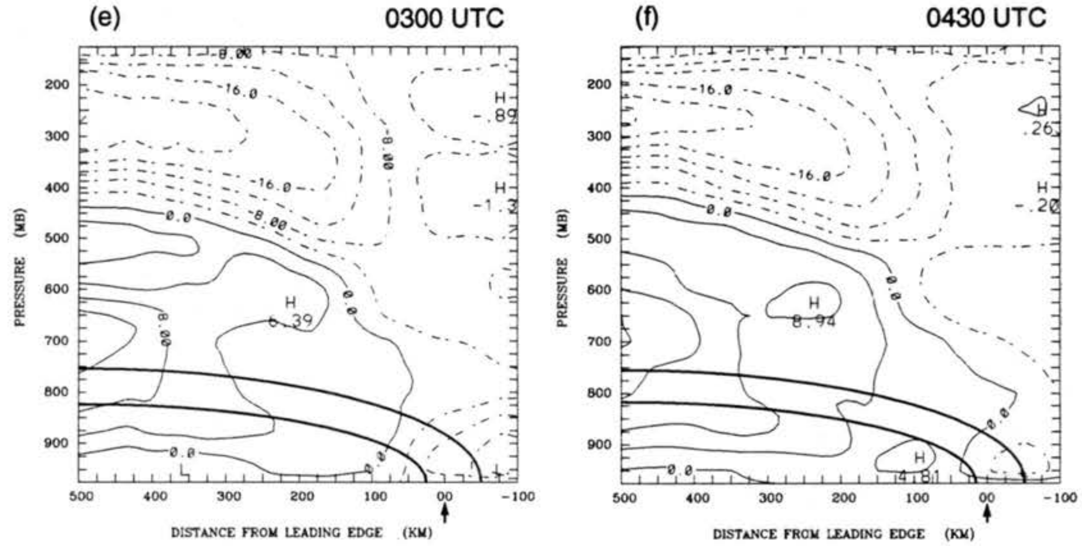

Figure 4.3: Continued.

intensity of the lower branch of the rear-to-front flow gradually decreased. During this time interval, it appeared that there was still no tendency for the middle level rear-to-front inflow to extend downward in a pronounced way into the system.

By 0130 UTC (Fig. 4.3d), the depth of the rear-to-front flow within 200 km behind the leading edge began to increase. Not only was there a peak (more than 4.0 m s^{-1}) associated with the cold front between 900 and 850 hPa 175 km behind the system, but also there was another peak (nearly 5.5 m s^{-1}) located at 750 hPa 75 km behind the leading edge. Since the cold front did not extend as high at this position, this maximum is probably an indication that the mid-level rear-to-front flow finally began to descend into and/or develop behind the system.

From 0300 to 0430 UTC (Figs. 4.3e and f), when the squall line was in its dissipating stage, the rear-to-front flow shows different patterns from those of the early stages. At a distance of over 400 km behind the leading edge, the two rear-to-front inflow maxima gradually merged and the peak intensity increased to 12.0 m s^{-1} between 600 and 800 hPa 500 km behind the leading edge. Within 300 km of the convective line, there were two clearly separated branches of rear-to-front flow at 0300 UTC. The upper branch showed a clear pattern of the strengthening mid-level rear-to-front flow extending from well behind the leading edge down to 750 hPa within the system. This strengthening also corresponded to the period when the trailing stratiform region expanded significantly (Fig. 4.2).

From the above analyses, there are some similarities and some differences between the 26-27 June squall line and the 10-11 June case. A basic difference was that in the 26-27 June case the squall line was followed by a low-level cold front and its associated rear-to-front flow having a peak of $5 \sim 8$ m s^{-1} near 800-950 hPa. However, the flow near the surface and at upper levels in the two cases was very similar. The front-to-rear flow, similar to typical symmetric squall lines, transported heat and moisture from the convective region up to the middle and upper levels of the rear of the system. Although at low levels behind the leading convective line, it was dominated by the rear-to-front flow associated with the cold front, there were also indications of a weak front-to-rear flow near the surface behind the leading edge, which was usually found as a result of an overturning downdraft fed by divergence underneath the stratiform region (Srivastava et al. 1986, in Fig. 15; Augustine and Zipser 1987; Smull and Houze 1987, in Figs. 4b and 5b; Johnson and Hamilton 1988, in Fig. 16; Rutledge et al. 1988, in Figs. 4b, 5b and 6b; Gallus and Johnson 1991, in Fig. 3). But it occupied only a very shallow layer above the surface. The front-to-rear flow at low levels ahead of the leading edge was much weaker throughout the whole analysis compared to the 10-11 June case. However, the horizontal wind shear across the squall line remained relatively strong. Another feature is that the upper level front-to-rear flow had a similar magnitude to the 10-11 June case and increased slowly from the developing to mature stages, and then decreased at the dissipating stages. The mid-level rear-to-front flow, which was associated with the squall line system, was not apparent during the early stages compared to the large magnitudes of the rear-to-front flow at low levels. It gradually increased its strength from the developing and mature to the dissipating stages. At later times, the two rear-to-front inflows, resulting from different mechanisms, formed a deep layer of rear-to-front inflow behind the leading edge.

Figure 4.4 shows the along-line component of the relative wind. Consistent with the existence of a low-level cold front, there was a relatively strong vertical shear around the front. Strong horizontal shear of positive relative vorticity also existed at low-levels along the front. At 650 hPa just above the leading edge, a low-level southwesterly jet can be noticed at 2100 UTC, which was associated with the cold front. Its magnitude gradually decreased with the passage of time. Southwesterly flow was dominant aloft within the system and increased toward the rear, with speeds exceeding 36.0 m s^{-1} at 0430 UTC. It may be related to an upper level synoptic jet. At low levels behind the front was northeastly flow dominated. Its magnitude varied little throughout the evolution of the system.

4.3 Divergence

The vertical cross sections of divergence normal to the 26-27 June squall line are illustrated in Figure 4.5. During the entire evolution process, the strongest convergence

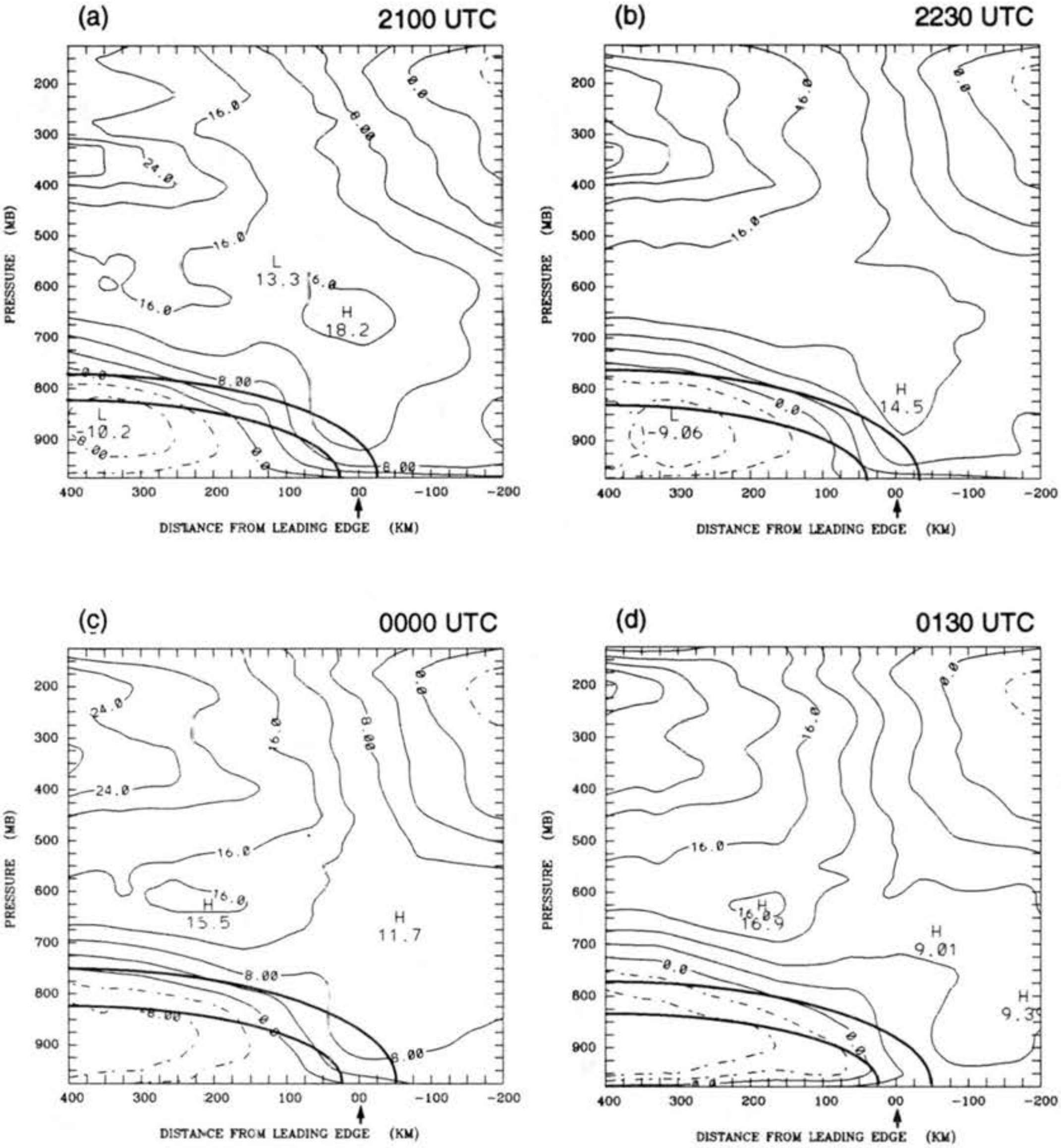

Figure 4.4: Relative wind (in m s^{-1}) along the squall line. a) 2100 UTC, b) 2230 UTC, c) 0000 UTC, d) 0130 UTC, e) 0300 UTC, f) 0430 UTC. Positive values indicate southwest flow. Heavy solid lines approximately delineate the position of the low-level frontal zone. Arrow denotes the leading edge.

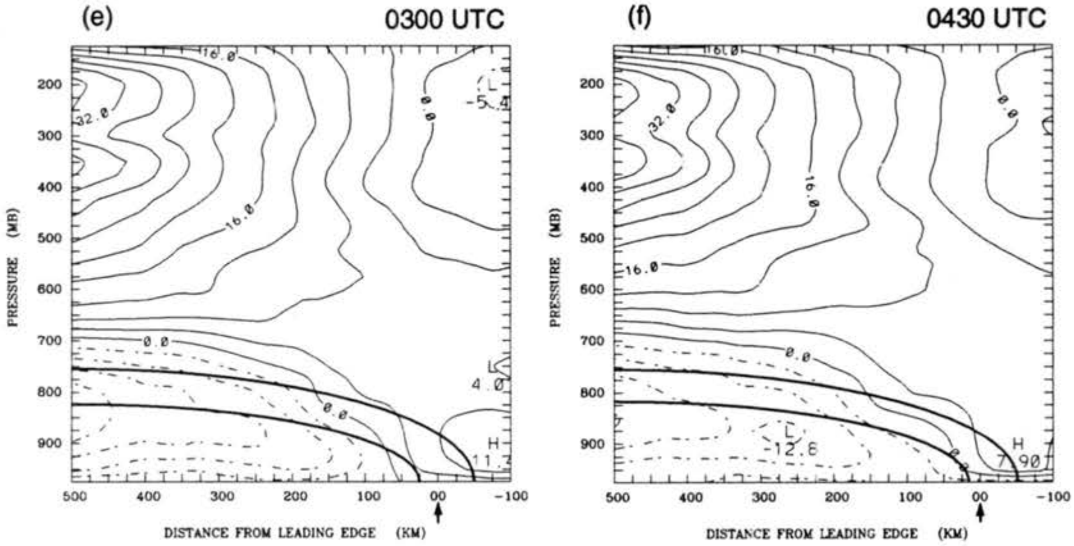

Figure 4.4: Continued.

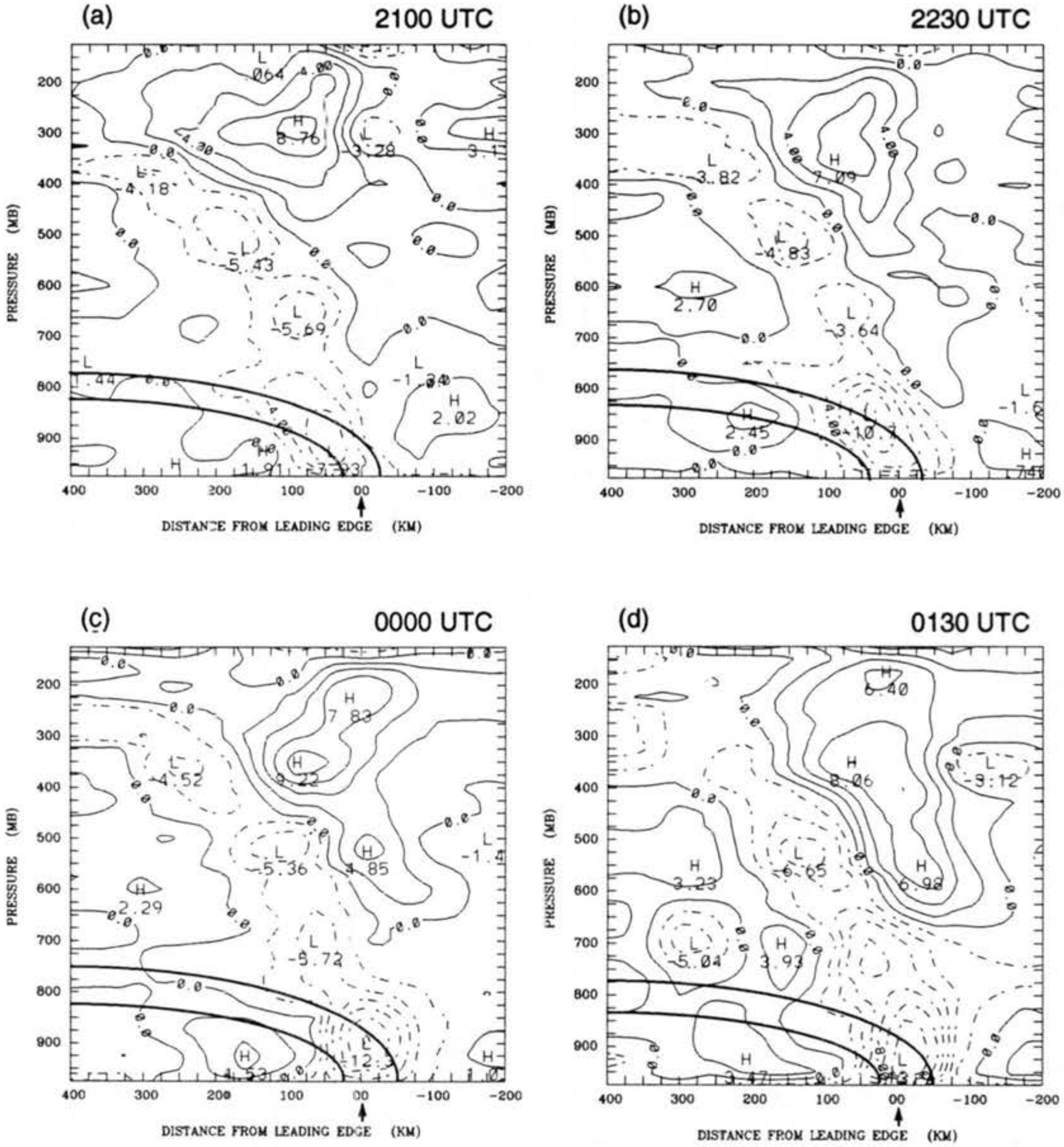

Figure 4.5: As in Fig. 4.3 except for divergence, in unit of 10^{-5} s^{-1}.

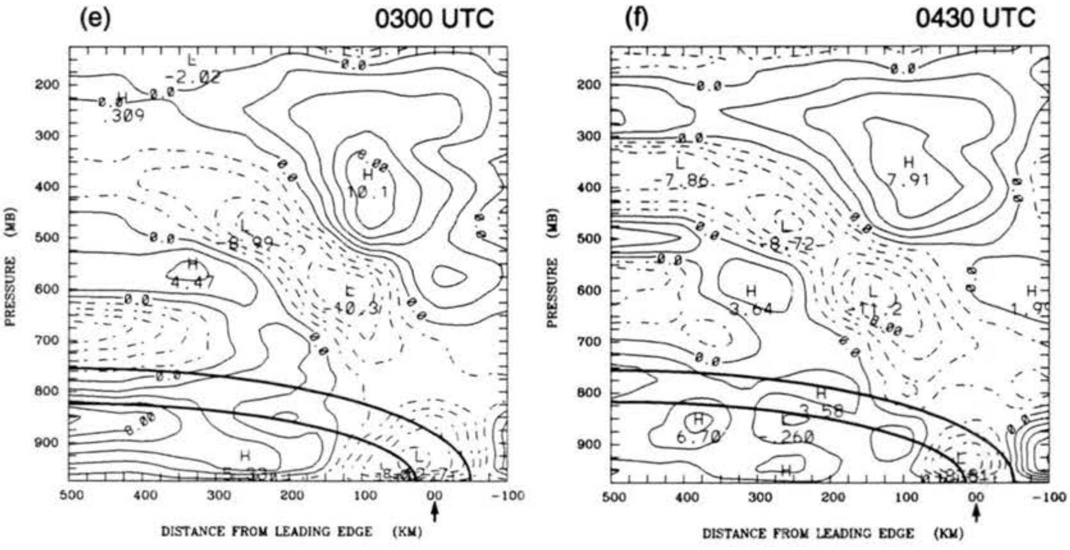

Figure 4.5: Continued.

was generally located at about 900 hPa near the leading edge except at 0430 UTC. Similar to previous diagnostic studies of middle latitude squall lines (Ogura and Liou 1980; Gallus and Johnson 1991), the axis of the convergence within the system tilted from low levels near the leading edge up to high levels in the rear of the system due to the strong convergence of the rear-to-front flow and the front-to-rear flow. There were several convergence peaks with similar magnitudes located at middle and upper levels within the convergence zone. The average magnitude in the mid-troposphere was 5.0×10^{-5} s^{-1} from 2100 to 0130 UTC and increased to about 1.0×10^{-4} s^{-1} at 0300 and 0430 UTC. This increase might be an indication that at later times the middle level rear-to-front inflow associated with the squall line strengthened and converged more intensively with the front-to-rear flow.

In the convective region and ahead of the leading edge, there was strong convergence at low levels and divergence from middle to high levels. From the developing and mature to the dissipating stages (2100 – 0430 UTC), the basic structure of the divergence pattern remained almost the same. Convergence near the surface gradually increased from 7.9×10^{-5} s^{-1} at 2100 UTC, and reached the maximum (13.9×10^{-5} s^{-1}) at 0130 UTC, then slowly decreased during the dissipating stage (12.7×10^{-5} s^{-1} at 0300 UTC and 8.8×10^{-5} s^{-1} at 0430 UTC). The magnitudes of divergence and convergence were generally smaller than those of the 10-11 June case (Gallus and Johnson 1991), suggesting that the intensity of the 26-27 June case might be weaker than that of the 10-11 June squall line.

Figure 4.6 shows the vertical profiles of divergence averaged over the convective region and the stratiform region. In the convective region (Fig. 4.6a), the vertical profiles at different times (from 2100 to 0300 UTC) were quite similar. Convergence was present below 575 hPa. The average peak value (about 1.0×10^{-4} s^{-1}) was generally located at $\sim 850 - 950$ hPa, indicating the interrelationship between the upward transport of mass and moisture and the large convergence at low levels. Above 575 hPa, divergence dominated. Peak values were generally around 7.0×10^{-5} s^{-1}.

Compared with the convective region, the vertical profiles of divergence in the stratiform region (from 2230 to 0430 UTC) showed a different pattern (Fig. 4.6b). Below 700 hPa, very weak convergence existed uniformly at most of times. It was partly due to

(a) Convective region

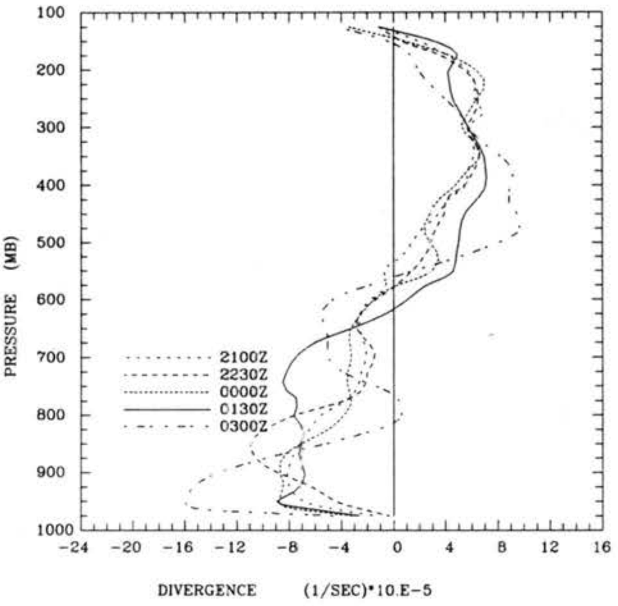

(b) Stratiform region

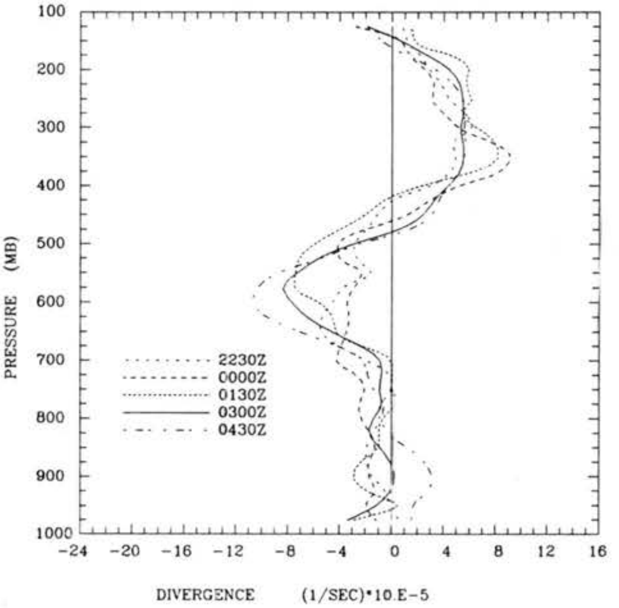

Figure 4.6: Vertical profiles of divergence (in 10^{-5} s^{-1}) averaged over a) the convective region from 2100 to 0300 UTC, b) the stratiform region from 2230 to 0430 UTC.

the aliasing from the convective region. At 0430 UTC, divergence was occurring below 800 hPa. This feature may have resulted from the rear-to-front inflow and the system's mesoscale downdrafts. Convergence peaks were generally located between 500 and 600 hPa and the magnitudes increased with time. The presence of mesoscale updrafts above and mesoscale downdrafts below in the stratiform region was the main contribution from the midlevel convergence. Between 175 and 400 hPa divergence occurred due to outflow at the top of the system.

Divergence profiles for the entire system are considered in Figure 4.7. Two peaks of convergence resulting from the convective and stratiform regions can be clearly noticed below 500 hPa prior to 0300 UTC. One occurred at low levels ($\sim$ 900 hPa) and the other at middle levels ($\sim$ 600 hPa). As the system evolved from the developing and mature to the dissipating stages, the low-level convergence gradually decreased, which indicates that the low level mass and moisture supply to the whole system decreased. On the other hand, the midlevel convergence gradually increased, implying a growing influence of the stratiform region. More mass and moisture converged at middle levels by the rear inflow and the front-to-rear flow and went to feed mesoscale updrafts and downdrafts within the stratiform region. The non-divergence level was around 500 hPa, a level higher than the melting level (600 hPa). From 500 to 150 hPa a deep layer of uniform divergence existed similar to that in the convective region. Further above, weak convergence can be noticed near tropospause and this feature has also been found in several other studies (e.g., Johnson et al. 1990).

4.4 Vertical motion

Figure 4.8 shows the vertical motion in the squall line from the developing and mature through the dissipating stages. At 2100 and 2230 UTC, the 26-27 June squall line demonstrated the most pronounced asymmetry over the Oklahoma and Kansas regions. Since the vertical motion field is sensitive to the asymmetry, averaged cross sections for Kansas and Oklahoma regions are portrayed respectively. During these times, the part of

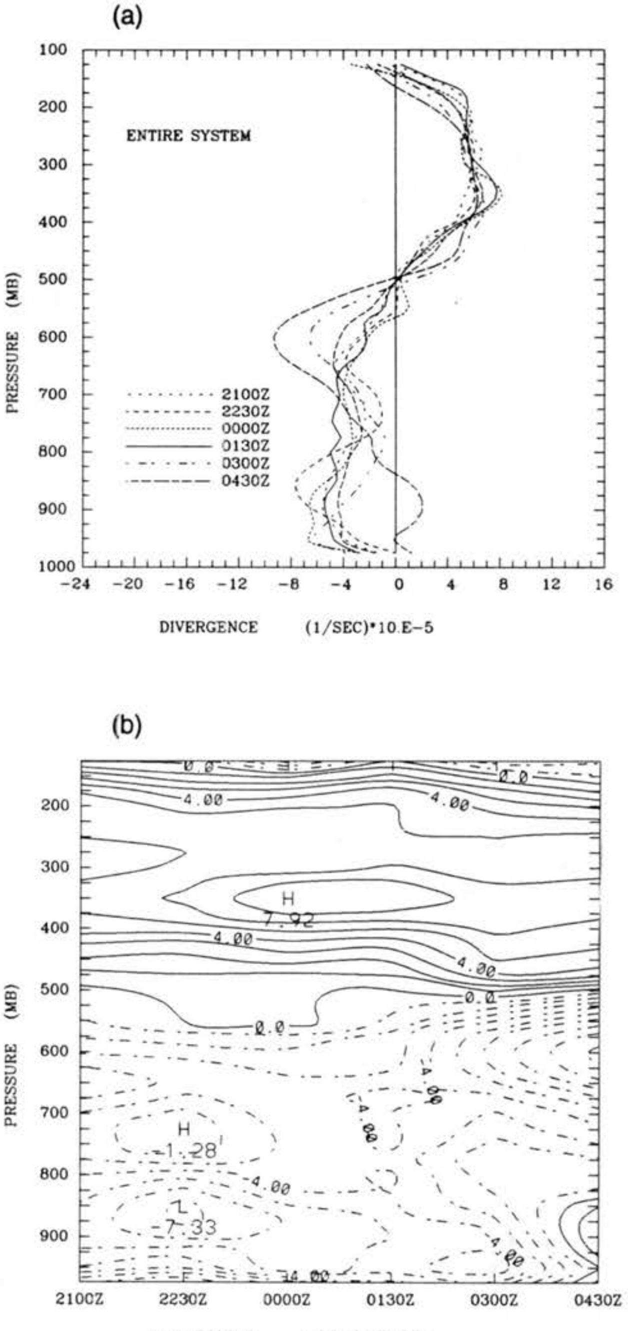

Figure 4.7: Vertical profiles (a) and time evolution (b) of divergence (in $10^{-5}\ \mathrm{s}^{-1}$) averaged over the entire region from 2100 to 0430 UTC.

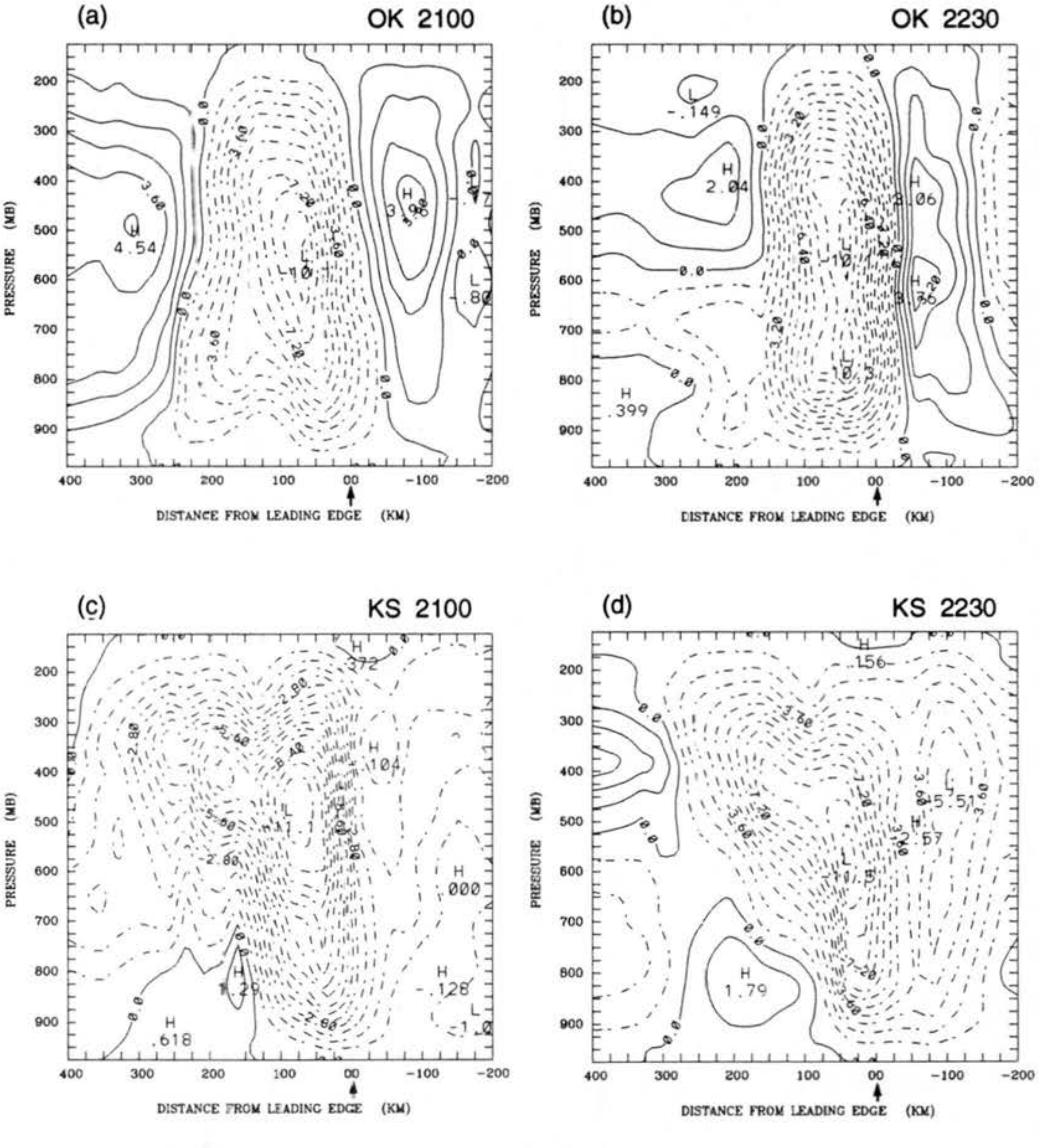

Figure 4.8: Vertical velocity (ω) (in unit of μb s^{-1}) normal to the squall line. a) the OK region at 2100 UTC, b) the OK region at 2230 UTC, c) the KS region at 2100 UTC, d) the KS region at 2230 UTC, e) 0000 UTC, f) 0130 UTC, g) 0300 UTC, h) 0430 UTC.

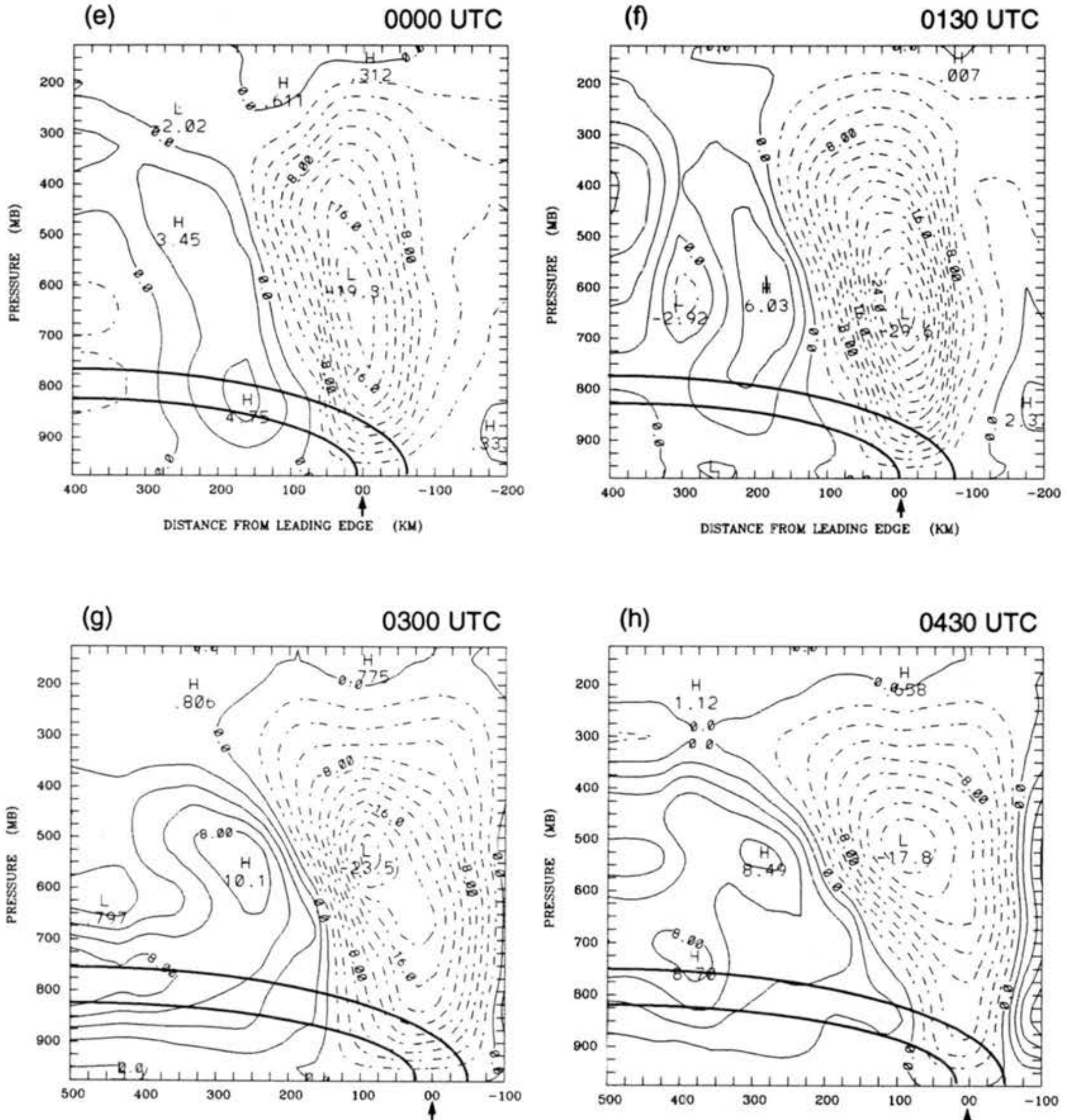

Figure 4.8: Continued.

the squall line over Oklahoma was basically a convective line (about 30 to 50 km wide). The vertical velocity within this part of the squall line was dominated by upward motion throughout the whole troposphere with a peak of 10.1 μb s^{-1} at 550 hPa at 2100 UTC (Fig. 4.8a) and 2230 UTC (Fig. 4.8b). Because of the narrowness of the squall line, aliasing due to poor resolution and weaker intensity of the squall line, the magnitude of upward motion was much smaller than that found by Gallus and Johnson (1991) for the 10-11 June case.

Regions of compensating descent in front of the leading edge have been shown in many squall line studies (Fankhauser 1974; Fritsch 1975; Sanders and Paine 1975; Gamache and Houze 1982; Gallus and Johnson 1991). Ahead of the leading edge of the 26-27 June squall line at 2100 and 2230 UTC, there was a 120 km wide region of downward motion throughout the depth of the troposphere over Oklahoma. The average peak value was around 3.8 μb s^{-1} at 425 hPa. To the rear of the system was another extensive region of compensating downward motion with a peak centered between 400 and 500 hPa.

Based on radar reflectivity maps, the part of the squall line over Kansas was in its mature to dissipating stages at 2100 and 2230 UTC. The pattern of the vertical motion (Figs. 4.8c and d) was distinctly different from that over Oklahoma. The most prominent difference was the larger horizontal extent of upward motion over Kansas. Near the leading edge, features of the convective region can be noticed. There was upward motion throughout most of the troposphere with an average peak of 11.3 μb s^{-1} at 550 hPa. In the stratiform region, from middle to upper levels there was upward motion with an average peak 9.6 μb s^{-1} at 400 hPa. At low levels from 800 hPa to the surface there was weak downward motion at 100 to 300 km behind the leading edge. Because the rear of the system was near the northwest edge of the grid, where it was almost outside the sounding network, the features within the stratiform region were smoothed to the rear of the system. Also the weak upward motion ahead of the leading edge might be the result of aliasing of the features in the convective region during objective analysis.

Beginning at 0000 UTC, the part of the squall line over the Oklahoma region also evolved into the mature and the dissipating stages. The asymmetry was not as pronounced as that at earlier times, so only the average of the entire system is considered.

From 0000 to 0130 UTC, the movement of the squall line was the fastest during the entire system evolution. Therefore, the features within the system should be better represented by the composite analysis. Vertical motion at these two times is shown in Figs. 4.8e and f. The peaks of upward motion at these two times were located at about 600 to 650 hPa with magnitudes of 19.3 μb s^{-1} at 0000 UTC and 29.6 μb s^{-1} at 0130 UTC. The increase in magnitude of upward motion peak from 0000 to 0130 UTC was quite dramatic. It was probably influenced in part by a sounding station near the leading edge that was located in a very strong convective core at 0130 UTC. To the rear of the system was a deep layer of downward motion. The maximum downward motion increased from 0000 UTC (4.8 μb s^{-1}) to 0130 UTC (6.0 μb s^{-1}) and the peak shifted upward from 800 to 600 hPa.

At 0000 and 0130 UTC, the slopes of the axes of maximum downward motion and upward motion for the entire system were nearly vertical. This structure is in agreement with radar observations showing that the stratiform region was still quite narrow and the system was not expanding rapidly.

From 0300 to 0430 UTC, the squall line was in its dissipating stage. The upward motion within the convective region decreased from about 29.6 μb s^{-1} at 0130 UTC to 23.5 μb s^{-1} at 0300 UTC, and to 17.8 μb s^{-1} at 0430 UTC. Strong downward motion can be clearly noticed to the rear of the system with peak values of 10.1 μb s^{-1} at 0300 UTC and 8.5 μb s^{-1} at 0430 UTC. The slope of the axes of maximum downward motion increased at the back edge of the squall line. Between 750 and 800 hPa about 300 km to the rear of the system, there was a second peak of downward motion, which might be associated with the cold front although it did not appear at earlier times. Downward motion also occurred ahead of the system, which may have resulted from the compensating flow associated with the MCS.

Figure 4.9 shows the vertical profiles and time evolution of vertical motion in the convective region averaged over both Kansas and Oklahoma. Similar to other studies of tropical and mid-latitude squall lines (Gamache and Houze 1982; Johnson 1984; Frank and McBride 1989; Gallus and Johnson 1991), strong upward motion dominated throughout

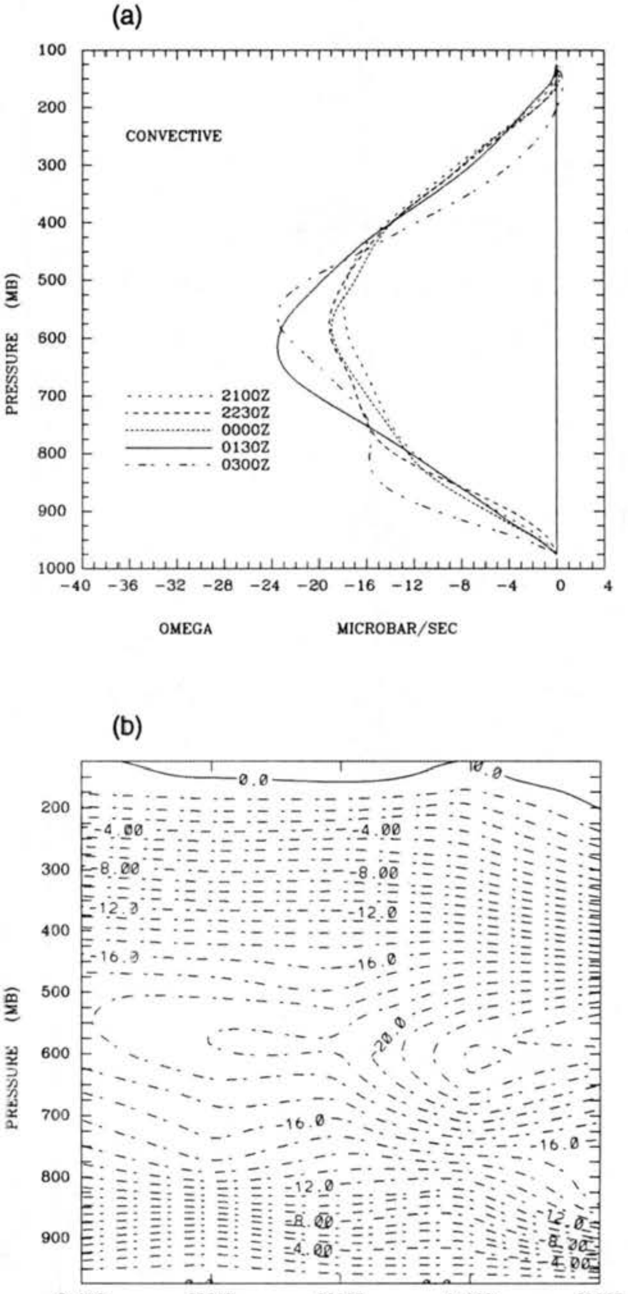

Figure 4.9: Vertical profiles (a) and time evolution (b) of vertical motion (in μb s^{-1}) averaged over the convective region of the squall line at different budget times from 2100 to 0300 UTC.

most of the troposphere in the convective region. The peaks of upward motion for different budget times were generally located between 550 to 600 hPa, a result similar to the 10-11 June case (Gallus and Johnson 1991). However, the magnitudes were much smaller than those in Ogura and Liou (1980) and Gallus and Johnson (1991) due to the narrowness and weakness of the squall line. The magnitudes of cumulus updrafts in the convective region gradually increased and reached 26.0 μb s^{-1} at 0130 UTC, and then slowly decreased. There was almost no indication of the effect of the low-level cold front on the vertical velocity evolution in the convective region.

In the stratiform region (Figs. 4.10a and b), vertical motion above the melting level between 600 and 250 hPa was dominated by mesoscale ascent in the anvil cloud. The level of maximum ascent was located at about 450 hPa, which was much lower than that determined in the 10-11 June case (350 hPa) (Gallus and Johnson 1991). This is probably due to weaker stratiform region in this case and the features in the convective region being smoothed into the stratiform region so that the level of maximum rising in the stratiform region shifted a little downward. The peak upward motion increased from the developing stage and reached the maximum intensity (15.0 μb s^{-1}) at 0130 UTC, and then gradually decreased during the decaying stage. At low levels, due to the influence of rear-to-front inflow and mesoscale downdrafts, the magnitudes of weak upward motion slowly decreased and turned into downward motion at 0430 UTC below 650 hPa.

Figure 4.11 shows the vertical profiles and time evolution of vertical velocity averaged over the entire system. From 2100 to 0300 UTC, the vertical profiles were quite similar to each other with peak upward motion over 15.0 μb s^{-1} centered between 500 and 550 hPa. Prominent changes took place during the dissipating stage when the developing stratiform region imposed more influence on the squall line. As illustrated in Fig. 4.3f, the rear-to-front flow descended from 200 km behind the leading edge into the system, and the mesoscale downdrafts gradually strengthened as the stratiform region developed. The upward motion at low levels during the dissipating stage rapidly decreased. At 0430 UTC, the system-averaged vertical motion was generally downward below 700 hPa. Above 700 hPa, the vertical motion during the dissipating stage was generally dominated by upward

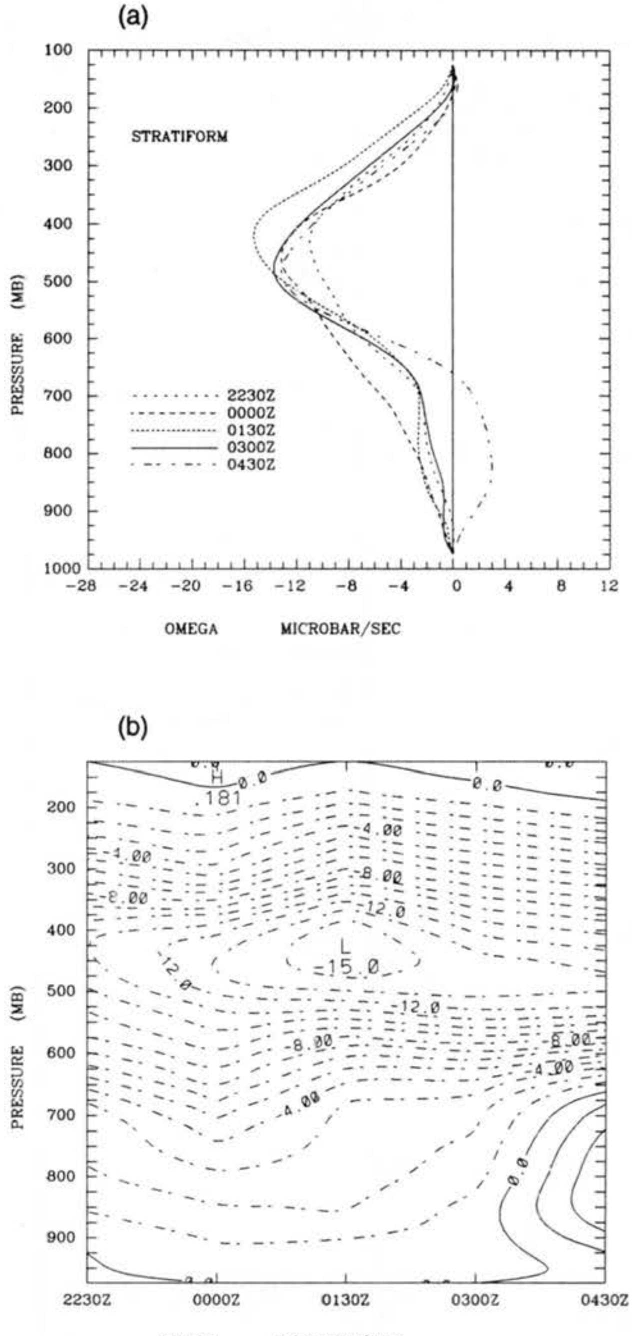

Figure 4.10: Vertical profiles (a) and time evolution (b) of vertical motion (in μb s^{-1}) averaged over the stratiform region of the squall line at different budget times from 2230 to 0430 UTC.

motion. The peak magnitude only weakened a little (14.0 μb s^{-1} at 0430 UTC) and was still located at middle levels around 500 hPa. Weak downward motion was present at the top at some times, similar to the results found by Balsley et al. (1988) and Johnson et al. (1990).

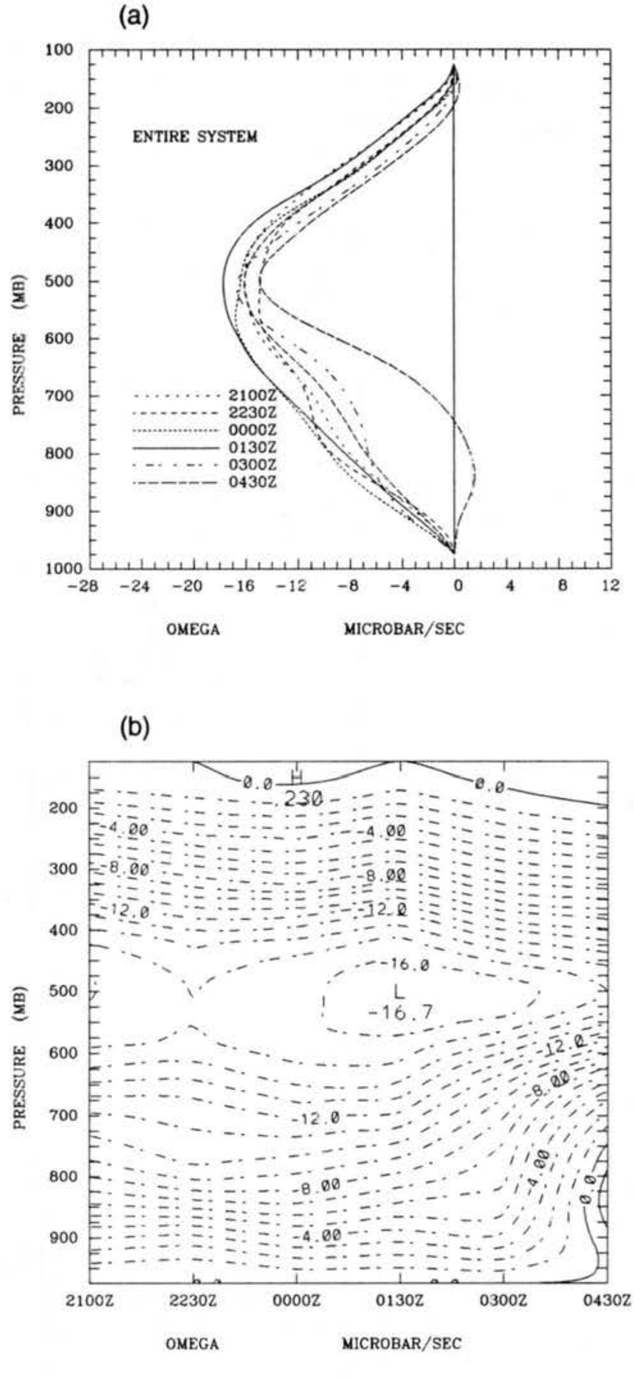

Figure 4.11: Vertical profiles (a) and time evolution (b) of vertical motion (in μb s^{-1}) averaged over the entire squall line system at different budget times from 2100 to 0430 UTC.

Chapter 5

THE HEAT AND MOISTURE BUDGETS

The kinematics and structure of the 26-27 June squall line differed from typical symmetric, fast-moving squall lines with extensive trailing stratiform regions, such as the 10-11 June PRE-STORM case. These differences, as discussed earlier, can lead to differences in the heating and drying patterns from other cases, and in turn, may also modify the large-scale environment in a different way.

Hertenstein and Schubert (1991) compared the potential vorticity patterns within the 10-11 June case (at 0600 UTC when the squall line was in its late mature and decaying stages and was characterized by an extensive trailing stratiform region) and the 26-27 June case (at 0000 UTC, when the squall line was at its developing and early mature stages and was generally dominated by the convective region). They found that there was a large, positive PV anomaly located at midlevels with negative anomalies in the upper and low levels in the 10-11 June case. In contrast, the 26-27 June squall line left the positive PV anomaly at low levels and a negative anomaly in the upper troposphere. Their model results suggest that different heating functions induced by various squall lines may have different effects on the system-associated mass and wind fields, and also their subsequent evolution. Thus, the main objective of this chapter is to illustrate the heating and moistening features of the 26-27 June squall line, show the differences in the evolution of the heating and moistening profiles for the convective and stratiform regions, compare the vertical profiles to other midlatitude and tropical cases, and check the budget-calculated rainfall rates with surface observational rainfall data.

5.1 Spatial and temporal evolution of the heat budget

The contribution to the apparent heat source Q_1 comes mainly from three different mechanisms: radiative heating or cooling, latent heating or cooling, and vertical eddy heat flux (refer to Eq. 2.1).

The vertical cross-sections of Q_1 averaged over the entire squall line at six budget times are illustrated in Figure 5.1. Consistent with the evolution of vertical velocity throughout the life cycle of the squall line, the levels of peak heating remained almost the same (centered at about 550 hPa), which is lower than that found in the 10-11 June case (400 hPa) (Gallus and Johnson 1991). The approximation of $Q_1 \propto -\bar{\omega}$ found by Houze (1982) and Johnson and Young (1983) is quite evident in this case. The maximum heating rate (near the leading edge) increased from about 5.5 °C h^{-1} at 2100 UTC to 5.9 °C h^{-1} and 6.0 °C h^{-1} at 2230 and 0000 UTC and reached nearly 7.2 °C h^{-1} at 0130 UTC (the developing and mature stages), and then decreased to 6.0 °C h^{-1} at 0300 UTC and less than 4.2 °C h^{-1} at 0430 UTC (the dissipating stage). In agreement with the observation showing that the squall line remained narrow, the tilting of the vertical heating band was very small during the period of study except at 0300 and 0430 UTC. At the back edge of the squall line, evaporational cooling occurred through nearly the whole depth of the troposphere except at 2100 UTC, at which time there was relatively weak heating at middle and low levels. There were two cooling peaks to the rear of the system at middle and low levels, respectively. As time progressed, the cooling rate of the higher peak increased and the level rose from 650 hPa up to 550 hPa, a level similar to that found by Gallus and Johnson (1991).

As depicted on the radar map (Fig. 4.1b), there was a 40 $\sim$ 70-km-wide stratiform region behind the convective line over Kansas at 2100 UTC. Some features of the stratiform region can be seen at the back edge of the squall line in the system-averaged vertical cross section (Fig. 5.1a). However, some of the heating at 2100 UTC to the rear of the system (150 − 300 km) may not be real, but rather a result of aliasing into a region with little data. At other times, the squall line was well covered by data.

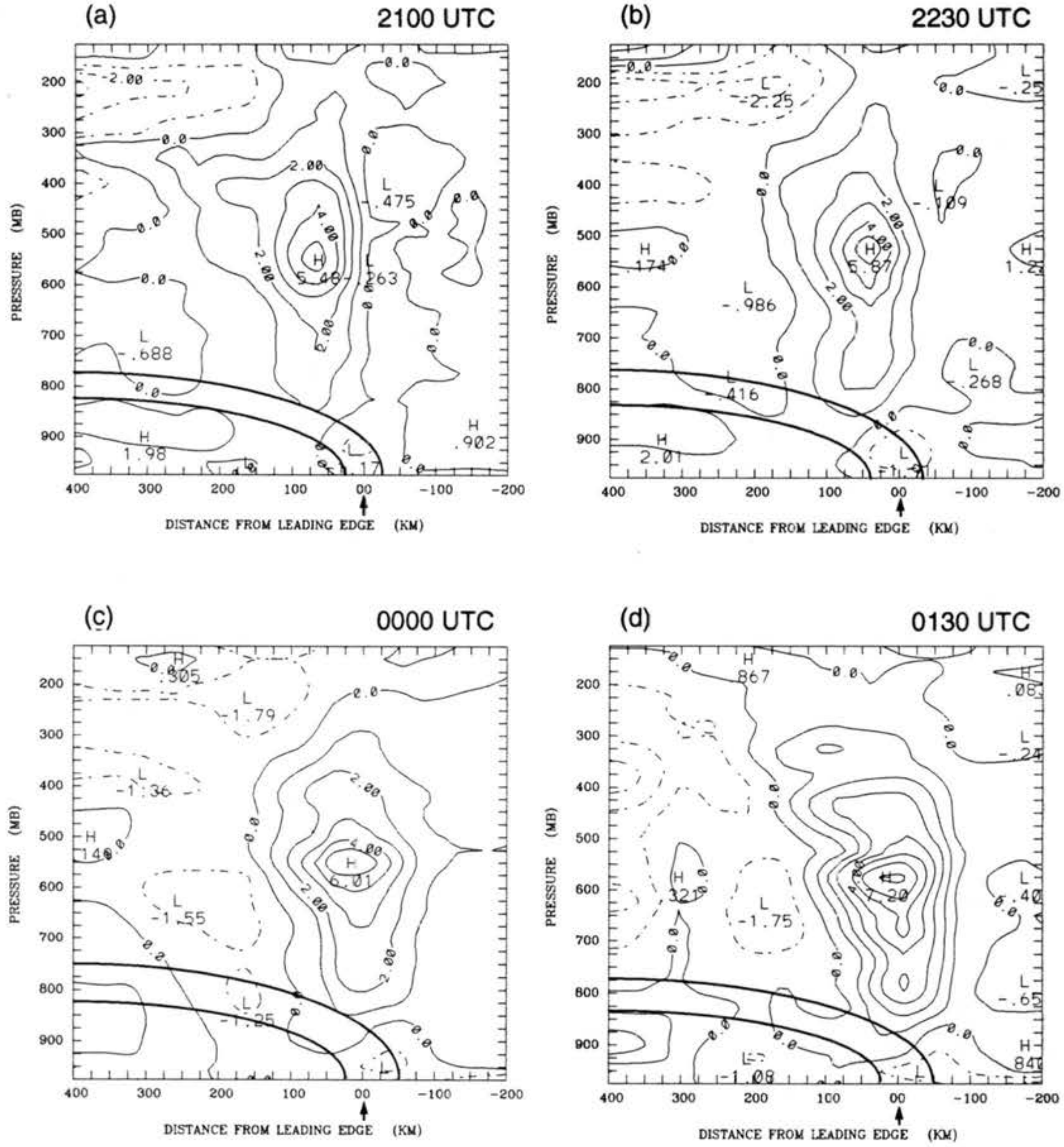

Figure 5.1: Apparent heat source Q_1 (in °C h^{-1}) at a) 2100 UTC, b) 2230 UTC, c) 0000 UTC, d) 0130 UTC, e) 0300 UTC, f) 0430 UTC. The low-level frontal zone is approximately represented by isentropes 300 K and 305 K. Arrow marks leading edge.

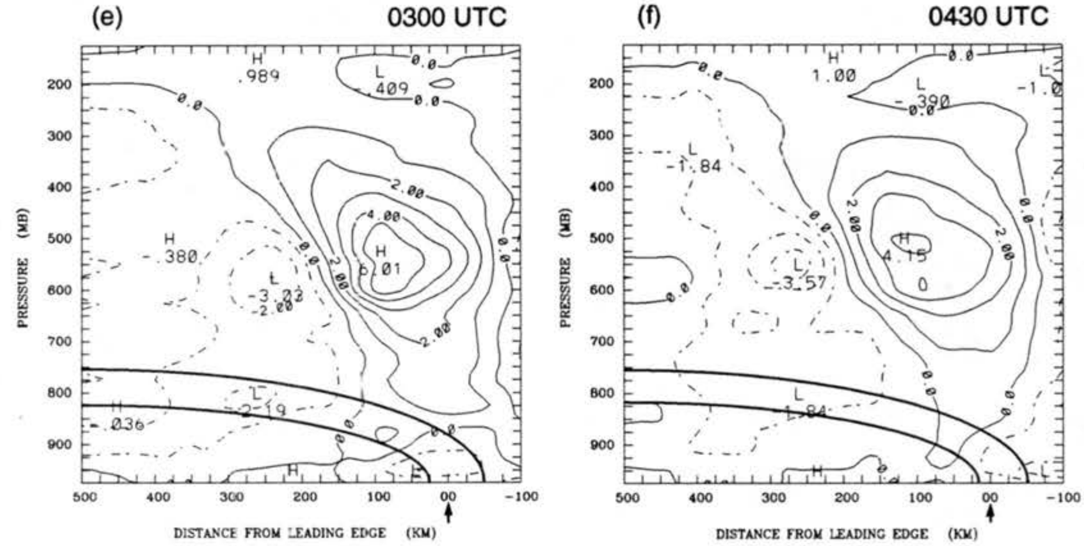

Figure 5.1: Continued.

Studies of the vertical heating profiles in the convective region of mesoscale convective systems have placed the heating peak anywhere from the low to middle troposphere (Houze 1989). Houze pointed out that the variation in the level of peak heating may be accounted for by the natural variability in the convective heating profiles from one type of organized convective system and/or large-scale environment to another. The 26-27 June case, in which the system was dominated by the convective region during the early stages, provided some evidence of heating features within the convective region. Figure 5.2 shows the vertical profiles of Q_1 and the evolution in the convective region from 2100 to 0300 UTC. Latent heating (including condensation, deposition and freezing) can be seen to be dominant within a deep layer between 875 and 300 hPa. In common with other studies (Houze 1982; Johnson 1984), the heating peak in the convective region was located at middle levels (about 550 hPa in this case) and the magnitudes remained quite constant throughout the developing, mature, and the dissipating stages. Weak evaporational cooling occurred at low levels below 900 hPa with similar magnitudes between $0.5 \sim 1.0$ $^{\circ}\mathrm{C\,h^{-1}}$.

Figure 5.3 exhibits the vertical profiles and time evolution of the Q_1 field in the stratiform region from 2230 to 0430 UTC. Heating released primarily by condensation and deposition induced by mesoscale updrafts within the anvil clouds is apparent between 600 and 200 hPa. During 2230 and 0000 UTC, the peak heating was centered at about 550 hPa. It was likely that some features of the convective region might be aliased into the profiles since the stratiform region was quite narrow at these times. At later times, the peak shifted upward slightly and was generally located between 450 and 475 hPa. Below 650 hPa, very weak heating was present from 2230 to 0130 UTC. By 0300 and 0430 UTC, there was weak cooling due to evaporation and melting with the peak centered between 700 and 800 hPa, a result similar to those determined by Houze (1982), Johnson and Young(1983) and Johnson (1984).

Houze (1982) and Johnson (1984) found that the convective and stratiform regions have distinctly different contributions to the large-scale latent heat budget. In the convective region, strong condensation, deposition and freezing resulting from cumulus updrafts

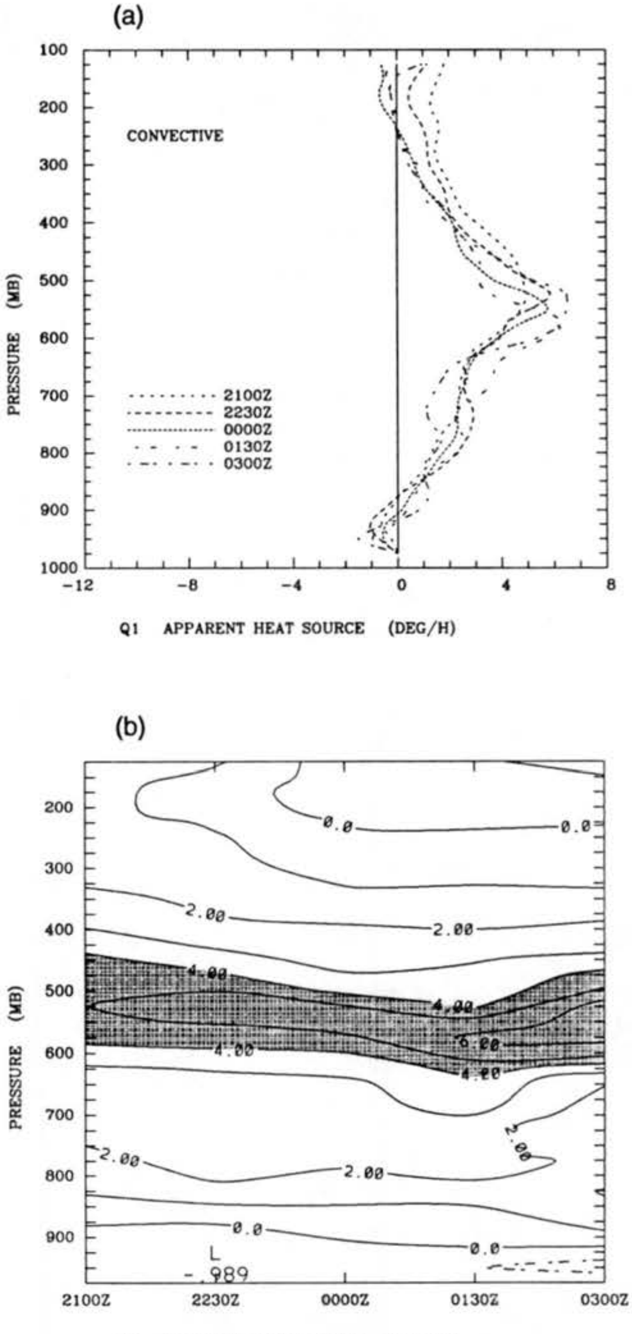

Figure 5.2: Vertical profiles (a) and time evolution (b) of Q_1 (in °C h^{-1}) averaged over the convective region of the squall line at different budget times from 2100 to 0300 UTC. Shading area represents a region where $Q_1 > 4.0$ °C h^{-1} .

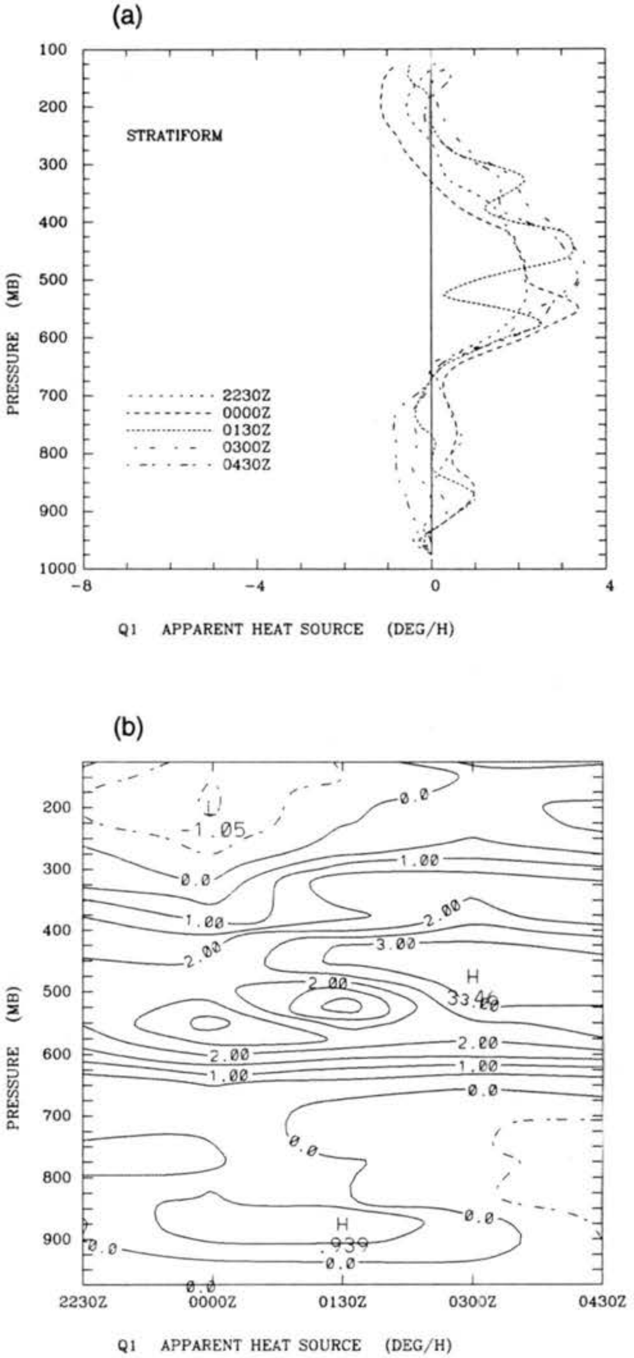

Figure 5.3: Vertical profiles (a) and time evolution (b) of Q_1 (in °C h^{-1}) averaged over the stratiform region of the squall line at different budget times from 2230 to 0430 UTC.

dominate through the full depth of the troposphere and the heating peak is generally located at middle levels. In the stratiform region, condensation and deposition take place in mesoscale updrafts at middle and high levels, evaporation occurs in mesoscale downdrafts at low levels and melting occurs near the 0° level. The heating profiles usually show a heating peak at high levels (about 400 hPa) and a cooling peak at low levels (near 700 hPa).

Figure 5.4 shows the vertical Q_1 profiles and their time evolution averaged over the entire system from 2100 to 0430 UTC. The contribution to the Q_1 profiles at early times (2100 to 0130 UTC) mainly came from the heating in the convective region. The heating peak was generally located at middle levels (between 500 and 550 hPa). At later times (0300 to 0430 UTC), the heating rate gradually decreased and became negative between 700 and 975 hPa, which indicated increasing evaporational cooling resulting from the stratiform region and the weakening convective line. The heating peak at middle levels moved slightly higher, but was still lower than those found in the 10-11 June case (Gallus and Johnson 1991) in which the stratiform region was more than three times as extensive as the convective region. In that case, the upper level heating feature from the stratiform region dominated the system average. Another important reason for the midlevel heating peak for the entire system might be that the 26-27 June case had weaker updrafts compared to the 10-11 June case. Johnson and Hamilton (1988) calculated the convective available potential energy (2300 m^2 s^{-2} at station PTT at 2230 UTC) (CAPE; Moncrieff and Miller 1976; Weisman and Klemp 1982) in the 10-11 June case. In the 26-27 June case, the CAPE values for stations were generally smaller and most of them were below 1700 m^2 s^{-2} (e.g., 1675 m^2 s^{-2} for station OKC at 2300 UTC 26 June). Thus the released latent heat was primarily concentrated at middle levels.

It is interesting to notice that above 200 hPa heating was diagnosed at 2100 and 2230 UTC (during the afternoon) and this heating turned into cooling (maximum roughly -0.6 °C h^{-1}) after 0000 UTC (around sunset). The evolution and magnitudes of Q_1 within the entire system are quite consistent with the expected radiative effects at the top of clouds (radiative warming in the afternoon and cooling in the evening, e.g., Webster and Stephens

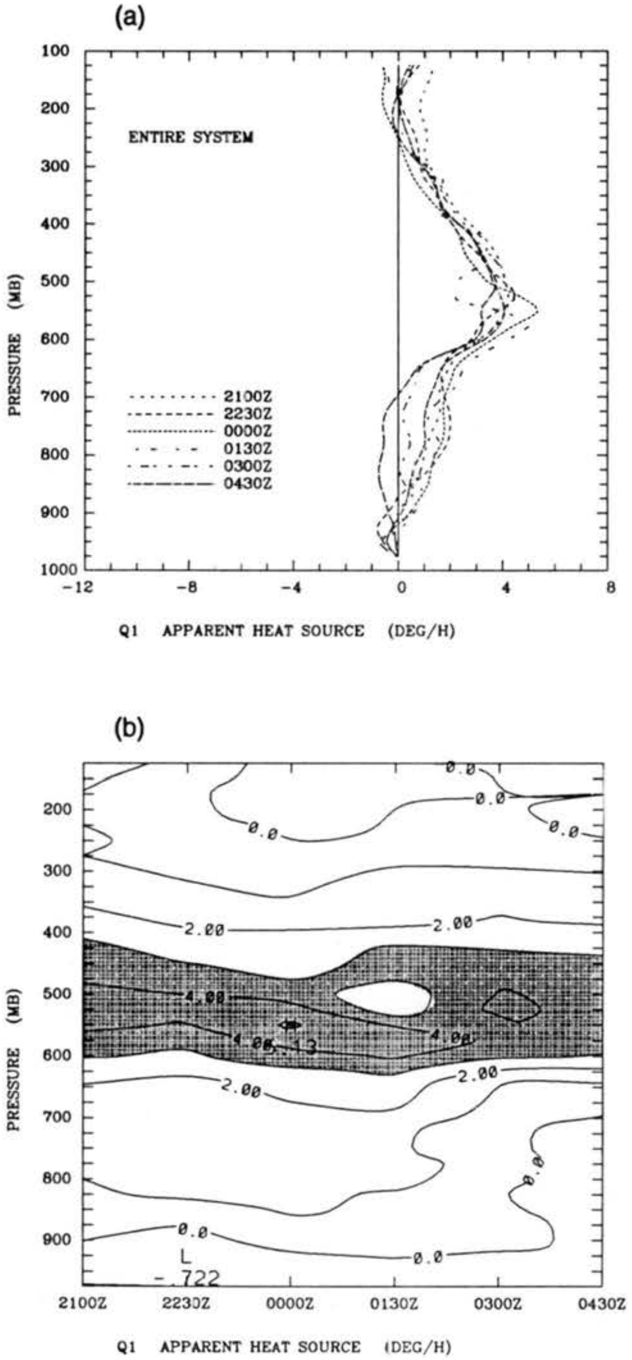

Figure 5.4: Vertical profiles (a) and time evolution (b) of Q_1 (in °C h^{-1}) averaged over the entire system of the squall line at different budget times from 2100 to 0430 UTC. Shading area represents a region where $Q_1 > 3.0$ °C h^{-1} .

1980). However, in the 26-27 June case, the upper level features should be viewed with caution since they were near the highest level; real features might be distorted by paucity of sounding data at high levels and the calculation method of vertical velocity.

Dividing the heating rates by observed precipitation rates, we can get normalized rates which make it possible to compare vertical profiles among different cases. Figure 5.5 compares the normalized heating rates for the entire system in the 26-27 June case to several other tropical and midlatitude convective systems. Curve GJ (from Gallus and Johnson 1991) was determined from the well-organized 10-11 June PRE-STORM squall line case during the late mature through decaying stages, in which a more extensive stratiform region (roughly 160 km wide) trailed the convective region. Curve Y (from Yanai et al. 1973) and curve T (from Thompson et al. 1979) were both estimated from tropical cases. The former is from the Pacific Marshall Islands and the latter is from the eastern Atlantic GATE area. The results of this study resemble those from Gallus and Johnson (1991) except the level of peak heating is much lower in this case. Both midlatitude studies show a pronounced effect of evaporative cooling at low levels. The depth of this low level cooling progressively increased as the squall line decayed. In the tropics, since air normally contains more water vapor and cloud bases are lower, evaporational cooling is smaller than in midlatitude cases. Therefore, both curves Y (Yanai et al. 1973) and T (Thompson et al. 1979) show heating at low levels instead of the weak cooling shown in the PRE-STORM cases.

As Houze (1982) pointed out, the middle level maximum heating in the convective region combined with the upper level peak heating in the stratiform region form a system-averaged heating peak between middle and high levels. The 10-11 June case (curve GJ) had a higher heating peak (at about 400 hPa) than the 26-27 June case (between 500 and 550 hPa). The former case was generally dominated by the stratiform region during the late mature and decaying stages, while in the latter case the system-averaged heating primarily came from the contribution of the convective region during the early times and from the contribution of both the convective and stratiform regions at later times. However, the levels of the heating peak turned out to be quite constant. The heating

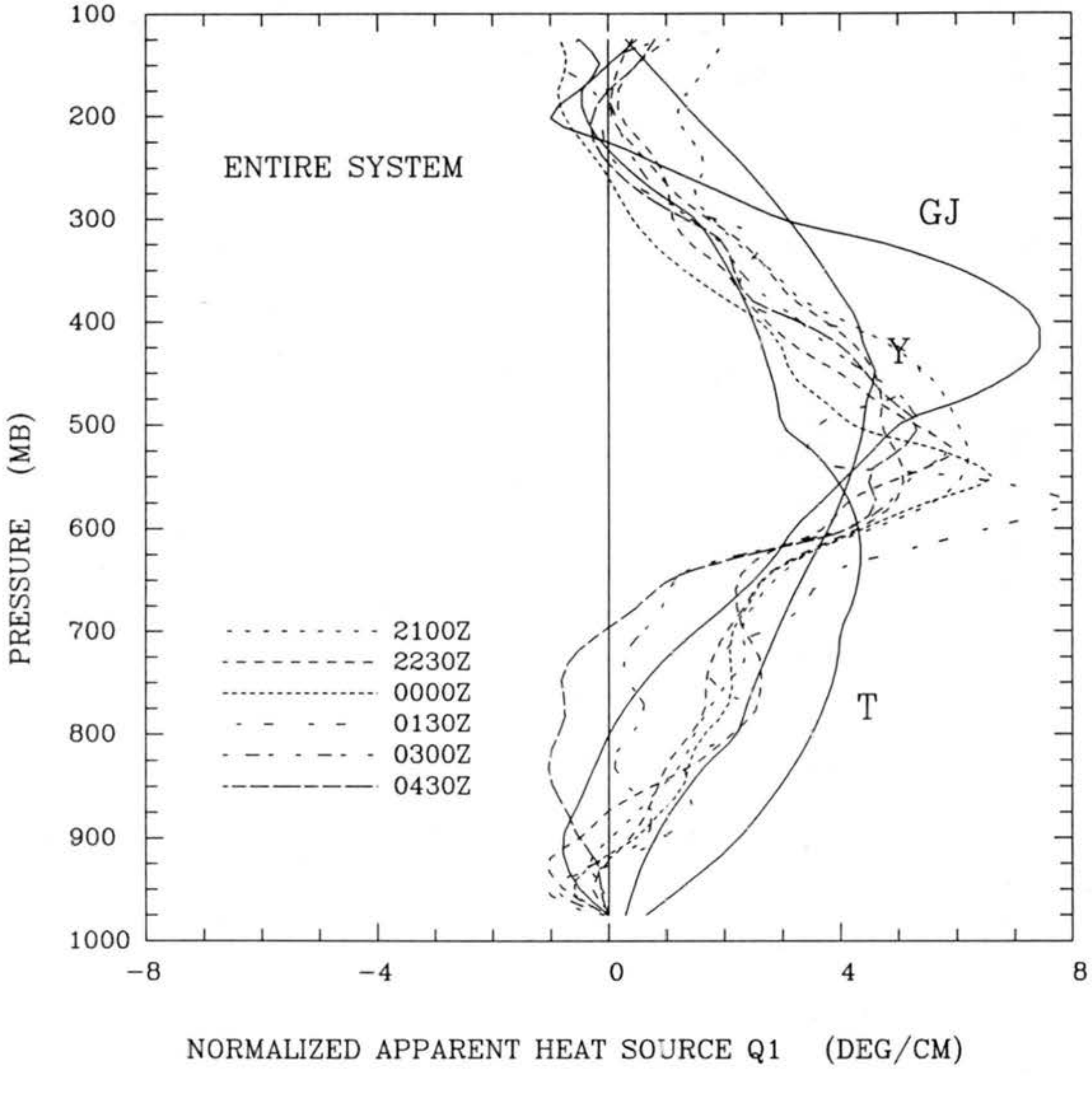

Figure 5.5: Comparison of vertical Q_1 profiles normalized by the rainfall rate for average taken over the entire system (in unit of Deg Day^{-1}/1 cm Day^{-1}). Curve GJ is from the 10-11 June PRE-STORM case (Gallus and Johnson 1991). Curve Y and T are from tropical Pacific islands (Yanai et al. 1973) and GATE (Thompson et al. 1979), respectively.

peak of curve Y is located at about 450 hPa, just between the above two curves. Curve T has a lower heating peak which is located at about 600 hPa, which Thompson et al. (1979) attributed to the different cloud population under the influence of local large-scale environment in the GATE region. The above analyses provide some indication that the actual location of the heating peak in the vertical for the entire convective system depends on the large-scale environment, the strength of updrafts, and also depends significantly on the relative area covered by the stratiform region and the convective region in the entire system.

Johnson and Young (1983), using WMONEX sounding data at 6-hour intervals from three ships, calculated the components of the heat and moisture budgets. They found the vertical advection term is the primary contributor to the Q_1 and Q_2 budgets. With more intense PRE-STORM sounding data and shorter time intervals, the components were calculated to check the results in this midlatitude squall line. The system-averaged vertical profiles of each component of Q_1 shown in Figure 5.6 reaffirmed their conclusion that the storage term and horizontal advection term are small compared to vertical advection term throughout most of the troposphere. However, at low levels near the surface, where the vertical advection term approaches zero, the storage and horizontal advection terms play a more important role. Cooling rates of $\sim 1.0 - 2.0$ °C h^{-1} occurred at low levels in the profiles of the storage term, while heating rates of $\sim 0.5 - 1.0$ °C h^{-1} can be noticed in the profiles of the horizontal advection term. It can be clearly seen that the low level cooling near the surface which is uniquely found in midlatitude MCSs mainly results in this case from the net effect of the storage and horizontal advection terms. This result is associated with the low level frontal nature of the system. The horizontal advection term shows cold advection connected with the front, but the local temperature change is slightly larger, indicating the pronounced cooling effects of rainfall evaporation.

5.2 Spatial and temporal evolution of the moisture budget

Q_2 is a measure of the drying when water vapor condenses into liquid water or ice, the moistening when liquid water evaporates into vapor, and vertical divergence of the

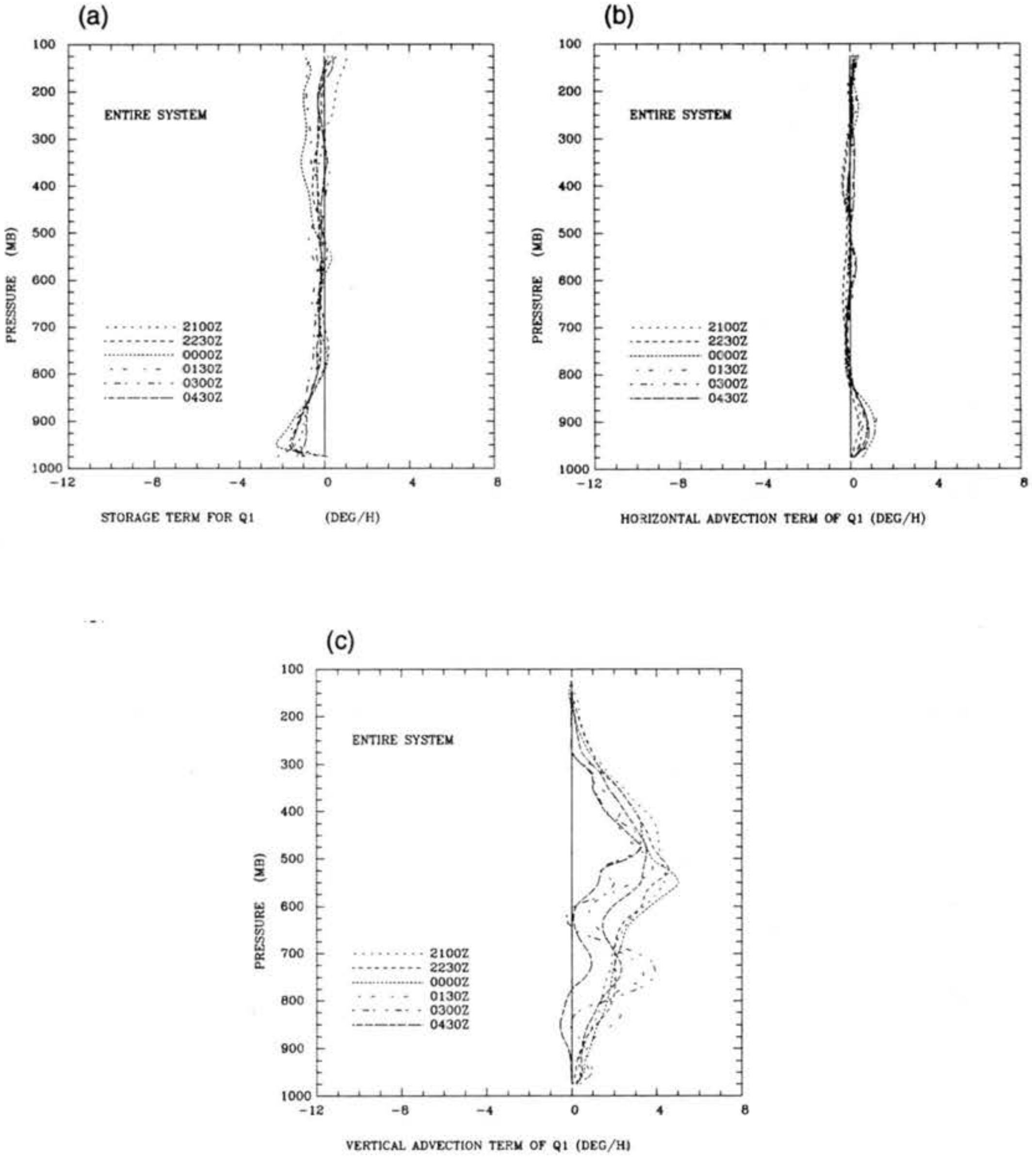

Figure 5.6: Components of apparent heat source Q_1 (in °C h^{-1}) averaged over the entire system of the squall line at different budget times from 2100 to 0430 UTC. a) local tendency term $\frac{\partial \bar{s}}{\partial t}$, b) horizontal advection term $\bar{\mathbf{v}} \cdot \nabla \bar{s}$, c) vertical advection term $\bar{\omega} \frac{\partial \bar{s}}{\partial p}$.

eddy moisture flux (refer to Eq. 2.2). Since the radiative effect does not appear in the Q_2 equation, it might be expected that Q_2 can better depict the latent heat evolution process within convective systems than Q_1, except that water vapor is difficult to measure accurately everywhere.

The vertical cross sections for the Q_2 field are delineated in Figure 5.7. Because water vapor is basically concentrated at middle and low levels and is easily modified by local small scale motion, the soundings may occasionally show narrow dry or moist layers. Compared to the Q_1 field, in which the variability of dry static energy affected by the local small scale features is not so large, the Q_2 field is noiser. However, quite consistent features are still present in this case.

At 2100 UTC (Fig. 5.7a), near the leading edge, condensational drying can be clearly noticed within a vertical band about 100 km wide. There were two drying peaks shown in this vertical band, similar to those revealed in other budget studies. The larger one (4.1 °C h^{-1}) was located at 475 hPa 60 km behind the leading edge and the other one (4.0 °C h^{-1}) about 200 hPa below. At high levels (nearly 350 hPa), similar to that shown in Q_1 field, Q_2 exhibited a drying extension at 150 km behind the leading edge.

Negative values generally dominated to the rear of the system, indicating the moistening due to evaporation of liquid water in the atmosphere and at the surface. An interesting feature is the rearward extension of apparent drying at 725 hPa just at the back edge of the system at 2100 UTC. At the same time, evaporational moistening of similar magnitude extended from 700 hPa, 400 km behind the leading edge down into the rear of the system. This structure is probably due to the low-level cold front, which gradually caught up with the squall line, forcing the air mass with abundant water vapor content ahead of the front to rise along the front. The water vapor condensed into liquid water by adiabatic cooling, resulting in the rearward drying feature. Although liquid water might form at this position, strong evaporation in the dry atmosphere behind the cold front at low levels almost completely evaporated it before reaching the surface. Therefore, there was little precipitation at the surface.

The 26-27 June squall line exhibited a complicated and asymmetric evolution pattern. At 2230 UTC (Fig. 5.7b), as the stratiform region over Kansas gradually dissipated, the

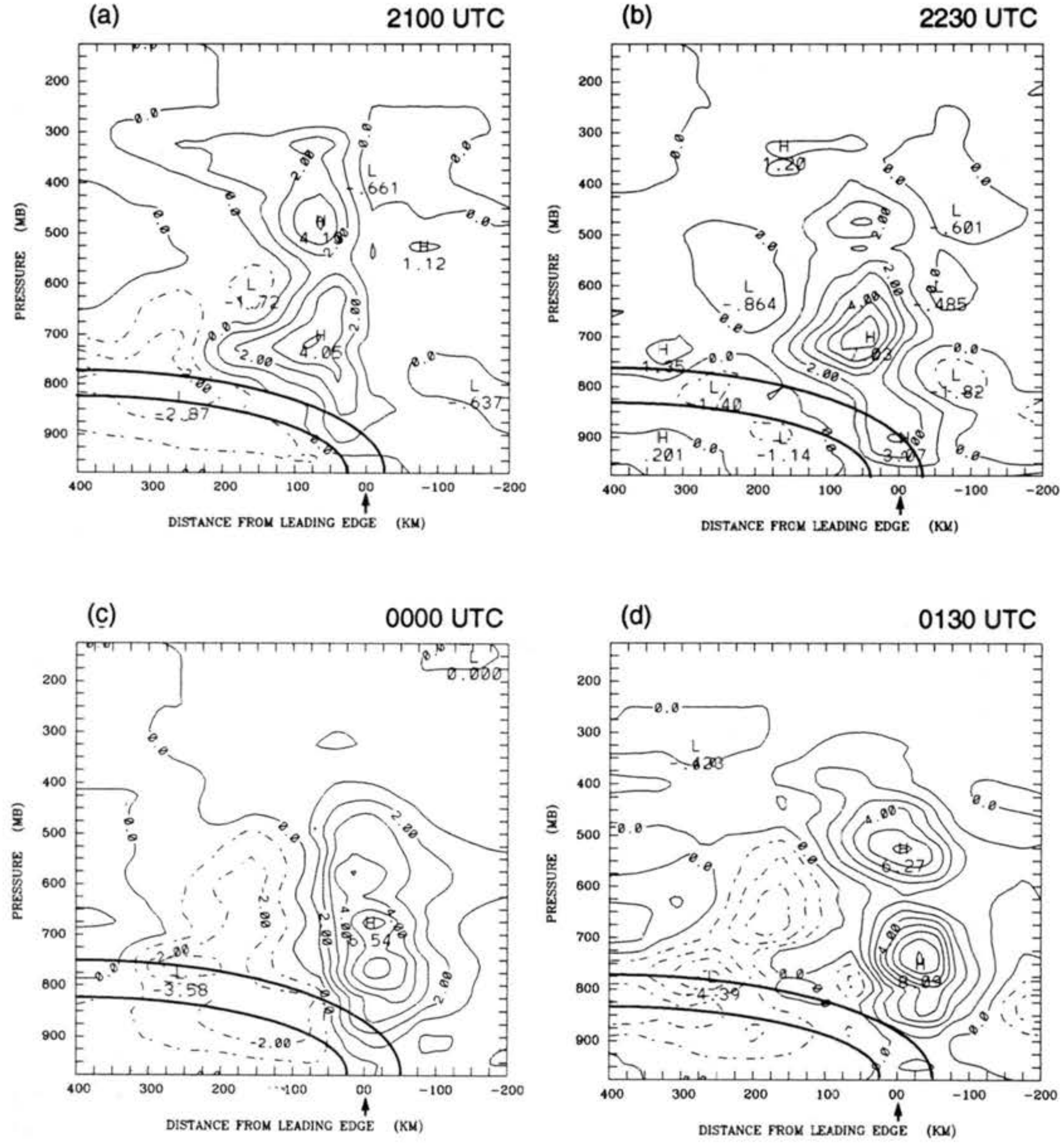

Figure 5.7: Apparent moisture sink Q_2 (in °C h^{-1}) at a) 2100 UTC, b) 2230 UTC,c) 0000 UTC, d) 0130 UTC, e) 0300 UTC, f) 0430 UTC. The low level frontal zone is approximately illustrated by isentropes 300 K and 305 K. Arrow marks the leading edge.

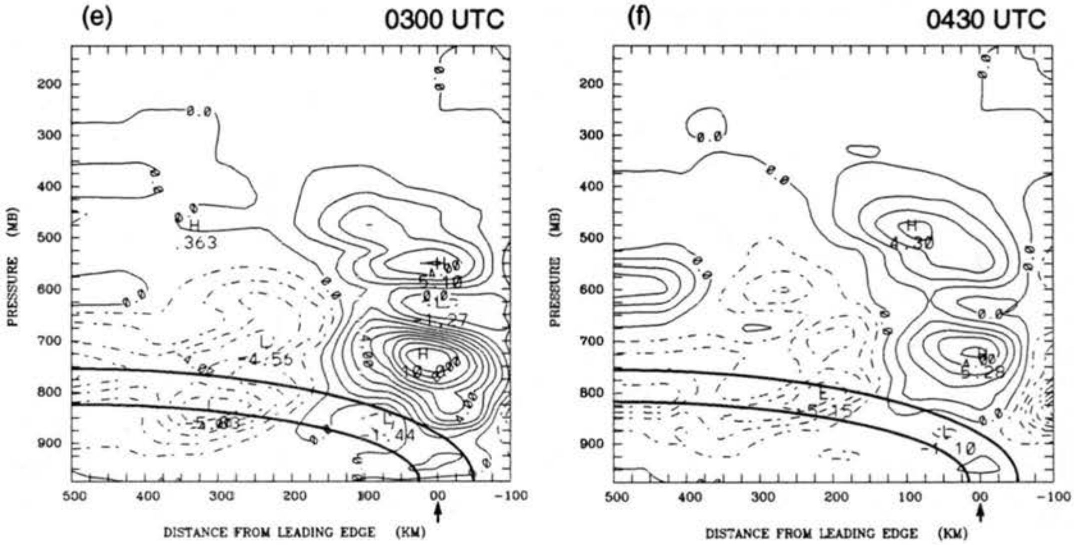

Figure 5.7: Continued.

features from the convective region dominated the entire system. The larger drying peak (7.0 °C h^{-1}) now was located at 700 hPa. The middle level drying peak weakened (about 3.0 °C h^{-1}) and was located at 450 hPa. To the rear of the system, evaporational moistening occurred from 500 hPa to the surface. At 2230 UTC, the region of drying resulting from uplifting of moist air along the cold front can still be noticed above 750 hPa while evaporational moistening resulting from the cold front was present below. However, a similar structure was not observed in the Q_1 field.

At 0000 UTC (Figure 5.7c), the larger drying peak was still located at low levels between 700 and 800 hPa, but the drying at middle levels became quite uniform. The middle level drying peak was not prominent.

As the system evolved into its mature and dissipating stages at 0130 and 0300 UTC, both the peak drying rates at low and middle levels increased and a double-peak structure became prominent again in the vertical. The larger peak was located at roughly between 750 and 700 hPa with a magnitude of 8.1 °C h^{-1} at 0130 UTC and 10.0 °C h^{-1} at 0300 UTC. The second peak was located at 550 hPa and reached 6.3 °C h^{-1} at 0130 UTC and 5.1 °C h^{-1} at 0300 UTC. Since the system remained quite narrow, tilting was not apparent. Similar to the 10-11 June case (Gallus and Johnson 1991), the Q_2 field was usually displaced forward during the dissipating stage. The reason is that since the convective region was near the edge of sounding network, the features within the convective region were smoothed forward. At 0430 UTC, the double drying peaks weakened significantly.

As discussed in the last section, many studies have noticed that the Q_1 profile has a good corresponding relationship with vertical velocity (Houze 1989). Since the vertical advection term generally dominates Q_1 , it indicates that $\partial\bar{s}/\partial p$ is nearly constant. Actual observations confirmed the quasi-linear relationship between dry static energy and pressure throughout most of the troposphere. Q_2 differs from Q_1 since moisture is much more sensitive to cumulus convection and the term $\partial\bar{q}/\partial p$ may vary significantly, particularly in the middle to lower troposphere.

The vertical profiles and time evolution of Q_2 averaged over the convective region are illustrated in Figure 5.8. Within the convective region, the Q_2 profiles are generally noisier than the Q_1 profiles and have larger variations. Drying is shown at almost all levels and there is little indication of moistening near the surface, although the Q_1 profiles suggested evaporational cooling there. The larger drying peak at different times was generally located at about 700 hPa, about 150 hPa lower than Q_1 heating peak, indicative of strong deep convection (Luo and Yanai 1984).

At 2100 UTC, the peak drying value was around 4 °C h^{-1} and was quite uniform between 600 to 750 hPa. Similarly, the Q_2 profile also showed uniform drying between 550 and 850 hPa at 0000 UTC. At 2230 UTC, a strong drying peak (7.1 °C h^{-1}) was shown around 700 hPa. There was also a secondary drying peak located at 450 hPa, but its magnitude was much smaller than the lower one. Thus, during the early stage, the double-peak structure was not as pronounced, although a uniform drying rate was shown at middle and low levels at 2100 and 0000 UTC.

At later times (0130 to 0300 UTC), there was a drying minimum developing between 600 to 675 hPa, as found in many tropical and midlatitude budget studies (Reed and Recker 1971; Yanai et al. 1973; Johnson 1976; Frank and McBride 1989; Gallus and Johnson 1991; Johnson and Bresch 1991; etc). It seems that the drying minimum split the drying peak and resulted in the double drying peak structure at 750 and 500 hPa, respectively.

The vertical profile of Q_2 averaged over the entire system (Figure 5.9) resembles Fig. 5.8. However, some differences can still be noticed. Similar to the Q_1 profiles, almost all the Q_2 profiles show evaporational moistening near the surface. At 0430 UTC, both the Q_1 and Q_2 profiles show heating or drying at middle and high levels and weak cooling or moistening at low levels. They compare very well to each other.

During the evolution of the 26-27 June squall line, although the convective region and the stratiform region coexisted, the convective region generally dominated the contribution to the entire system except at the dissipating stage. This is confirmed by the apparent separation of the Q_1 and lower Q_2 peaks which Luo and Yanai (1984) suggested as an indicator of deep convection.

Although the relationship between the separation of the Q_1 and lower Q_2 peaks and deep convection has been clarified by a number of budget studies, the cause for the

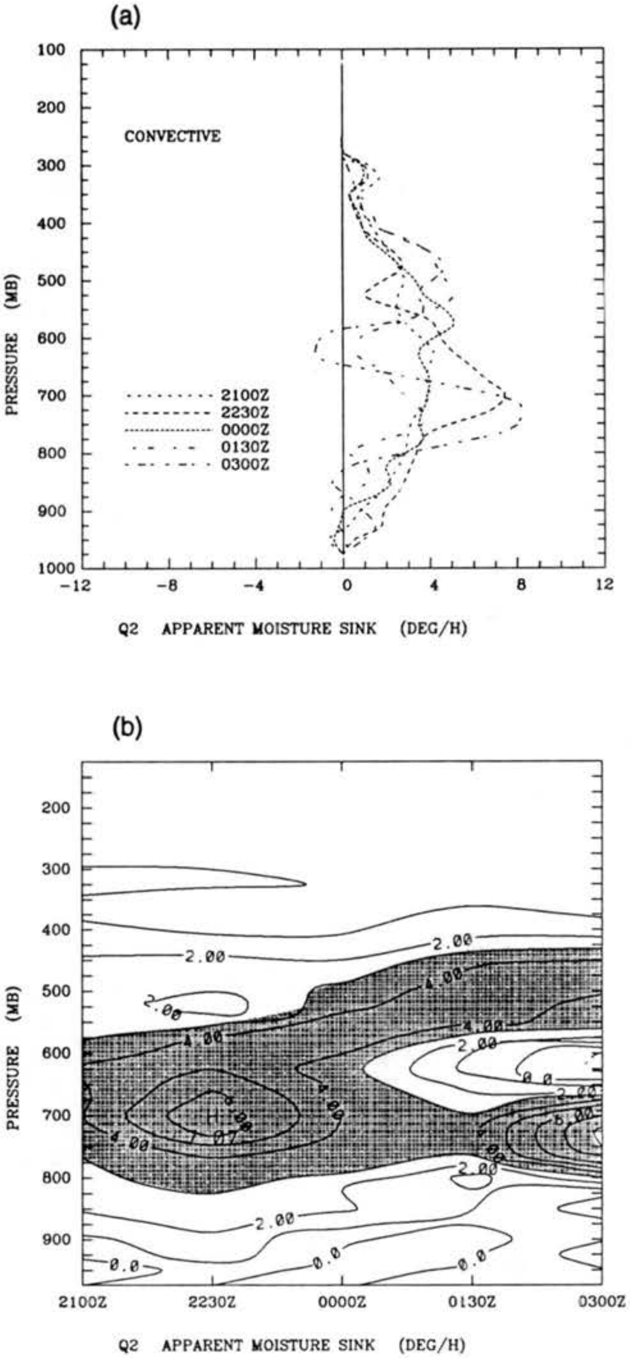

Figure 5.8: Vertical profiles (a) and time evolution (b) of Q_2 (in °C h^{-1}) averaged over the convective region of the squall line at different budget times from 2100 to 0300 UTC. Shading area represents a region where $Q_2 > 3.0$ °C h^{-1} .

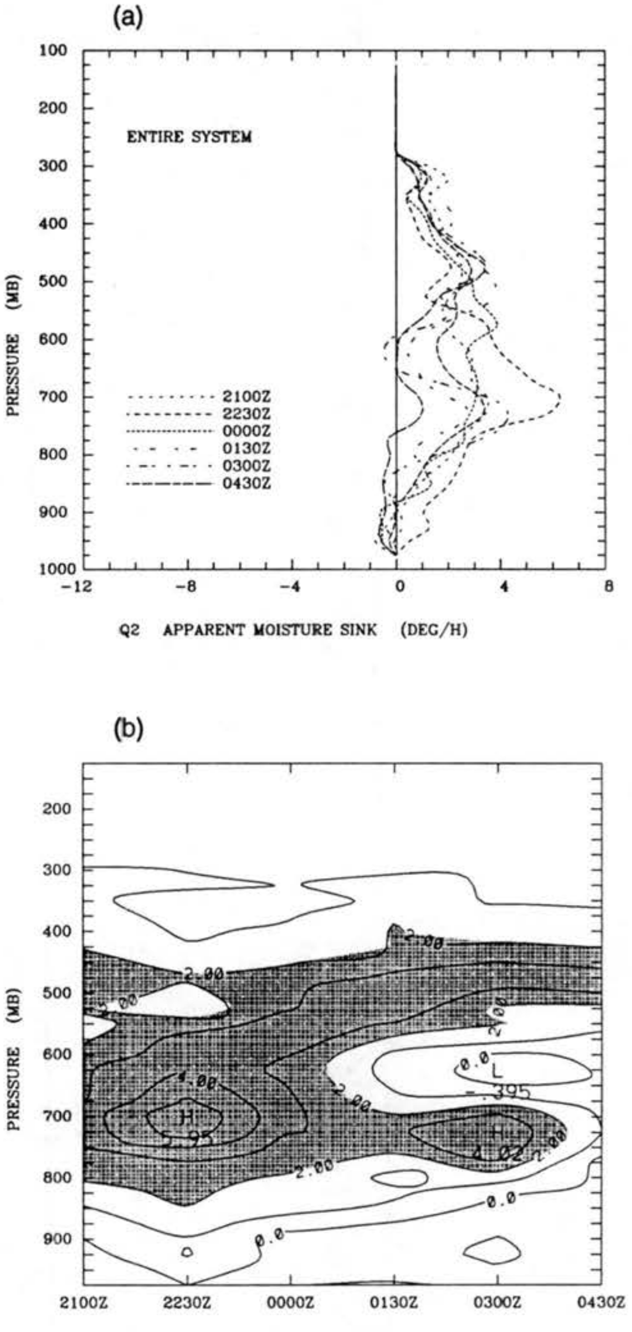

Figure 5.9: Vertical profiles (a) and time evolution (b) of Q_2 (in °C h^{-1}) averaged over the entire squall line at different budget times from 2100 to 0430 UTC. Shading area represents a region where $Q_2 > 2.0$ °C h^{-1} .

mid-tropospheric drying peak is still under investigation. Johnson (1984) proposed that the double-peak Q_2 structure is a result of the combination of two distinctly different drying processes. He suggested that the lower peak is a result of cumulus updrafts in the convective region while the higher one comes from the mesoscale updrafts within anvil clouds. This hypothesis is supported by the results of Esbensen et al. (1988) and Gallus and Johnson (1991). Recently, the importance of vertical eddy transport of water vapor in the Q_2 profile has been investigated (Tao and Soong 1986; Dudhia and Moncrieff 1987; Lafore et al. 1988; Chong and Hauser 1990). Dudhia and Moncrieff (1987) and Lafore et al. (1988) suggested a different interpretation of the double-peak Q_2 structure. Their results showed that the vertical convective eddy transport of water vapor can play an important role on Q_2 profiles and may cause the higher drying peak in the double-peak structure. Although the exact nature of the mid-tropospheric drying peak of Q_2 profiles is still unclear, it is assumed that the coexistence of the convective and stratiform precipitation or strong eddy transport of water vapor by deep convection or a combination of both may result in the structure (Johnson 1992).

Convection was most intense during the early stage of the 26-27 June squall line. At 2230 UTC, the apparent separation of the Q_1 peak (500 hPa) and both Q_2 peaks (about 700 and 450 hPa) implied deep convection and suggested that the contribution from the stratiform region was small. This is confirmed by radar echo and surface observational rainfall data which showed a narrow stratiform region trailing the convective region. It seems that the mechanism of vertical eddy transport of water vapor (Tao and Soong 1986; Dudhia and Moncrieff 1987; Lafore et al. 1988; Chong and Hauser 1990) is appropriate to be applied here. The interpretation at 2100 and 0000 UTC is a little more difficult, since a $40 - 70$ km wide dissipating stratiform region trailed the convective line over Kansas at 2100 UTC and the stratiform region gradually developed to the rear of the system at 0000 UTC. Although the low level drying peak was still quite intense, which indicates deep convection as proposed by Luo and Yanai (1984), the Q_2 profile was relatively uniform at middle and low levels compared with that at 2230 UTC. There was no apparent drying peak to coincide with the Q_1 peak at 550 hPa. During these two times, both mechanisms suggested above may be combined to produce the above uniform feature.

During the mature and dissipating stages of the squall line (0130 to 0300 UTC), not only was there a large drying peak at 700 hPa, but the mid-level Q_2 peak was also coincident with the Q_1 peak at about 500 hPa. This is consistent with the radar echo and surface rainfall observation showing that the stratiform precipitation gradually developed and coexisted with the convective precipitation during the later times. It is believed that the mid-level drying peak is mainly caused by the stratiform region.

Figure 5.10 compares the normalized profiles of Q_2 averaged over the entire system with some other tropical and midlatitude cases. In the 10-11 June PRE-STORM case (curve GJ), the system was at the late mature and dissipating stages, and the squall line was characterized by an extensive stratiform region (about 160 km wide). The midlevel drying peak resulting mainly from the mesoscale updrafts within the stratiform region was very pronounced and was located at about 450 hPa. The low level drying peak resulting from convective updrafts, although it can be noticed, was quite weak and located at 825 hPa. In the 26-27 June case, the system showed a different evolution from the developing and mature, through the dissipating stages. At the developing and early mature stages, the convective region dominated the contribution to the entire system. The maximum drying peak, which resulted from convective updrafts, was located between 700 and 750 hPa. At the late mature and dissipating stages (0130 to 0300 UTC), the double-peak structure became apparent and the magnitude and position were quite similar to the Y curve (Yanai et al. 1973). At 0430 UTC, the low level drying peak decreased rapidly. Weak moistening was dominant below 750 hPa to the surface. The middle level drying peak became prominent and was located at a similar position as the 10-11 June case (GJ curve) (Gallus and Johnson 1991).

5.3 Comparison of diagnosed and observed rainfall rates

By integration of Q_1 and Q_2, the diagnosed rainfall rates can be determined from the large scale budget study. They can be used to compare with the actual rainfall rates observed from surface PAM and SAM stations to check the reliability of the budgets. Many

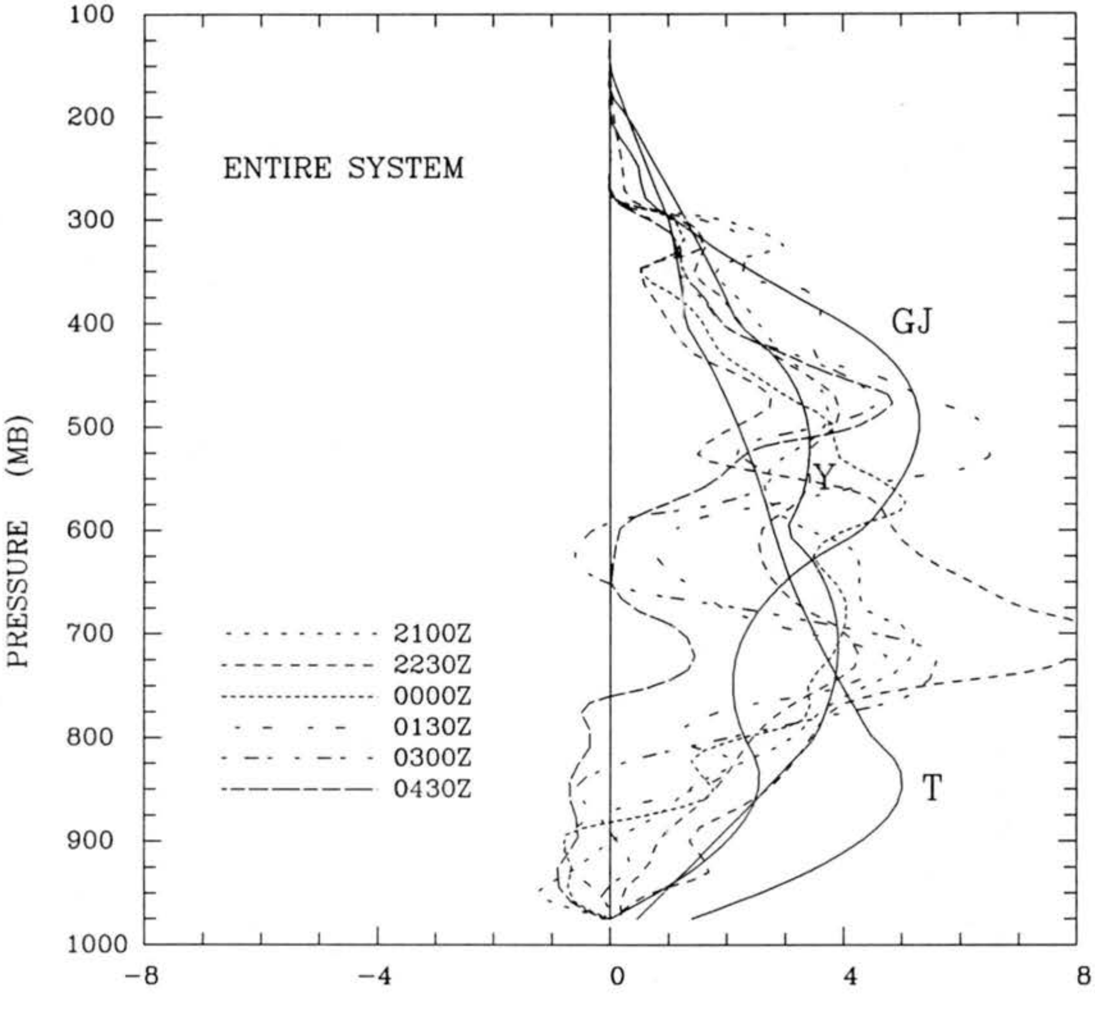

Figure 5.10: Comparison of vertical Q_2 profiles normalized by the rainfall rate for average taken over the entire system (in unit of Deg Day^{-1}/1 cm Day^{-1}). Curve GJ is from the 10-11 June PRE-STORM case (Gallus and Johnson 1991). Curve Y and T are from tropical Pacific islands (Yanai et al. 1973) and GATE (Thompson et al. 1979), respectively.

previous budget studies have been unable to perform these checks due to limitations in both sounding and surface data.

For the 26-27 June squall line, radiative effects and surface sensible and latent heat fluxes are considered small compared to the large condensation/evaporation terms so that their effects are neglected. However, the liquid water storage term is not necessarily small, especially during the organizing and developing stages of the squall line (Gallus and Johnson 1991). Due to strong cumulus updrafts and an expanding cloud field, part of the condensate may remain within the clouds and not fall to the ground as precipitation. Some portion may stay at the same place, while some may be transported elsewhere by the system-relative flow. It may fall to the ground as precipitation at later times when the updrafts become weaker. This feature can cause some inconsistencies during the comparison of the predicted and observed rainfall rates (McNab and Betts 1978; Johnson 1980).

Figure 5.11 shows the observed surface rainfall rates at six budget times, which were derived from accumulated rainfall data and averaged over a 20-minute period centered at each budget time. Because of measurement errors and the influence of small scale phenomena, the observed rainfall rates occasionally exhibit irregular patterns, as found in many rainfall data analyses. A subjective analysis was applied to perform contouring.

At 2100 UTC (Fig. 5.11a), it can be clearly noticed that there were two separated large rainfall rate bands along the leading edge over Kansas and Oklahoma. The maximum rainfall rates exceeded 40 and 30 mm h^{-1} , respectively. There was also a circular maximum on the Oklahoma side near the border of these two regions. The system asymmetry is quite evident at this time. Over Oklahoma, the squall line was dominated by the convective region, and the stratiform region trailing the convective line (with rainfall rate less than 6 mm h^{-1}) was quite narrow. Over Kansas, the width of the stratiform region was similar to that of the convective region. By 2230 UTC (Fig. 5.11b), both of the rainfall rate bands over Kansas and Oklahoma weakened, with maximum values of about 30 and 20 mm h^{-1} , respectively, while the circular rainfall rate maximum shown at the previous time evolved into a band structure and merged with the one over Kansas. With

(a)

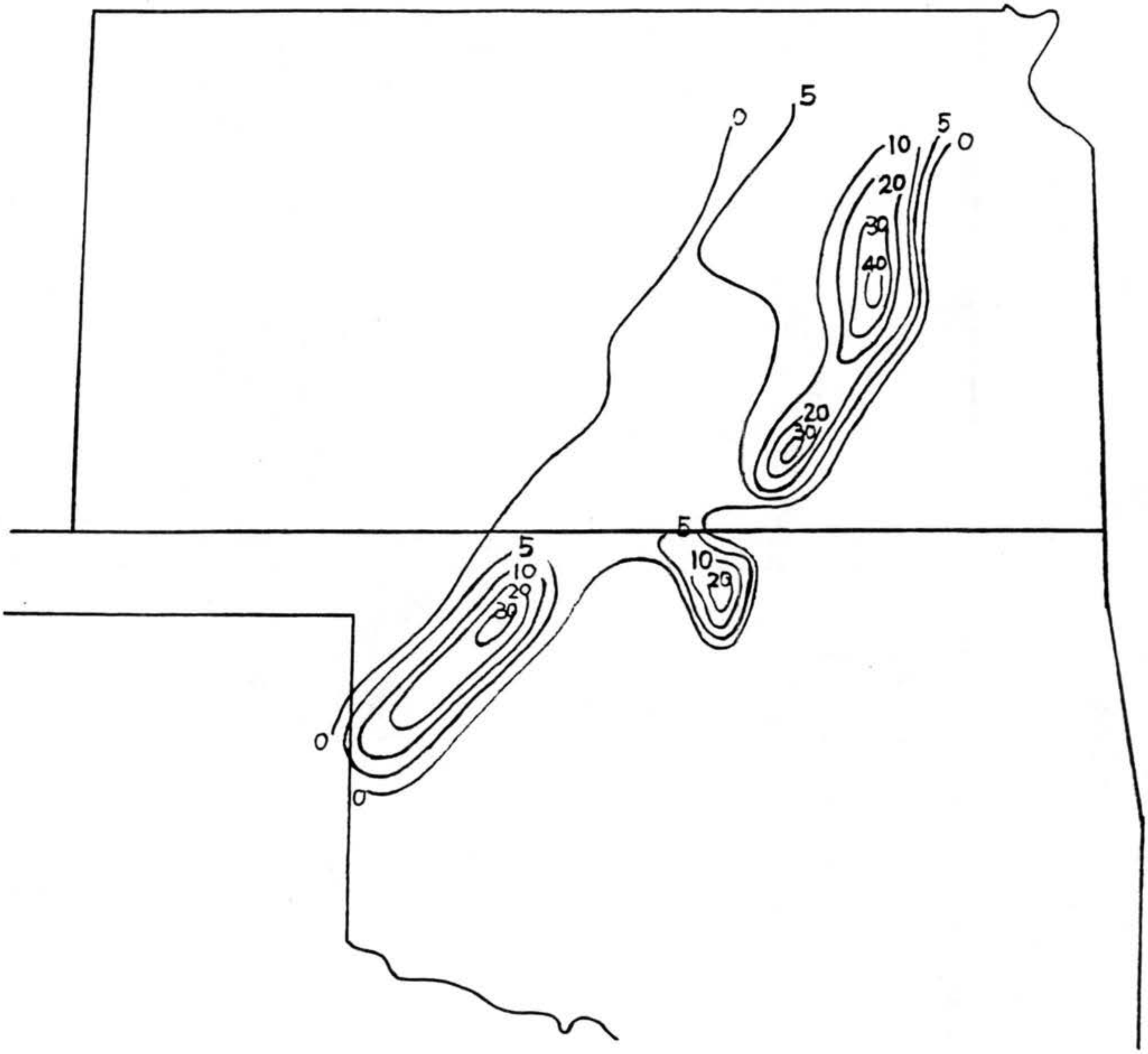

Figure 5.11: Observed rainfall rates (in mm h^{-1}) for the PRE-STORM region using PAM and SAM mesonet data at a) 2100 UTC, b) 2230 UTC, c) 0000 UTC, d) 0130 UTC, e) 0300 UTC, f) 0430 UTC.

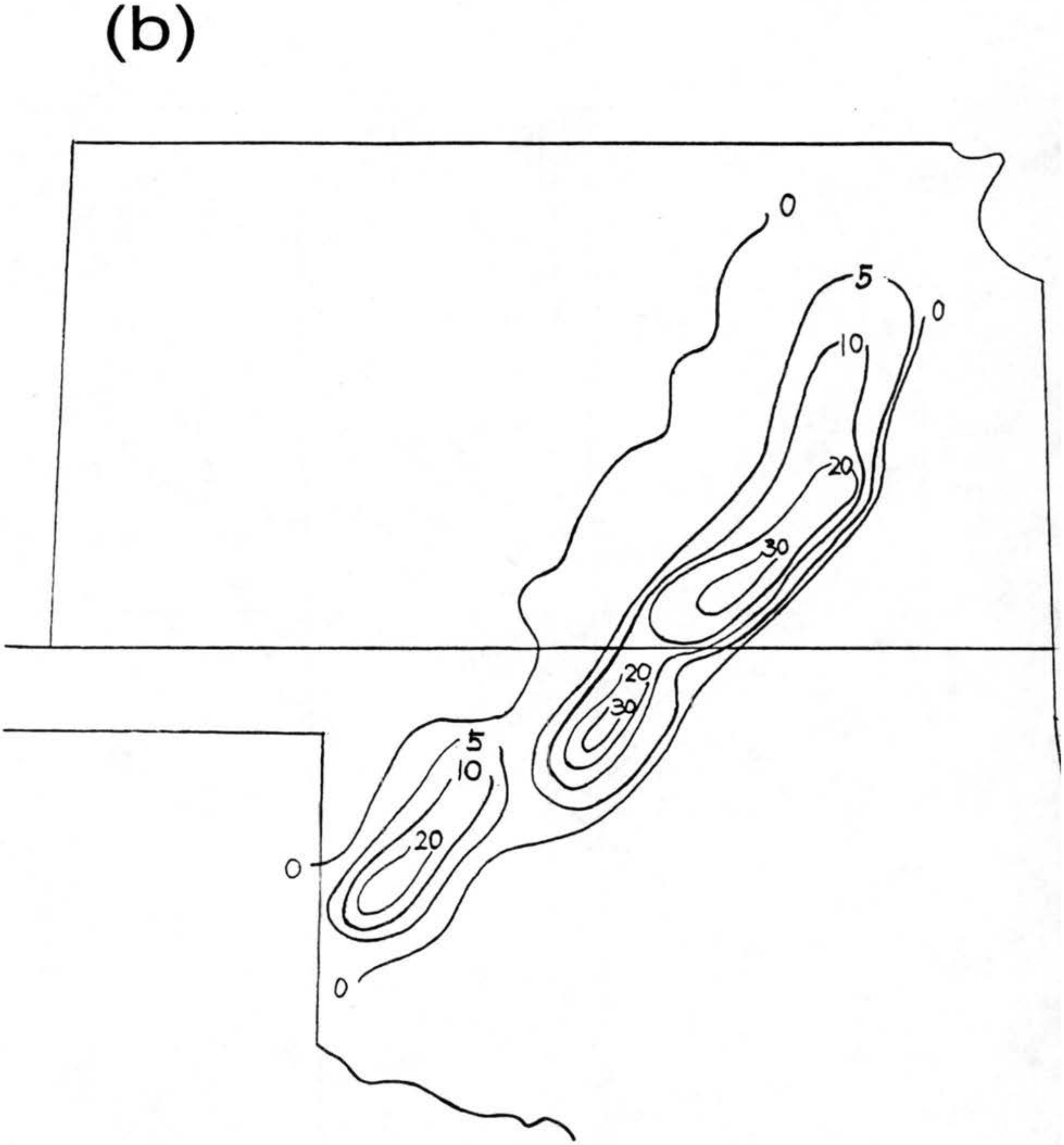

Figure 5.11: Continued.

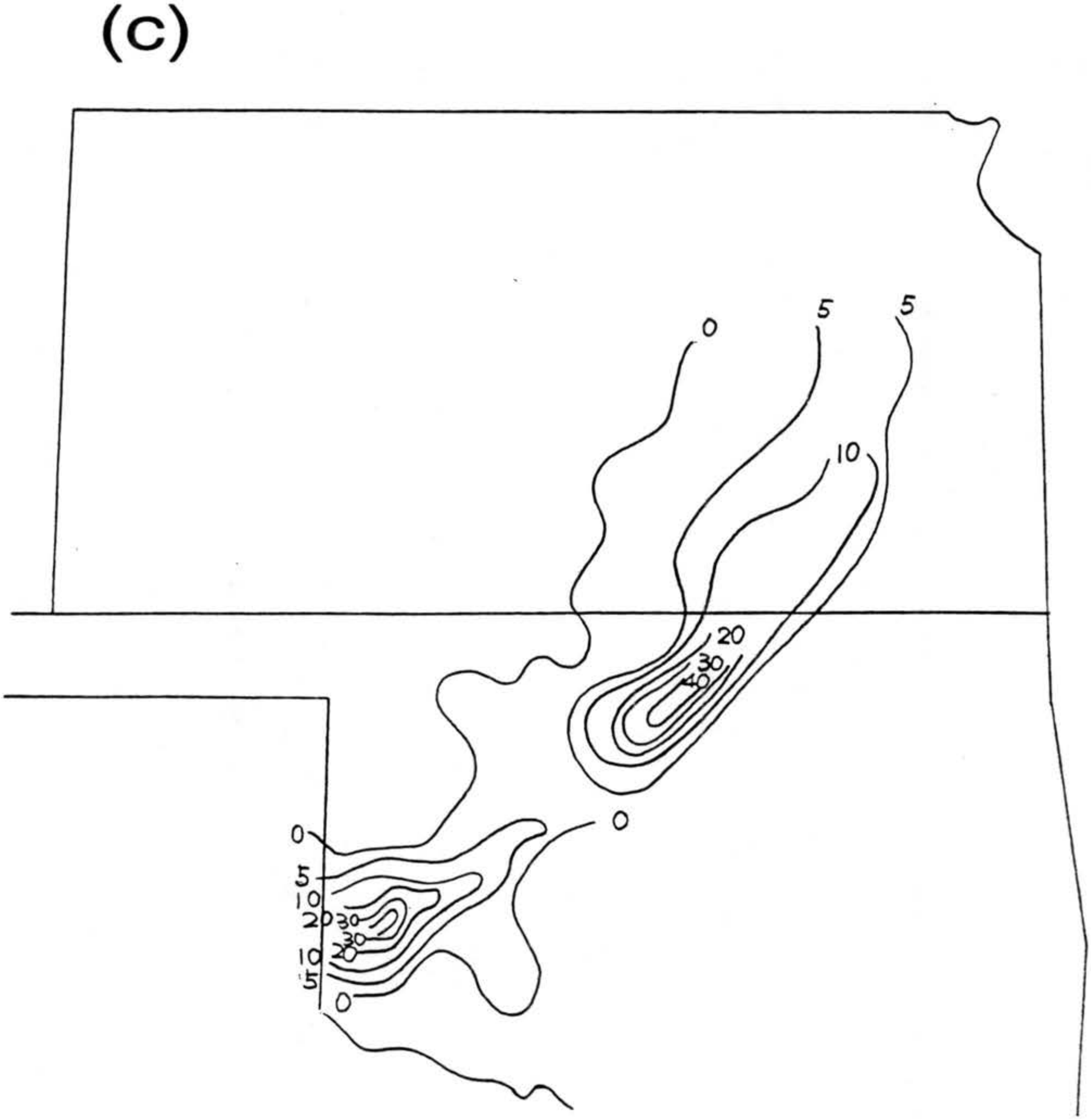

Figure 5.11: Continued.

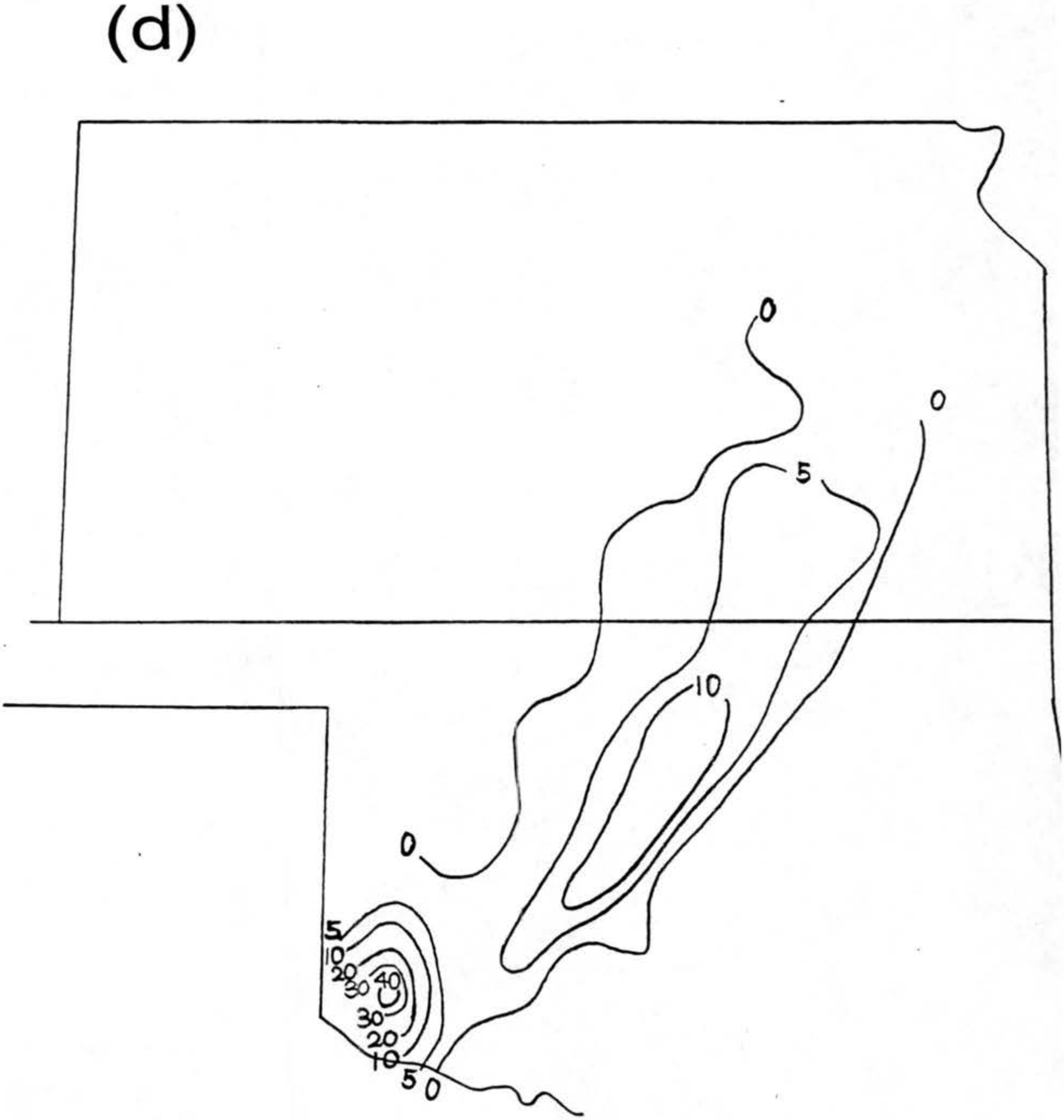

Figure 5.11: Continued.

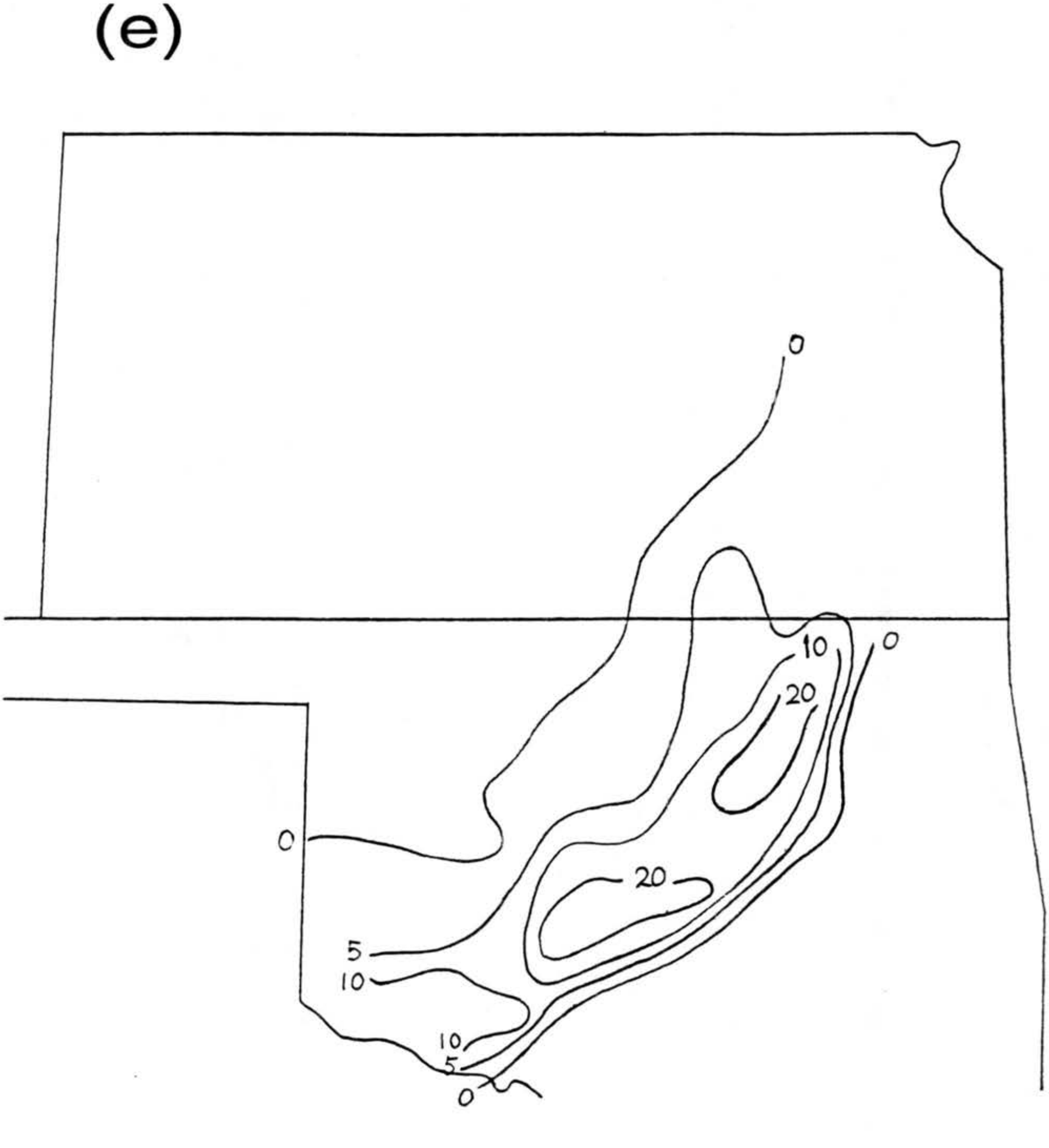

Figure 5.11: Continued.

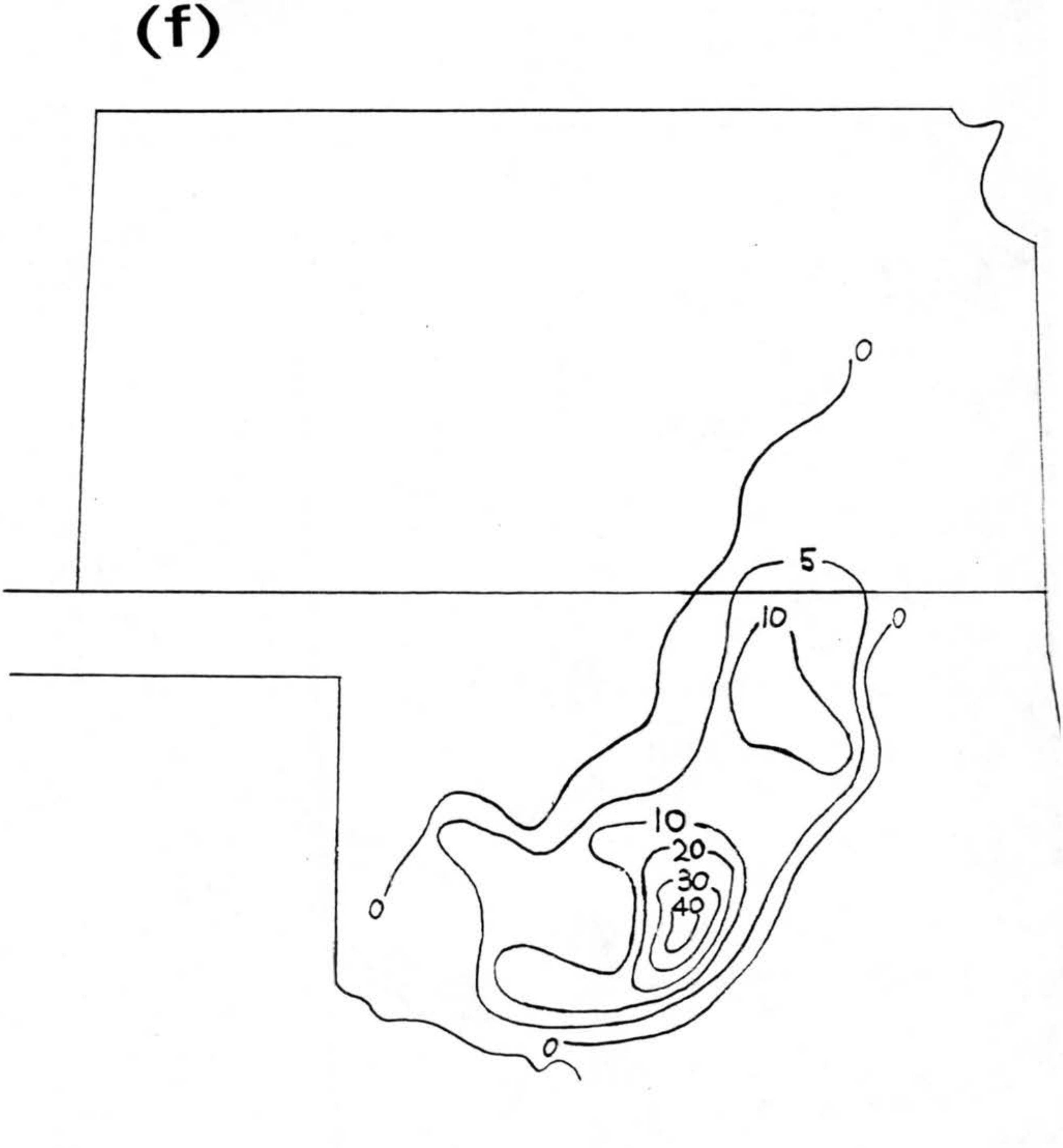

Figure 5.11: Continued.

the peak rainfall rates over Kansas further decreasing at 0000 and 0130 UTC (Figs. 5.11c and d), the precipitation bands changed from three to two and were generally located in the Oklahoma region with the larger band at the southwest end of the squall line. The stratiform region developed to the rear of the convective region and had almost the same width as the convective region in Oklahoma at these two times. When the system evolved into the dissipating stage at 0300 and 0430 UTC (Figs. 5.11e and f), it turned out that the rainfall rates increased again, indicative of the large variability of the system evolution. On the other hand, the increase could also be an artifact of the coarse resolution of the surface mesonet, such that some intense rainfall values at 0130 UTC were not resolved. During the dissipating stage, the entire width of the squall line increased and the rainfall rate pattern became relatively symmetric. However, the stratiform region still had a similar width to the convective region.

Similar to the works by Chen and Zipser (1982), Kuo and Anthes (1984) and Gallus and Johnson (1991), comparisons of diagnosed and observed rainfall rates were performed for six budget times. Figures 5.12 and 5.13 illustrate the precipitation rates predicted from the heat and moisture budgets, respectively.

At 2100 UTC (Figs. 5.12a and 5.13a), consistent with the two large rainfall rate bands in the observed data, the diagnosed rainfall rates exhibited two peaks similarly-located over Oklahoma and Kansas, respectively. Since cumulus-scale features can not be fully resolved by the sounding data, the predicted rainfall rates were largely underestimated and the peak values were only about 30 % to 40 % of the observed, agreeing with the results of Gallus and Johnson (1991). Ahead of the squall line, negative values can be noticed along the leading edge, which indicated pre-squall evaporation. The leading edge was well defined by the predicted rainfall rates compared to radar echo and observed rainfall rates.

At 2230 UTC (Figs. 5.12b and 5.13b), the rainfall rates calculated from the heat and moisture budgets compared well with each other in terms of magnitudes and positions. There were still two peak values over Oklahoma and Kansas with maximum magnitudes about 30 % of the observed. Evaporation can be noticed to the rear of the system.

Rather strong evaporation persisted over the northeast corner of Kansas from 2100 to 0130 UTC. Although some of it may not be real since it was near the edge of network,

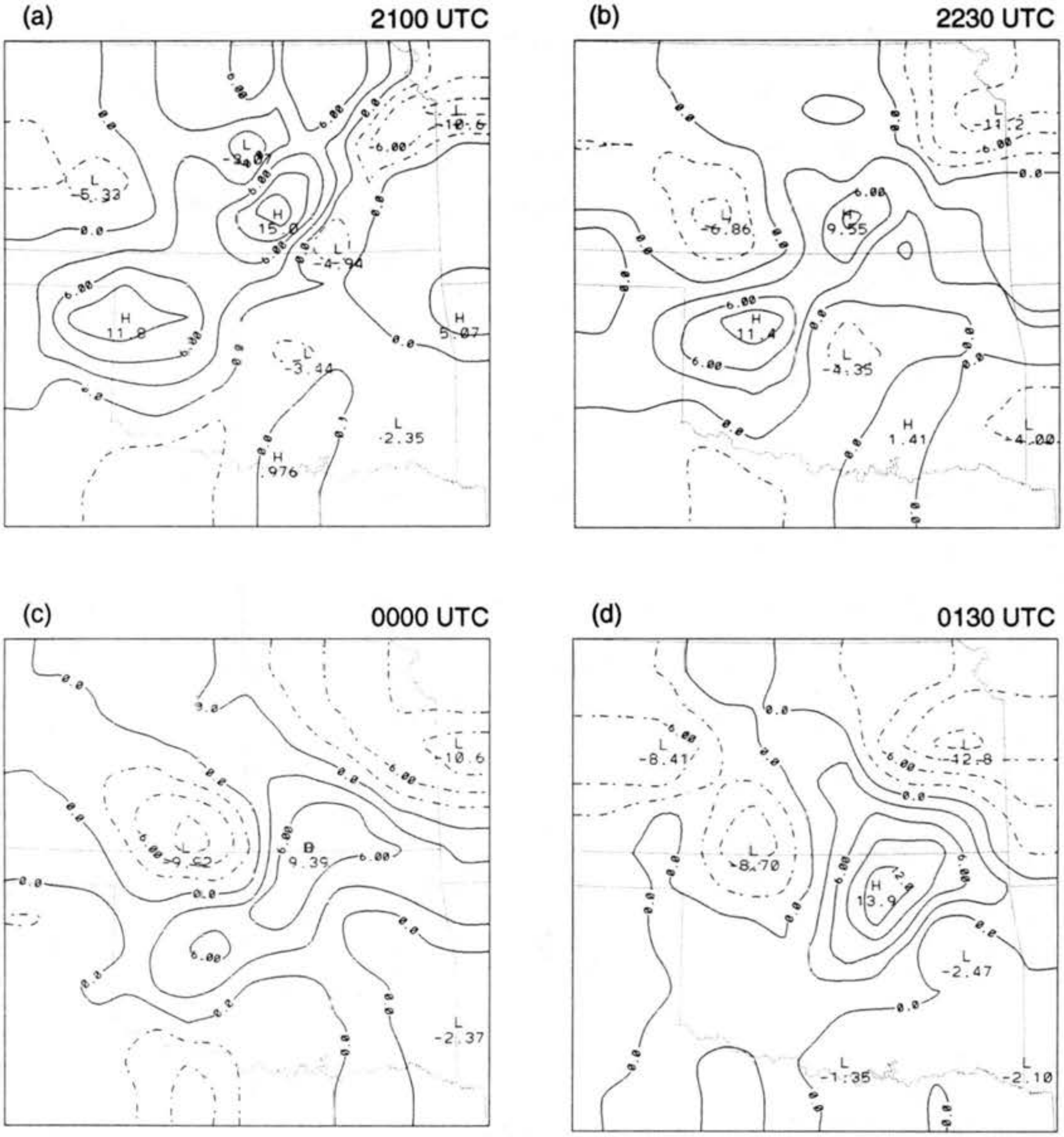

Figure 5.12: Predicted rainfall rates (in mm h^{-1}) from the vertically integrated heat budget at a) 2100 UTC, b) 2230 UTC, c) 0000 UTC, d) 0130 UTC, e) 0300 UTC, f) 0430 UTC.

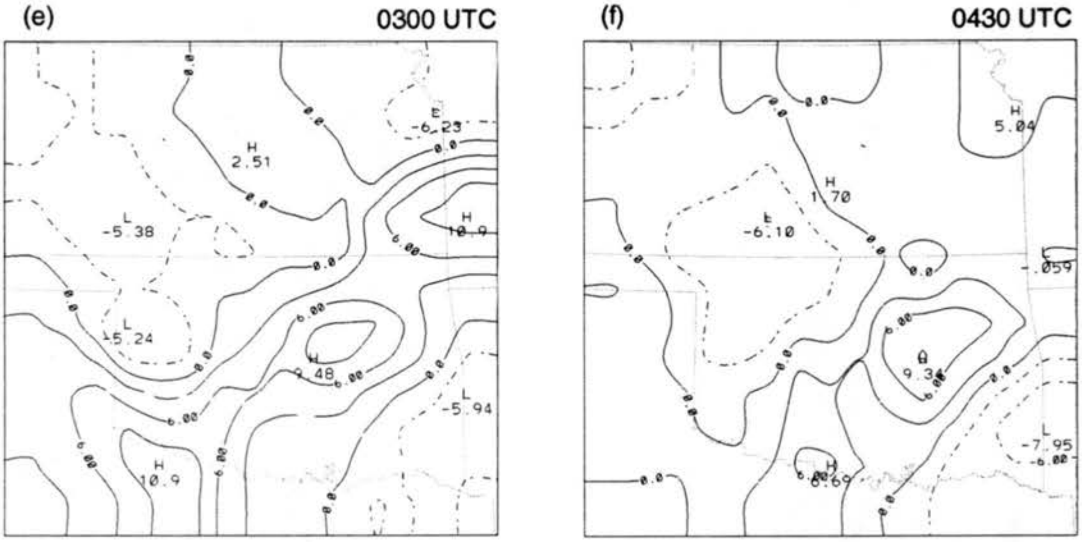

Figure 5.12: Continued.

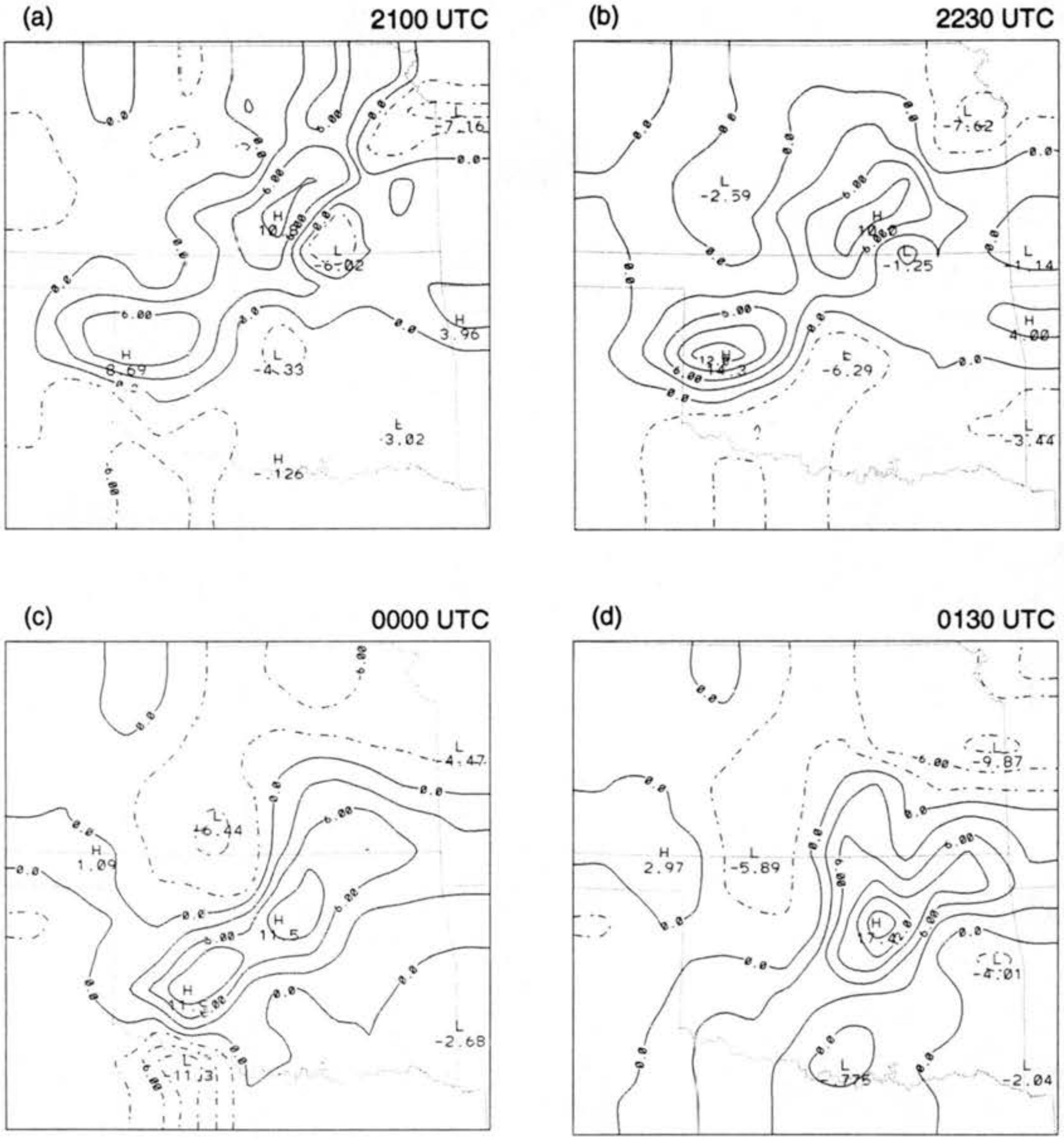

Figure 5.13: As in Fig. 5.12, except for the vertically integrated moisture budget.

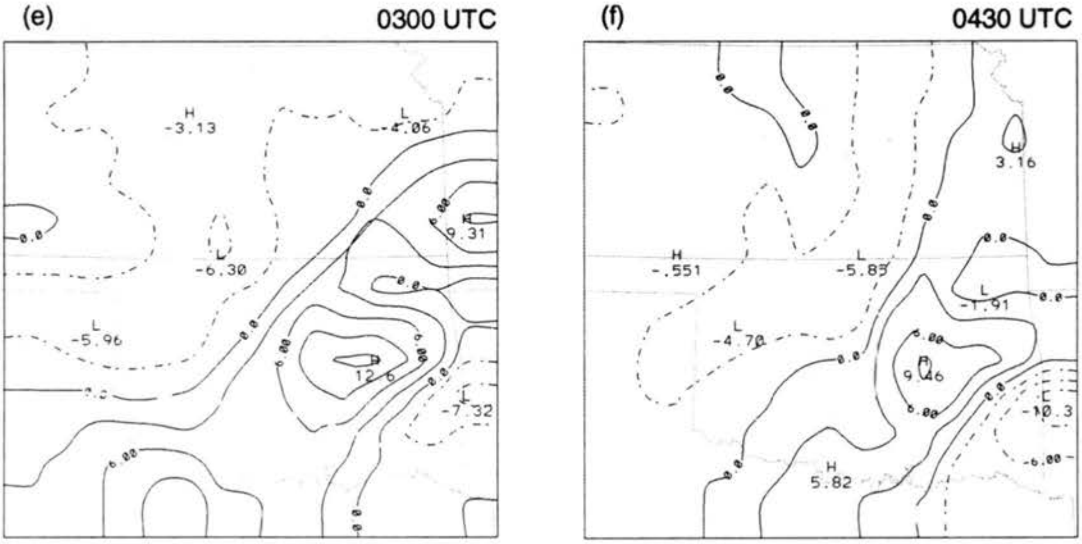

Figure 5.13: Continued.

part of it may account for the continuing dissipation of the squall line over Kansas. The main part of the system moved into Oklahoma after 0000 UTC. At 0130 UTC (Figs. 5.12d and 5.13d), the heat and moisture budgets diagnosed very similar peak rainfall rates to the observed (although as noted, the observed may have been underestimated).

As the system evolved into the late mature and dissipating stages at 0300 and 0430 UTC (Figs. 5.12e and f and 5.13e and f), "negative precipitation" or an excess of evaporation over condensation can be clearly seen behind the system. The peak rainfall rates estimated from Q_1 and Q_2 reached 50 % of those observed. However, they were displaced forward compared to the radar echo (Figs. 4.2f and g). One possible reason for this forward displacement is that the leading edge of the system was near the edge of sounding network, so features from within the system were smoothed forward during the objective analysis.

Table 5.1 compares the rainfall rates diagnosed from the heat and moisture budgets to those observed in the convective region from 2100 to 0300 UTC. Since the convective system remained narrow and there was no clear separation between the convective and stratiform regions, together with that the system was not well organized, large variation may occur. From the developing and mature to the dissipating stages, the observed rainfall rates increased from 9.0 mm h^{-1} at 2100 UTC to 10.7 mm h^{-1} at 2230 UTC and reached a maximum (10.9 mm h^{-1}) at the mature stage (0000 UTC), then decreased to 9.4 mm h^{-1} at 0130 UTC. At 0300 UTC, however, the rainfall rate increased again (10.3 mm h^{-1}). Although some errors may exist in the accumulated rainfall data and during the process of calculating the averaged rainfall rates, the observed rainfall rates generally remained between 9.5 and 11.0 mm h^{-1} . This indicates that the variation of the average intensity of the convective system was not large throughout the entire study period, differing from the 10-11 June case which showed an apparent decrease during the dissipating stage.

The predicted rainfall rates from integration of Q_1 and Q_2 underestimated the observed rates by 20 % to 40 % in the convective line. This percentage in the convective region is a little better than that found in the 10-11 June case. In the 10-11 June case, the dominant features of the stratiform region might be aliased into the convective region.

Time	$\int Q_1$ dp (mm h^{-1})	$\int Q_2$ dp (mm h^{-1})	Observed (mm h^{-1})
2100 Z	7.6	6.3	9.0
2230 Z	7.3	8.3	10.7
0000 Z	5.9	6.6	10.9
0130 Z	6.7	5.3	9.4
0300 Z	6.5	6.8	10.3

Table 5.1: Comparison of rainfall rate predictions (in mm h^{-1}) from the integrated heat and moisture budgets with observed rainfall rates over the convective region from 2100 to 0300 UTC.

Time	$\int Q_1$ dp (mm h^{-1})	$\int Q_2$ dp (mm h^{-1})	Observed (mm h^{-1})
2230 Z	2.2	3.6	3.6
0000 Z	2.3	0.8	3.6
0130 Z	2.8	2.3	3.6
0300 Z	3.5	2.3	3.4
0430 Z	2.7	1.0	4.7

Table 5.2: Comparison of rainfall rate predictions (in mm h^{-1}) from the integrated heat and moisture budgets with observed rainfall rates over the stratiform region from 2230 to 0430 UTC.

Time	$\int Q_1$ dp (mm h^{-1})	$\int Q_2$ dp (mm h^{-1})	Observed (mm h^{-1})
2100 Z	6.3	5.1	6.6
2230 Z	5.4	6.7	7.6
0000 Z	5.3	5.1	6.9
0130 Z	5.5	4.2	5.9
0300 Z	4.7	4.0	6.5

Table 5.3: as Table 5.1 except for the entire system.

The underestimation is mainly due to inadequate resolution of the convective line by the sounding network.

Comparison of the rainfall rates in the stratiform region from 2230 to 0430 UTC is presented in Table 5.2. The observed rainfall rates from 2230 to 0300 UTC are generally around 3.5 mm h^{-1} , which are similar to those found in the 10-11 June case. At 0430 UTC, the rainfall rate reached 4.7 mm h^{-1} .

From 2230 to 0300 UTC, the rainfall rates predicted by integration of Q_1 in the stratiform region turned out to be quite stable and were generally $0.5 \sim 1.0$ mm h^{-1} smaller than those observed. However, the rainfall rates diagnosed by integration of Q_2 had relatively large variations. At 0430 UTC, both predicted rainfall rates underestimated the observed rate by 2 to 3 mm h^{-1} . One explanation for this discrepancy between the predicted and observed rainfall rates is the rearward transport of hydrometeors (Rutledge and Houze 1987; Gallus and Johnson 1991) and storage effect (McNab and Betts 1978; McAnelly and Cotton 1990). However, since the stratiform region remained narrow in the 26-27 June case throughout the system evolution, the resolution problem and errors should have more effect on the rainfall rate prediction. Caution must be taken when considering the stratiform region.

In order to minimize the problems of inadequate sounding resolution and occasionally extremely large rainfall rate values at a single grid point, the rainfall rates averaged over the entire system were compared from 2100 to 0300 UTC (Table 5.3). As the system evolved, the observed rainfall rates increased from 6.6 mm h^{-1} at 2100 UTC and reached the maximum 7.6 mm h^{-1} at 2230 UTC, then began to decrease to 6.9 mm h^{-1} at 0000 UTC and 5.9 mm h^{-1} at 0130 UTC. At 0300 UTC, the observed rainfall rate increased again (6.5 mm h^{-1}). The diagnosed rainfall rates are generally 1 to 2 mm h^{-1} smaller than the observed rates. Both the observed and predicted rainfall rates are relatively stable although there are some fluctuations. This indicates that although the stratiform region gradually developed to the rear of convective line, the production of rain by the entire convective system remained relatively constant.

In general, although there was underestimation due to resolution, the predicted values from Q_1 and Q_2 agreed fairly well with the radar echoes and the observed rainfall rates in terms of position and magnitudes. It may be improved if the sounding and surface stations had similar resolution. The rainfall rate predicted from the heat budget is generally 0.5 $\sim$ 1.0 mm h^{-1} better than that from the moisture budget in this case especially for the entire system, supporting the results of Gallus and Johnson (1991) for the 10-11 June case showing that Q_1 was a better predictor of rainfall rate.

As illustrated in Eq. (2.5), the discrepancy between the actual precipitation rate and the diagnosed precipitation rate is basically determined by the temporal and spatial variation of P_x, the combination of volume integrations of net ice phase changes, convergence terms of horizontal eddy flux and surface terms, which can not be determined directly from conventional sounding data; and P_σ the errors resulting from data grid selection, smoothing scheme, distribution of sounding stations, storage effect and hydrometer transport by system relative flow. In the convective region, it appeared that the resolution problem mainly resulted in the discrepancy. However, in the stratiform region, it becomes much more complicated. For an extensive stratiform region, such as the 10-11 June PRE-STORM case, the resolution problem is not so large (Gallus and Johnson 1991). The discrepancy can be basically explained by the storage effect and hydrometer transport from the convective region. For a narrow stratiform region, such as the early stages of the 26-27 June case, the resolution problem can act as an equally important factor in affecting the discrepancy.

Chapter 6

MOMENTUM BUDGET

As discussed in previous chapters, the 26-27 June squall line was characterized by asymmetry along the line during the early times and a slow moving speed. The width of the stratiform region underwent a relatively large change throughout the budget analysis times. Although it was still quite narrow compared to some other typical squall line cases, its width gradually increased from $\sim 30 - 50$ km at the developing and mature stages to more than 100 km at the dissipating stage. In this chapter, we document the evolution of the Coriolis force, pressure gradient force, acceleration and turbulent terms normal to the squall line. The results during the mature and dissipating stages will be compared with the 10-11 June squall line budget study (Gallus and Johnson 1992).

Few previous studies have directly applied mesoscale rawinsonde height data to perform momentum budgets. Part of the difficulty came from the fact that the actual height variation usually had the same order as the data errors (Fankhauser 1974). With the eventual improvement of measuring instruments and techniques, the height data has been tested and found to be good enough to yield reasonable budget results (Sanders and Emanuel 1977). In this chapter, therefore, the pressure gradient force will be calculated directly from height data.

6.1 Geopotential height

From 2100 to 0430 UTC, the 26-27 June squall line evolved from the developing and mature to the dissipating stages. The width of the convective region gradually decreased from $\sim 50 - 60$ km to $\sim 30 - 40$ km, while the width of the stratiform region increased from ~ 30 − 50 km to more than 100 km. The geopotential height field, affected by this mesoscale convective system, also exhibits a quite interesting evolution pattern.

Figure 6.1 shows the geopotential height at 700 hPa for six budget times. At 2100 UTC (Fig. 6.1a), a pronounced synoptic-scale trough was over northern Kansas. The squall line was located in front of the trough where the geopotential height gradient was large. A distinct mesolow, as found in many squall line cases (Sanders and Emanuel 1977; Brown 1979; Menard and Fritsch 1989; Stumpf 1989; Gallus and Johnson 1992), did not appear at this time. Ahead of the squall line, the geopotential height gradually increased.

By 2230 and 0000 UTC (Figs. 6.1b and c), although the squall line remained relatively narrow, the geopotential height field indicated that a weak trough began to develop over the MCS (see 3150 m contour), suggesting an effect of the squall line on the geopotential height field. However, it is hard to distinguish whether the small trough was induced by the convective region or the stratiform region. A synoptic low was present to the rear of the system over northern Kansas.

At the mature and dissipating stages (0130 to 0430 UTC) (Figs. 6.1d, e and f), the squall line moved to the eastern Kansas and central and western Oklahoma and gradually widened. A deep mesoscale trough gradually developed at 700 hPa within the MCS. It had a width similar to the squall line and its position coincided well with the low-level radar echo resulting from the squall line system, especially at 0430 UTC. At 0300 UTC, a closed mesolow can be clearly seen over the Kansas-Oklahoma border. A mesoscale high was present to the rear of the squall line at 0300 and 0430 UTC.

Figure 6.2 shows the geopotential height evolution at 500 hPa for six different times. At 2100 UTC (Fig. 6.2a), a strong geopotential height gradient was occurring in front of the synoptic trough. The orientation of the squall line was almost parallel to the height contours. By 2230 to 0130 UTC (Figs. 6.2b, c and d), the geopotential height patterns were generally quite similar to those at 700 hPa with small variations. A synoptic-scale trough was located to the north of Kansas. Near the squall line, the height variation associated with the convective system was not pronounced.

By 0300 and 0430 UTC (Figs. 6.2e and f), there was a very prominent narrow mesoscale trough extending from eastern Kansas to southwest of Oklahoma. The trough

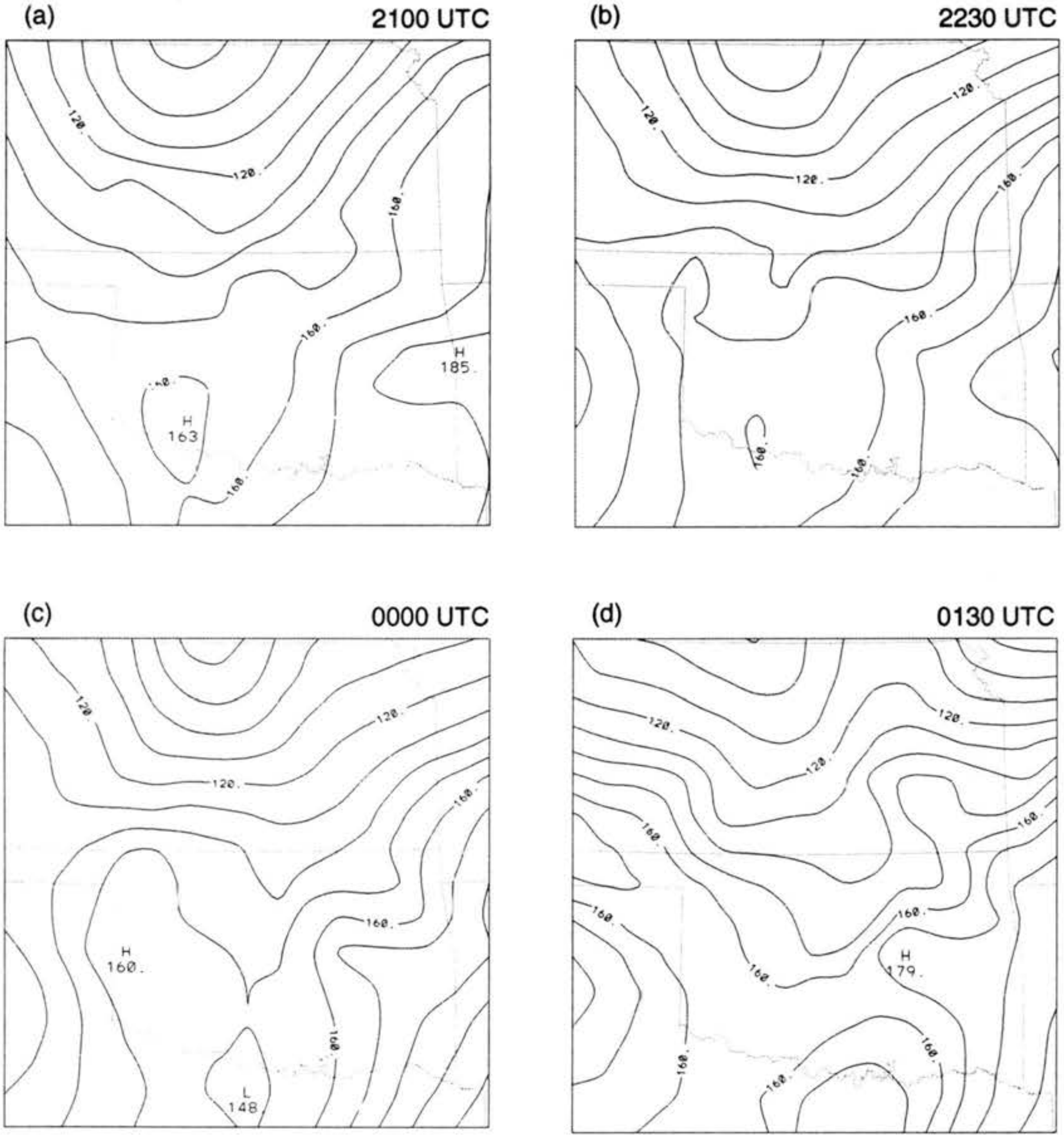

Figure 6.1: Geopotential height at 700 hPa in the PRE-STORM region for a) 2100 UTC, b. 2230 UTC, c) 0000 UTC, d) 0130 UTC, e) 0300 UTC, f) 0430 UTC. Heights are expressed in meters above 3000 m.

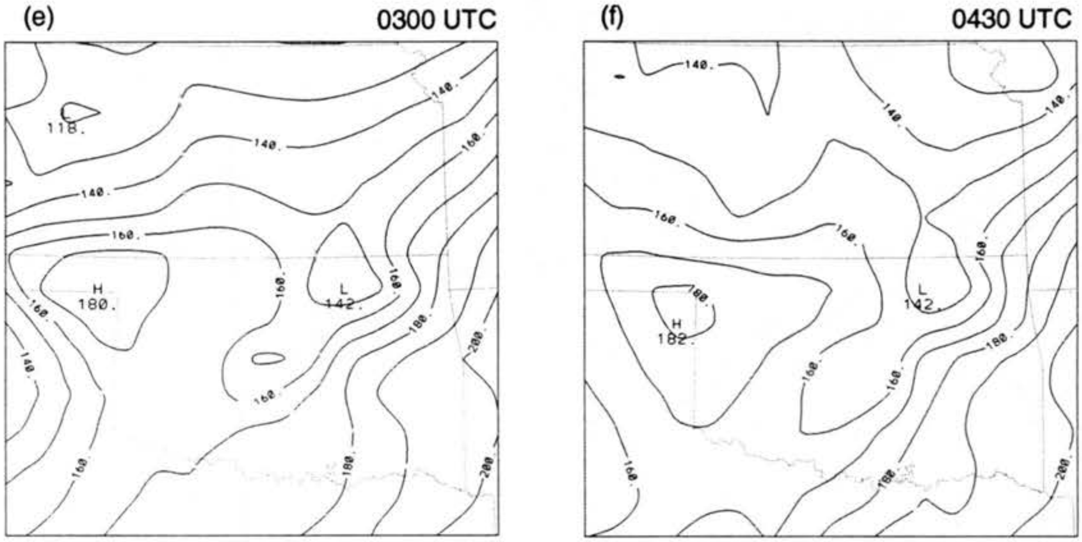

Figure 6.1: Continued.

line was roughly located within the stratiform region. Behind the mesolow region there was a mesohigh region, similar to that at 700 hPa. The height gradient across the squall line was about 30 – 40 m at 700 hPa and 25 m at 500 hpa over a distance of ~ 150 – 200 km, much less than that found in the 10-11 June case (70 m at 700 hPa) (Gallus and Johnson 1992).

By studying a GATE cumulonimbus line using aircraft data, LeMone (1983) found that there was a hydrostatically-induced mesolow within the convective region of the squall line. Smull and Houze (1987) also noticed a mesolow in a study of a middle latitude squall line. As depicted in the squall line schematic from Houze et al. (1989), this convective mesolow is located around midlevels in the convective region. In the 26-27 June case, the convective region was the widest and the convection was most intense between 2100 and 0000 UTC. However, no pronounced mesolow was found in the geopotential height field at middle and low levels during the early times (except a weak mesoscale trough), implying that the mesolow within the convective region was too small to be resolved by PRE-STORM sounding network, if it existed at all. Therefore, the deep mesoscale trough that appeared at the dissipating stage when the convective activity weakened could not be produced by the convective region. Since this mesoscale trough coincided well with the expanding stratiform region, it should be the feature produced by the stratiform region.

The mesolow within the stratiform region has been observed in many tropical and midlatitude squall line studies. Houze et al. (1989) showed that the maximum intensity of the mesolow is located at middle levels near the melting level. It is believed that this mesolow is also hydrostatically-induced (Brown 1979) and generated in the stratiform region by the latent heat release aloft within the anvil cloud and evaporational cooling and melting (Leary and Houze 1979) below cloud base.

Figure 6.3 shows the vertical cross-sections of perturbation height for six budget times. The method is similar to that used by Gallus and Johnson (1992). Since height data in the undisturbed environment outside the system were not available, the perturbation heights were computed by subtracting latitudinal averages across the selected domain at each level.

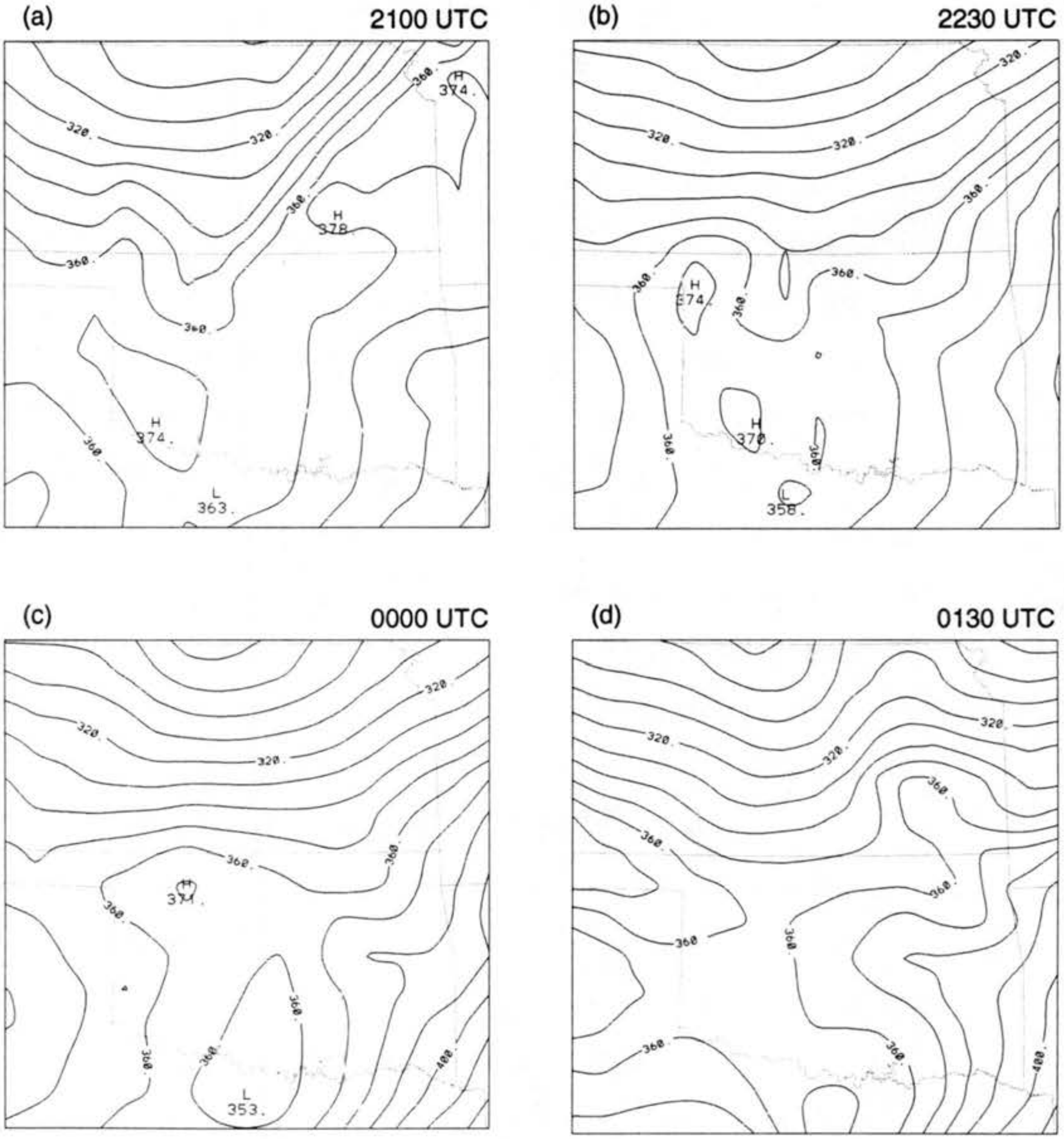

Figure 6.2: As in Fig. 6.1, except for 500 hPa. Heights are in meters above 5500 m.

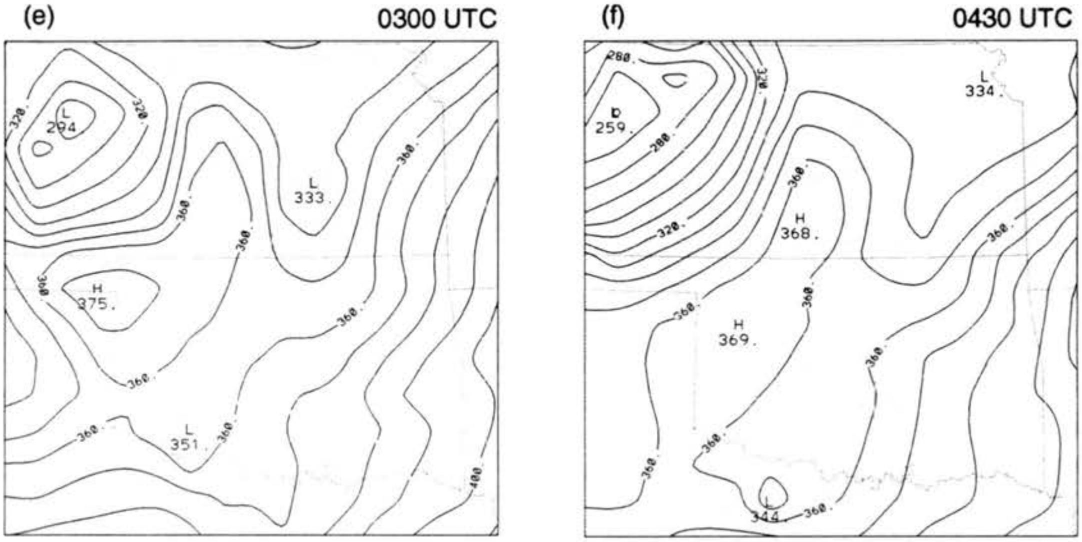

Figure 6.2: Continued.

During the developing and mature stages (from 2100 to 0000 UTC) (Figs. 6.3a, b and c), the most prominent feature is the positive height perturbation ahead of the squall line system and negative height perturbation behind the leading edge. The largest negative height perturbation was located at about 350 hPa, 300 km behind the leading edge. It was associated with a synoptic scale trough. Another notable feature is a positive height perturbation present at upper levels above the squall line. It was also observed in the 10-11 June budget study by Gallus and Johnson (1992) and noticed by Gao et al. (1990) in a numerical simulation. It is likely produced by both the cumulus updrafts in the convective region and mesoscale updrafts in the stratiform region.

A mesolow can be noticed at middle levels during the early times (2100 to 2230 UTC) (Figs. 6.3a and b). It was located at 700 hPa 250 km behind the leading edge at 2100 UTC and 550 hPa 80 km behind the system at 2230 UTC. However, the association of this mesolow with the squall line is questionable since the geopotential height field only indicated a weak trough over the squall line during the early stages and there was a synoptic low located north of Kansas just behind the squall line, which might account for this feature. Therefore, we will only concentrate on studying the mesolow at later times.

In studies of the 3-4 June PRE-STORM MCS (Smull and Augustine 1989) and the 10-11 June squall line (Gallus and Johnson 1992), the maximum amplitude of the low was observed to be around the melting level. In the 26-27 June case at the mature and dissipating stages (0000 to 0430 UTC) (Figures 6.3c, d, e and f), as the width of the stratiform region gradually increased, the mesolow was very well illustrated within the system. It extended vertically from low levels to about 400 hPa with a peak also located around the melting level (600 hPa), supporting previous observations. The midlevel mesolow gradually deepened from -8.4 m at 0000 UTC to -14.1 m and -18.7 m at 0130 and 0300 UTC, and reached the maximum (-20.9 m) at 0430 UTC. The peak was generally located at about 50 − 80 km behind the leading edge. Similar to the Q_1 and Q_2 fields in Chapter 5, the tilting of the mesolow was also quite small. During the developing and early mature stages, it turned out that there was no positive height perturbation present to the rear of the system. During the late mature and decaying stages, a positive height perturbation

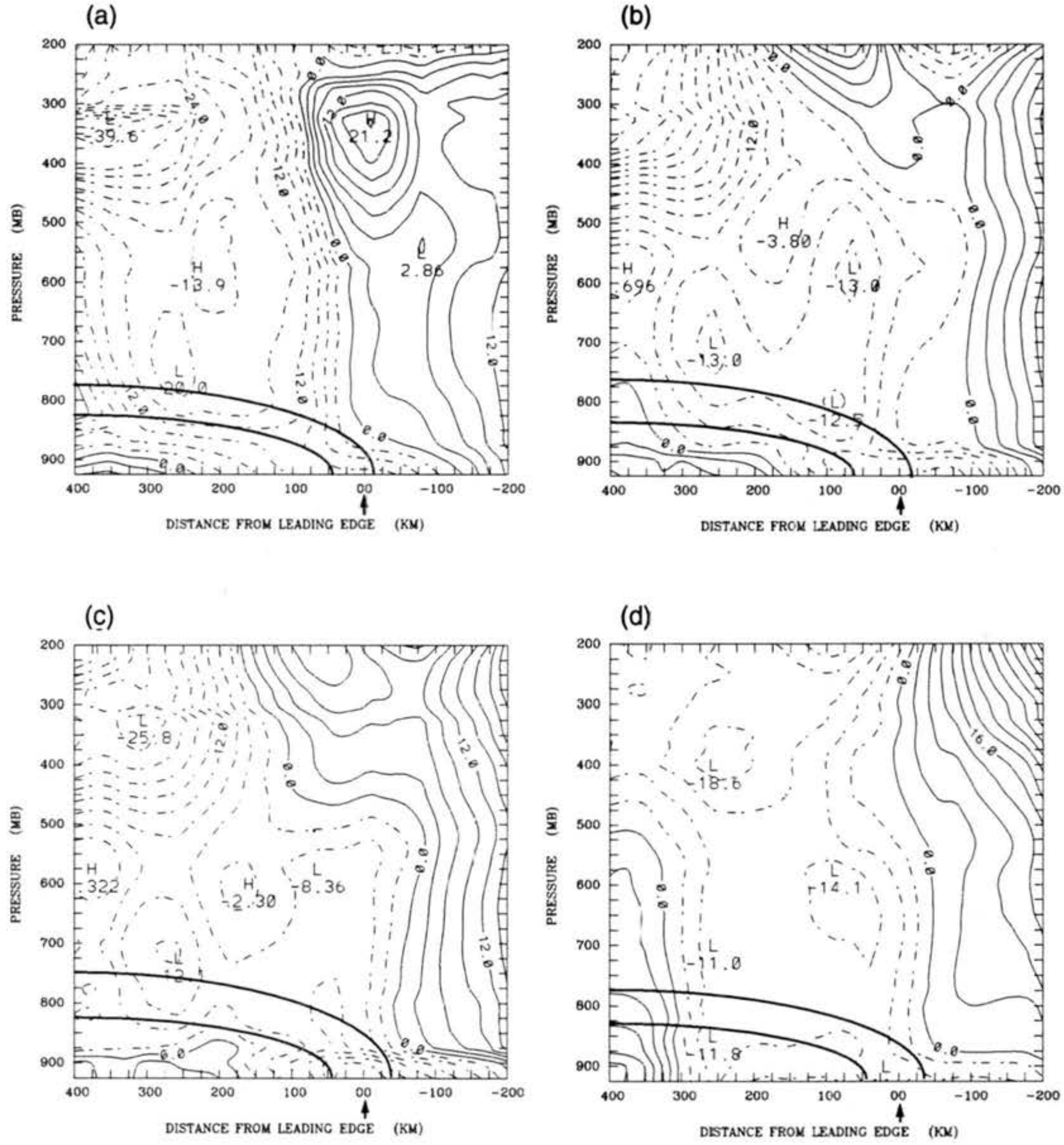

Figure 6.3: Vertical cross-sections of height perturbation (in meters) from latitudinal-average within PRE-STORM region for a) 2100 UTC, b) 2230 UTC, c) 0000 UTC, d) 0130 UTC, e) 0300 UTC, f) 0430 UTC.

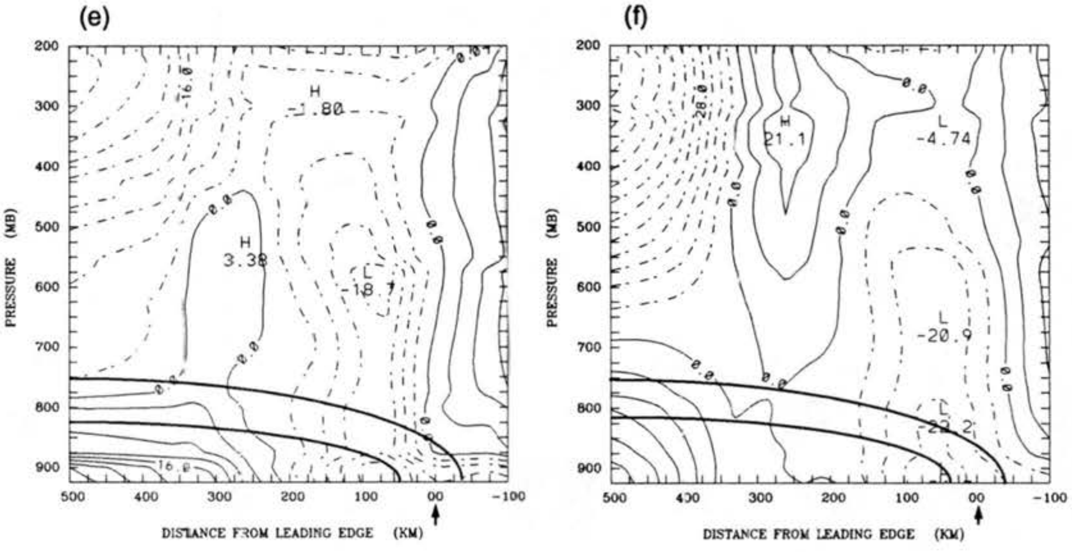

Figure 6.3: Continued.

gradually developed at about 200 km behind the mesoscale trough, which helped to induce rear-to-front flow into the system during the decaying stage (refer to Figs. 4.3e and f).

6.2 Force balance

As shown in the previous section, during the early stage, the effects of the squall line (the midlevel mesolow) on the momentum budget components (especially for the pressure gradient acceleration) might not be well resolved since the squall line was still quite narrow. Therefore, for the vertical cross-sections normal to the squall line, we only concentrate on studying the acceleration evolution patterns during the mature to the dissipating stages (0000 to 0430 UTC) and compare them with the results of the 10-11 June case (Gallus and Johnson 1992).

Figure 6.4 shows the vertical cross-sections of the pressure gradient force normal to the squall line from 0000 to 0430 UTC. At 0000 and 0130 UTC (Figs. 6.4a and b), front-to-rear acceleration took place over most of the regions. The figures at earlier times (not shown here) also indicated similar features. As stated before, the 26-27 June squall line was at the developing and mature stages at these times. The feature of dominance of the front-to-rear acceleration might have partly resulted from the fact that the 26-27 June squall line remained quite narrow at these times and its effects on the geopotential height might not be sufficiently resolved. On the other hand, this feature also indicated that the rear-to-front acceleration induced by the pressure gradient force might not be generated during the developing and early mature stages when the stratiform region was narrow and the midlevel mesolow was not apparently developed. However, some mesoscale features can still be observed at 0000 and 0130 UTC. Just ahead of the leading edge, there was moderately large front-to-rear acceleration. About 300 km behind the leading edge, rear-to-front acceleration took place at low and middle levels. However, this distant rear-to-front acceleration might not be induced by the squall line system, rather it was probably due to the surface anticyclone.

At the late mature and dissipating stages (0300 to 0430 UTC) (Figs. 6.4c and d), the pressure gradient acceleration showed different features from those at early times. There

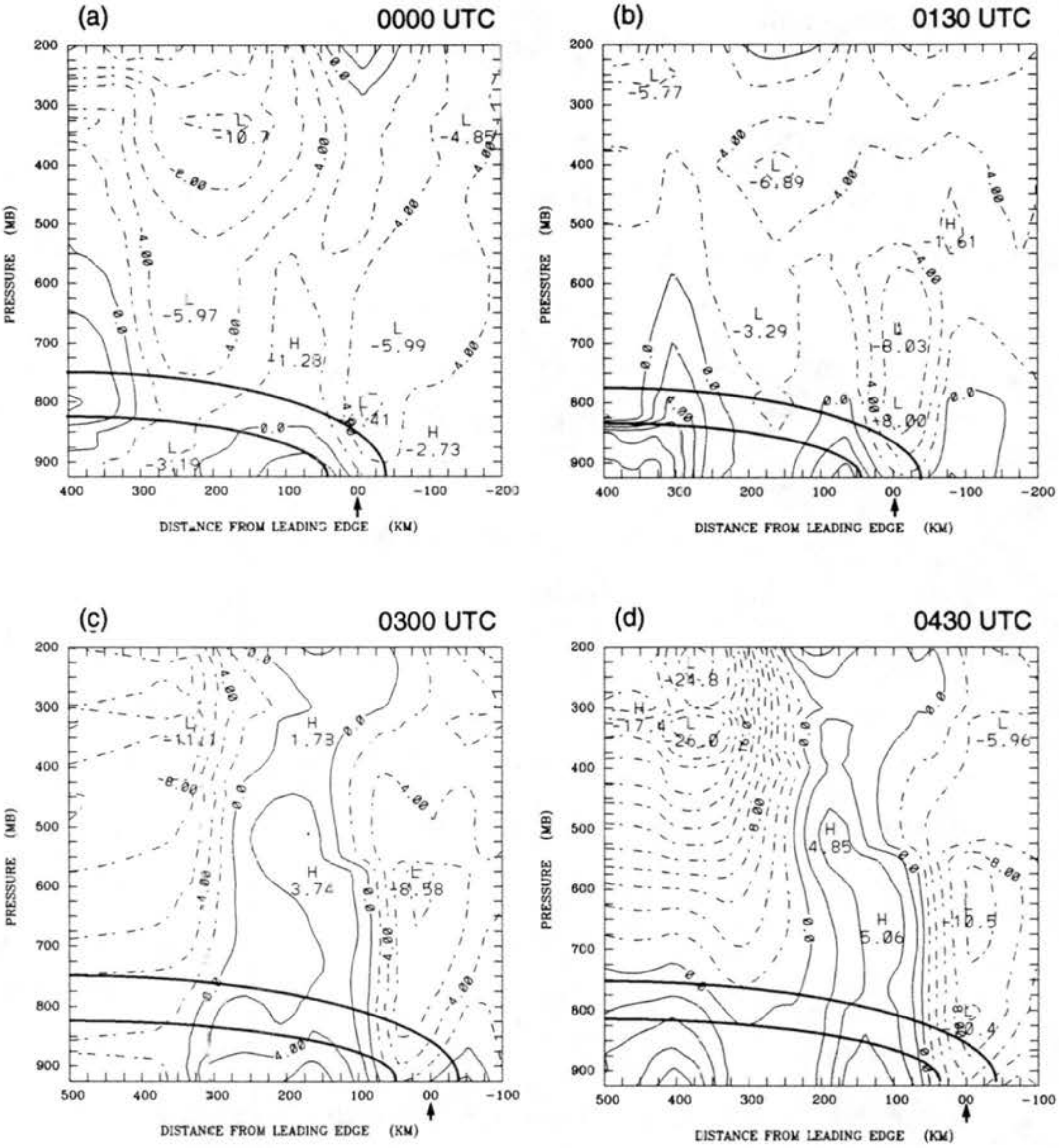

Figure 6.4: Vertical cross-sections of component of pressure gradient acceleration normal to the squall line (in unit of m s^{-1} h^{-1}) at a) 0000 UTC, b) 0130 UTC, c) 0300 UTC, d) 0430 UTC. Positive values indicate acceleration from rear to front (left to right).

developed a prominent rear-to-front pressure gradient acceleration aloft from 50 km to $\sim$ $200 - 300$ km behind the leading edge. The peak acceleration gradually increased from 3.7 m s^{-1} h^{-1} at 0300 UTC around 600 hPa to 5.1 m s^{-1} h^{-1} at 650 hPa at 0430 UTC. Considering the evolution and the width of the rear-to-front acceleration, it turned out to be a mesoscale feature, which might be an atmospheric mesoscale response to the mesolow development in the stratiform region during the late mature and dissipating stages. It contributed mainly to the strengthening rear-to-front flow during the dissipating stage in the 26-27 June case. Front-to-rear acceleration generally dominated at middle and high levels $\sim$ $200 - 300$ km behind the leading edge. However, at 0430 UTC, there was a maximum amplitude of 26.0 m s^{-1} h^{-1} . The large acceleration at 0430 UTC might be in part a result of geopotential height errors at upper levels. Near the leading edge there was a vertically extending band of strong front-to-rear pressure gradient acceleration with a width of about $50 - 100$ km. The maximum intensity was generally located between 600 and 700 hPa.

A few hypotheses for the generation of the rear inflow have been proposed. However, the actual mechanisms are still being argued and investigated due to limited observational data (Smull and Houze 1987; Zhang and Gao 1989; Lafore and Moncrieff 1990). In studies of a tropical convective line, LeMone (1983) and LeMone et al. (1984) suggested that hydrostatic generation of pressure minimum under rearward-tilted warm convective updrafts may induce the rear-to-front inflow. Brown (1979) found in a modeling study that the middle level mesolow induced in the stratiform region may drive the air in the rear of the system forward into the MCS. Schmidt and Cotton (1990) proposed a flow blocking theory, but it does not appear to be approriate to apply here due to lack of an upper level rear-to-front flow. In the 26-27 June case, as mentioned earlier, the rearward tilting of the convective band was small and the mesolow induced by the convective updraft could not be sufficiently resolved. On the other hand, the midlevel mesolow induced by the stratiform region was clearly illustrated during the late mature and decaying stages. Referring to figures of relative wind component normal to the squall line (Fig. 4.3), it appears that there are two mechanisms which may serve as possible explanations for the midlevel rear inflow in this case. One is from well behind the system which might be associated with an upper level jet streak, as argued by Zhang and Gao (1989). The other one is simply a direct result of a mesolow and mesohigh couplet that developed from within the stratiform region to the rear of the system. It generated strong rear-to-front pressure gradient acceleration to the rear of the system, which might explain most of the dramatic strengthening of the rear inflow at the back edge of the squall line during the dissipating stage.

The vertical cross-sections of Coriolis acceleration from 0000 to 0430 UTC are illustrated in Figure 6.5. Similar to those results shown by Gallus and Johnson (1992), rear-to-front acceleration dominated over most of the area, except at low levels behind the system, where there was front-to-rear acceleration. The Coriolis acceleration patterns normal to the squall line were generally determined by the wind along the squall line, which showed a southwest wind component over most of the area and a northeast wind component at low levels behind the leading edge. There were only minor changes throughout the evolution.

At 0000 and 0130 UTC (Figs. 6.5a and b), the Coriolis acceleration generally opposed the pressure gradient force, with similar magnitudes to the rear of the squall line. At later times, however, since the pressure gradient acceleration patterns had significant changes, the Coriolis acceleration opposed the pressure gradient force near the leading edge, which tended to decrease the vertical shear of the u component, but reinforced it as rear-to-front acceleration at the back edge of the system except at low levels below 800 hPa. Farther rearward, it opposed the pressure gradient acceleration again. The maximum rear-to-front acceleration was located at upper levels about $300 - 400$ km behind the system. It is associated with a southwest-northeast synoptic jet.

Referring to (2.6), the total acceleration term consists of a local derivative term and horizontal and vertical advection terms. This momentum budget component is usually hard to analyze due to large errors in wind measuring and even larger errors that might result from velocity differentiation. However, in the 26-27 June squall line, the vertical cross-sections of the total acceleration (Figure 6.6) showed relatively consistent features

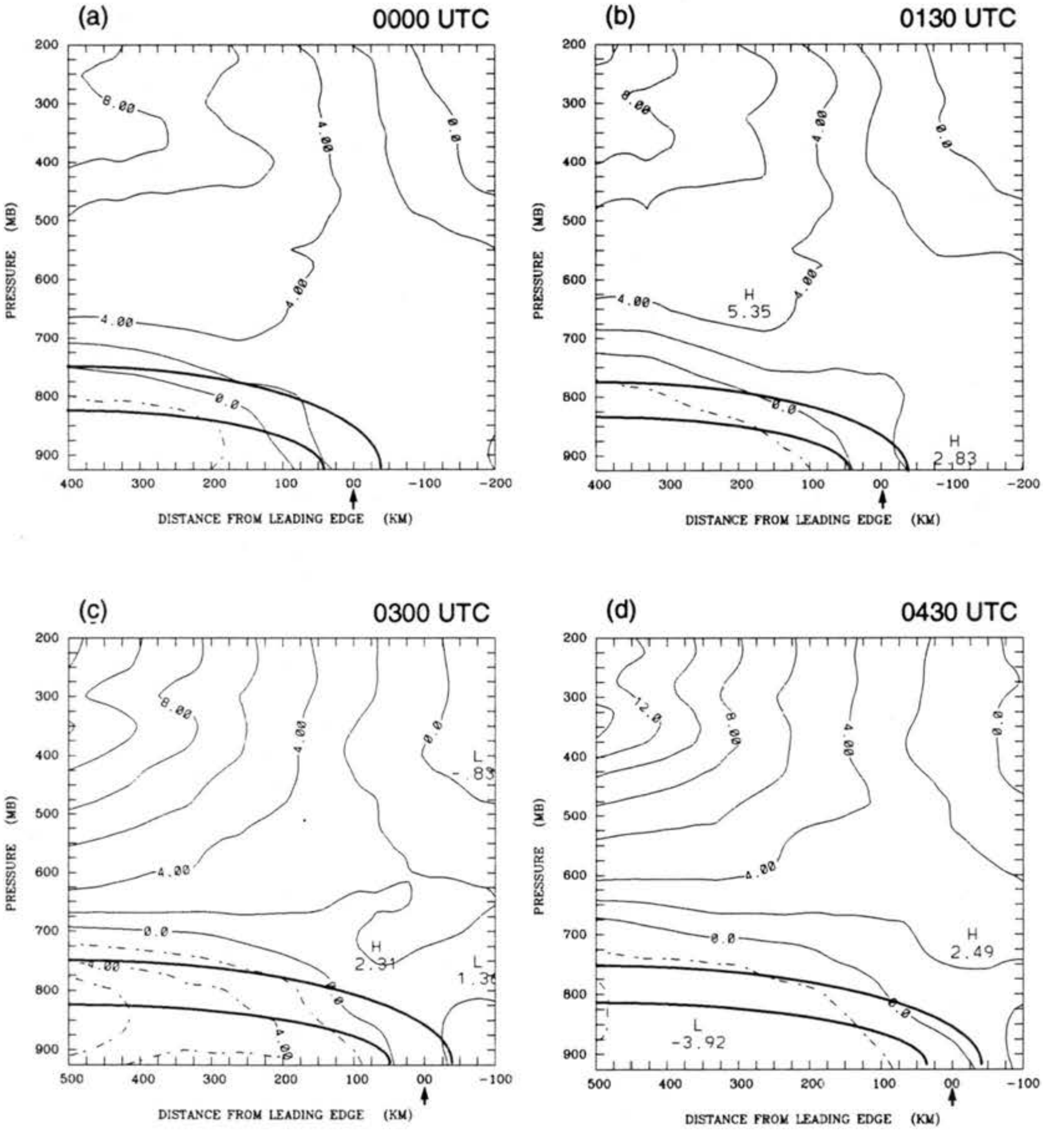

Figure 6.5: Same as Fig. 6.4, except for the component of Coriolis force normal to the line.

from 0000 to 0430 UTC, which, to a certain extent, suggest the good reliability of wind data used in this budget study.

The total acceleration was generally weaker than the pressure gradient force and Coriolis acceleration. It was the most intense within the system. At 0000 and 0130 UTC (Figures 6.6a and b), rear-to-front acceleration generally dominated below 600 hPa, with front-to-rear acceleration aloft. This feature tended to increase the vertical wind shear within the squall line. During the dissipating stage (0300 and 0430 UTC) (Figs. 6.6c and d), the acceleration within the system gradually weakened. There was still rear-to-front acceleration present at middle and low levels within the system with front-to-rear acceleration above. At low levels to the rear of the system, front-to-rear acceleration replaced earlier rear-to-front acceleration.

Figure 6.7 shows the vertical cross-sections of the turbulent stresses from 0000 to 0430 UTC. At 0000 UTC (Fig. 6.7a), rear-to-front acceleration was occurring at low levels around and ahead of the leading edge with a peak value of about 7.1 m s^{-1} h^{-1} at 800 hPa. Above it was a vertical band of front-to-rear acceleration. Behind and ahead of the system, there were two bands showing rear-to-front acceleration.

At 0130 UTC (Fig. 6.7b), the general pattern was very similar to the result at a similar stage (0300 UTC) in the 10-11 June case (Gallus and Johnson 1992, in their Figure 12a). The vertical band of rear-to-front acceleration was located around the leading edge and extended from the surface to midlevels. Ahead of it was a 100-km-wide band of front-to-rear acceleration. Another area of rear-to-front acceleration can also be noticed at low levels 100 km behind the leading edge. Front-to-rear acceleration generally dominated at middle and upper levels to the rear of the system.

During the dissipating stages (0300 to 0430 UTC) (Figs. 6.7c and d), the turbulent stress patterns were generally similar to the pressure gradient acceleration in the convective and stratiform regions, but in opposite directions. The couplet of vertical bands of rear-to-front acceleration in the convective region and front-to-rear acceleration in the stratiform region became more prominent. This structure was also clearly indicated at 0600 and 0730 UTC in the 10-11 June case (Gallus and Johnson 1992, in their Figs. 12b and c). But the

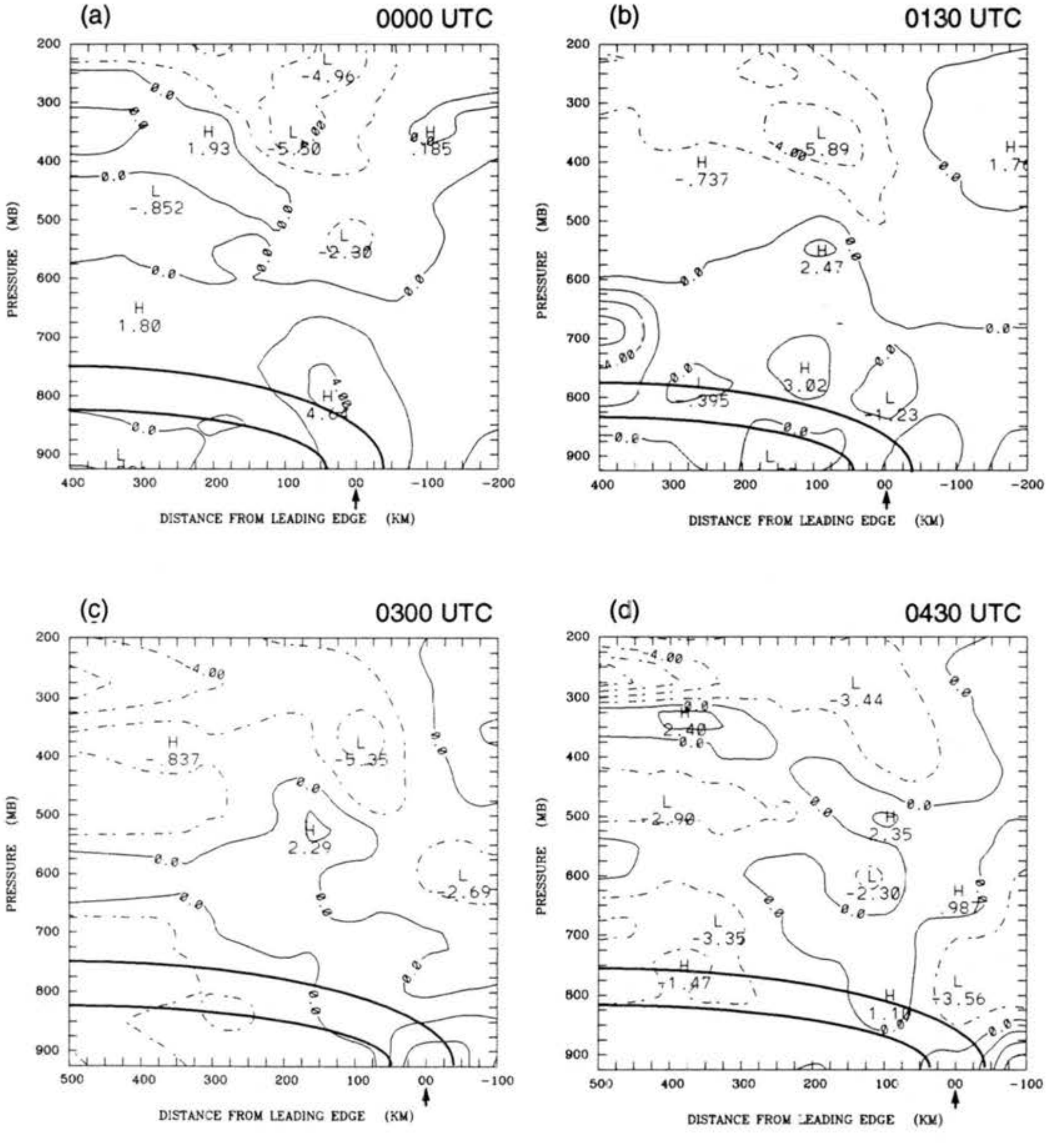

Figure 6.6: Same as Fig. 6.4, except for the component of total acceleration normal to the line.

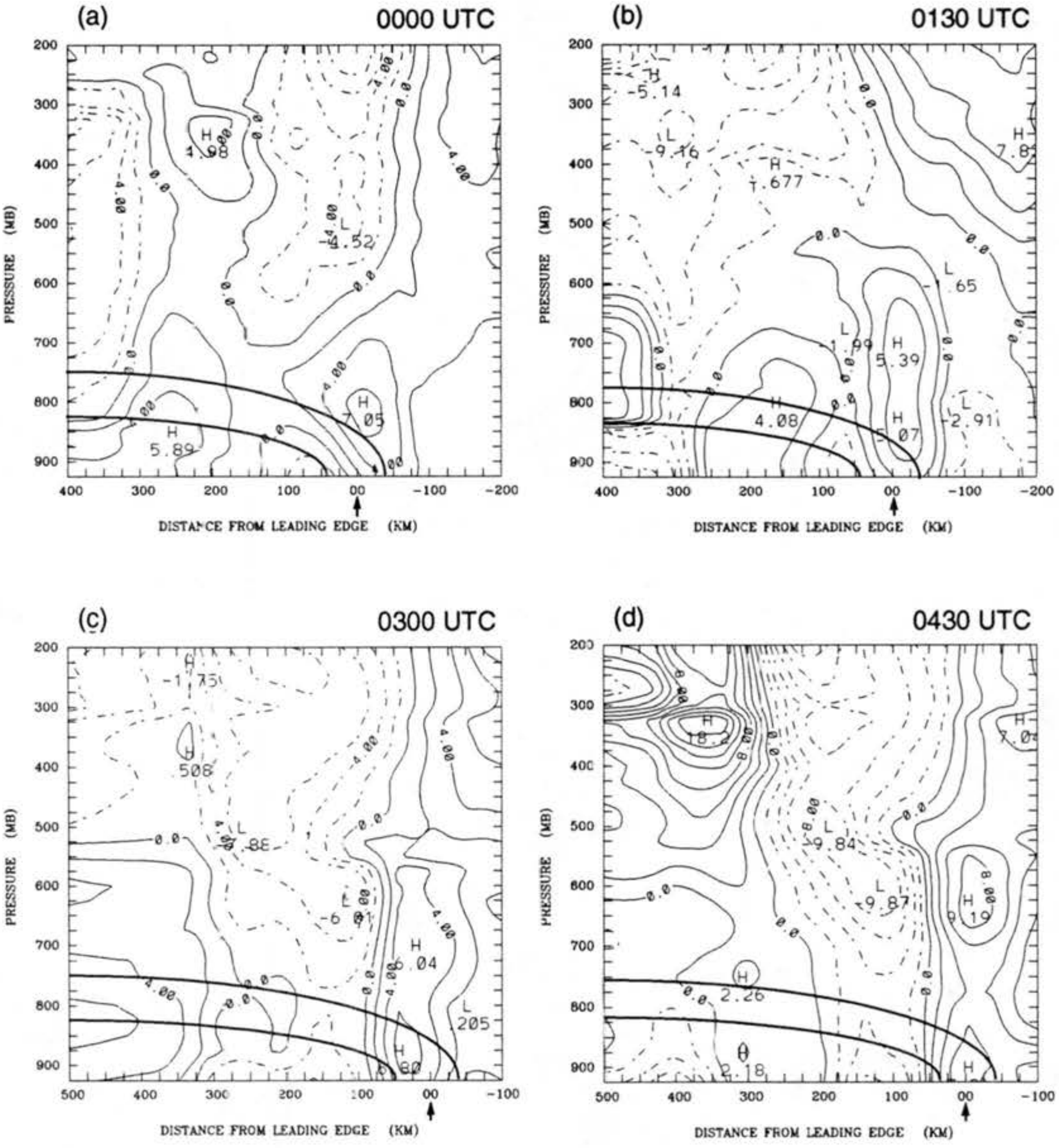

Figure 6.7: Same as Fig. 6.4, except for the component of turbulent stresses normal to the line.

tilting of these two bands was much smaller in the 26-27 June squall line case, consistent with the small tilting feature of vertical velocity, Q_1 and Q_2 shown in previous chapters. With the passage of time, the front-to-rear acceleration at the back edge of the system gradually increased from 6.0 m s^{-1} h^{-1} at 0300 UTC to 9.9 m s^{-1} h^{-1} at 0430 UTC. This strengthening trend was also noticed in the 10-11 June case (Gallus and Johnson 1992).

Figure 6.8 shows the vertical profiles of the four momentum budget components in the convective region from 2100 to 0300 UTC. The pressure gradient acceleration (Fig. 6.8a) was generally directed front to rear at most levels. The magnitude reached a maximum at 2100 UTC (about 8.0 m s^{-1} h^{-1}) and then gradually decreased to 3.0 m s^{-1} h^{-1} at 0000 UTC. At later times, it increased again at middle and low levels. Sanders and Emanuel (1977) studied the vertical profiles of the momentum budget components over a convective line. They found that there was a pronounced peak of front-to-rear pressure gradient acceleration located at about 700 hPa during the squall line development. In a similar momentum budget study of the 10-11 June PRE-STORM case, Gallus and Johnson (1992) also noticed that front-to-rear acceleration peak, but it was found to be located between 550 and 650 hPa during the late mature and decaying stages. They suggested that this peak might be the result of the middle level mesolow in the stratiform region. In the 26-27 June PRE-STORM case, the front-to-rear acceleration was nearly constant with height between 800 and 300 hPa during the developing and mature stages. At the dissipating stage (such as 0430 UTC), there was a front-to-rear acceleration peak at middle levels, similar to the result shown by Gallus and Johnson (1992). At low levels for most times, the profiles indicated rear-to-front acceleration. It is probably due to the development of a mesohigh near the surface within the system. A similar feature was also noticed by Sanders and Emanuel (1977) and Gallus and Johnson (1992).

During the squall line development, Coriolis acceleration in the convective region (Fig. 6.8b) exhibited regular and smooth profiles. Rear-to-front acceleration was occurring at each time throughout the whole troposphere, generally opposing the pressure gradient acceleration. From 2100 to 0000 UTC, the vertical profiles were quite similar to each other. The rear-to-front acceleration increased from low levels and remained nearly constant

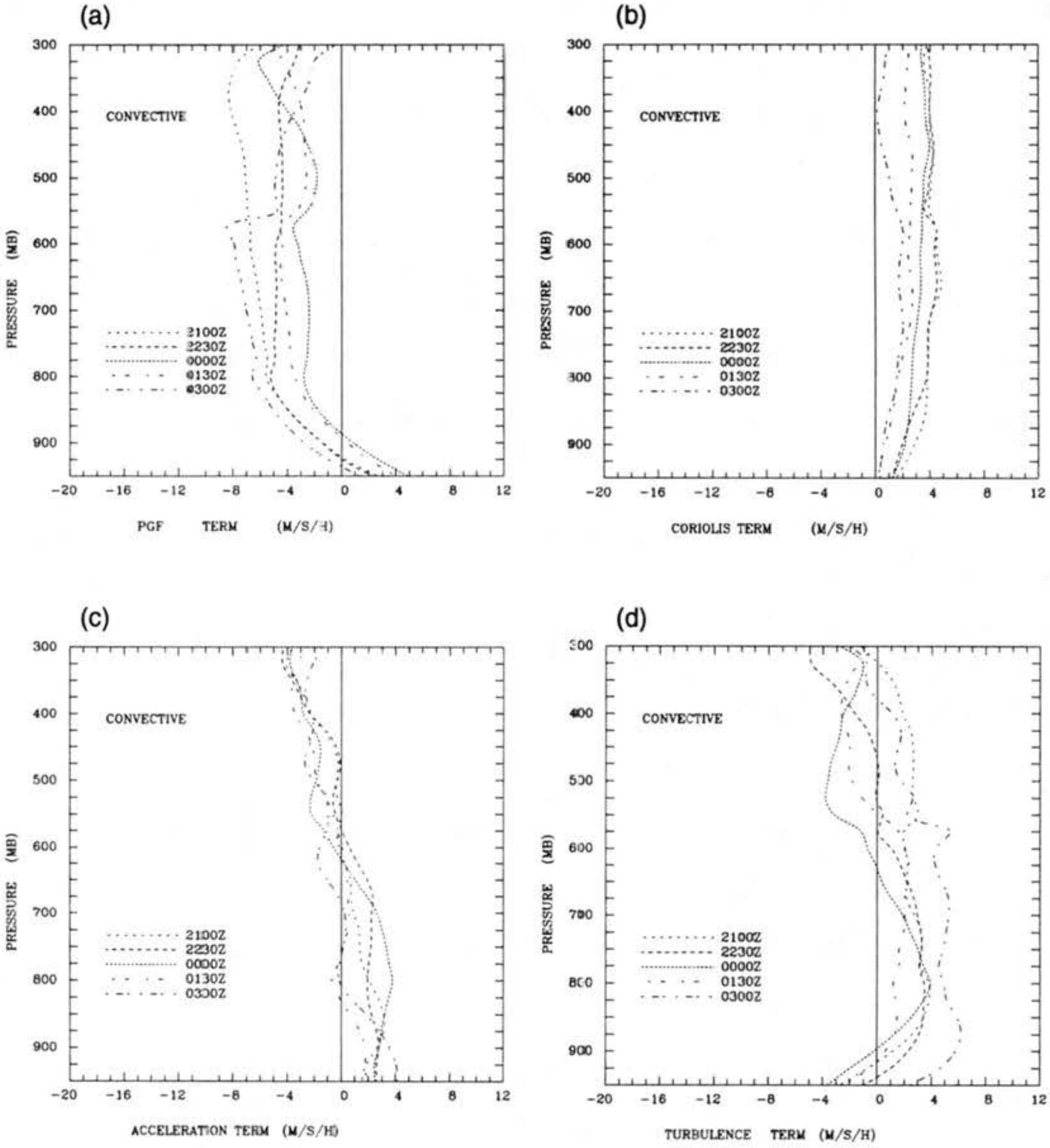

Figure 6.8: Vertical profiles of the momentum budget components averaged over the convective region from 2100 to 0300 UTC in the 26-27 June PRE-STORM case. a) the pressure gradient acceleration, b) Coriolis force, c) total acceleration, d) internal turbulent stresses $\bar{X}$. All units are m s^{-1} h^{-1} .

between 800 and 300 hPa. The maximum acceleration was about 4.0 m s^{-1} h^{-1} . At later times, the acceleration at middle and upper levels gradually decreased. The vertical profiles of Coriolis acceleration were generally similar to the results found by Sanders and Emanuel (1977) and Gallus and Johnson (1992) at middle and high levels except that the magnitudes at the early stages (2100 to 0000 UTC) in the 26-27 June case were larger than the other two cases (about 2.0 m s^{-1} h^{-1} in Gallus and Johnson's and 1.0 m s^{-1} h^{-1} in Sanders and Emanuel's). Compared with the magnitudes of the pressure gradient acceleration, it appears that the Coriolis acceleration was very important in the system development in the 26-27 June PRE-STORM case. At low levels below 825 hPa, Sanders and Emanuel (1977) showed that there was front-to-rear Coriolis acceleration. However, in both the 10-11 June case (Gallus and Johnson 1992) and the 26-27 June cases, only rear-to-front acceleration was found.

In the convective region, the total acceleration (Fig. 6.8c) also indicated a relatively regular evolution. During the developing and early mature stages (2100 to 0000 UTC), rear-to-front acceleration generally occurred below 600 hPa, where front-to-rear acceleration took place above. By 0130 and 0300 UTC, the late mature and dissipating stages, there was still rear-to-front acceleration below 800 hPa and front-to-rear acceleration above 450 hPa. Between 800 and 450 hPa, acceleration became quite weak and occasionally indicated weak front-to-rear acceleration. In the 10-11 June case, Gallus and Johnson (1992) also found that rear-to-front acceleration took place at low levels and front-to-rear acceleration occasionally occurred at middle levels. Farther upward, the acceleration became more variable in the 10-11 June case. The total acceleration profiles from both PRE-STORM squall line cases were different from the results of a Oklahoma squall line studied by Sanders and Emanuel (1977). They showed a very pronounced front-to-rear acceleration peak at about 750 hPa (see their Figure 3), although weak rear-to-front acceleration was also occurring at low and high levels.

The vertical profiles of the residual $\bar{X}$ in the convective region from 2100 to 0300 UTC are illustrated in Fig. 6.8d. At 2100 UTC, the turbulent stress was generally directed from rear to front. By 2230, 0000 and 0130 UTC, rear-to-front acceleration was still present at middle and low levels between 600 and 900 hPa, but it turned into front-to-rear acceleration at upper levels. This feature is similar to those results shown by Sanders and Emanuel (1977) and Gallus and Johnson (1992). However, its magnitude was not as large as other cases. At low levels near the surface, there was also an indication of front-to-rear acceleration. Later (0300 UTC), rear-to-front acceleration dominated from the surface up to 325 hPa with the maximum intensity of 6.0 m s^{-1} h^{-1} located at 850 hPa. The average magnitudes during the early times (about $2 - 4$ m s^{-1} h^{-1}) were generally smaller than the cases studied by Sanders and Emanuel (1977) and Gallus and Johnson (1992). This might indicate that the convection in the 26-27 June case was not as intense as the other two cases and/or the intensity of the convection was not quite well resolved by the sounding network.

Comparing the four momentum budget component profiles with the results of the 10-11 June case, the general patterns in the convective region were similar to each other, except for the smaller magnitudes of the pressure gradient acceleration and turbulent stresses in the 26-27 June case. The Coriolis force was larger during the early stages of the 26-27 June case. Therefore, the Coriolis force played an important role during the developing and early mature stages in opposing the pressure gradient acceleration.

Figure 6.9 illustrates the vertical profiles of u component relative to the ground and vertical momentum flux $\rho\overline{w'u'}$ in the convective region. During the developing and early mature stages (2100 to 0000 UTC), at middle and low levels, the averaged u component gradually turned from weak southeasterly wind at 2100 UTC to northwesterly wind at later times. The vertical wind shear remained quite small and occasionally showed weak positive or negative vertical shear. At the mature and dissipating stages (0130 to 0300 UTC), weak positive wind shear can be seen at low levels below 800 hPa, while between 650 and 800 hPa, the vertical shear still remained small. Above 650 hPa, except at 0300 UTC that small vertical shear was still present at high levels, the profiles at other times were similar to each other and showed strong negative vertical wind shear. The general pattern was distinctly different from the 10-11 June case (Gallus and Johnson 1992)

Negative values of $\rho\overline{w'u'}$ generally dominated throughout the whole troposphere (Fig. 6.9b), except that at 0000 UTC, weak positive values appeared above 475 hPa and below

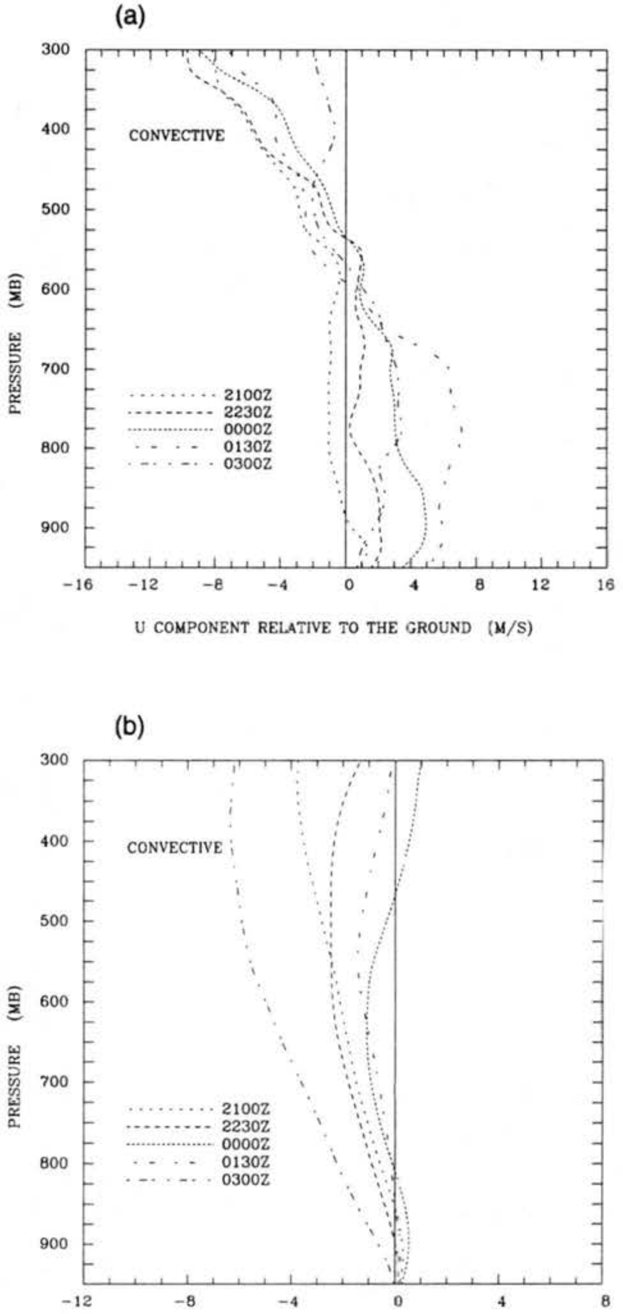

Figure 6.9: Vertical profiles of relative wind component relative to the ground normal to the squall line (a) (in unit of m s^{-1}) and vertical momentum flux (b) (in unit of kg m^{-1} s^{-2}) averaged over the convective region from 2100 to 0300 UTC in the 26-27 June PRE-STORM case.

825 hPa. Therefore, above 600 hPa, the momentum transport was generally upgradient and tended to increase the vertical wind shear. This feature agreed with the results found by LeMone (1983), Smull and Houze (1987), Gao et al. (1990), Lin et al. (1990) and Gallus and Johnson (1992). At middle and low levels, the vertical wind shear remained small and downgradient/upgradient argument is difficult to apply, although at 0130 and 0300 UTC, downgradient transport can be noticed below 800 hPa.

Figure 6.10 shows the vertical profiles of the momentum budget components in the stratiform region from 2230 to 0430 UTC. From 2230 to 0130 UTC, the pressure gradient acceleration (Fig. 6.10a) was in the front-to-rear direction above 850 hPa. The peak acceleration was located at 300 hPa with similar magnitudes (about 7.0 m s^{-1} h^{-1}) to the maximum in the convective region. Weaker front-to-rear acceleration was present at middle and low levels and remained quite constant with height. The patterns were generally similar to that shown at 0300 UTC in the 10-11 June case (Gallus and Johnson 1992, their Fig. 17). During later times, middle and low level front-to-rear acceleration gradually weakened and became rear-to-front acceleration at 0300 and 0430 UTC. Above 550 hPa, there was still front-to-rear acceleration. Below 850 hPa, rear-to-front acceleration was occurring near the surface at all times.

The Coriolis acceleration profiles in the stratiform region (Fig. 6.8b) were similar to those shown in the convective region. At 2230 and 0000 UTC, rear-to-front acceleration took place at all levels and remained nearly constant at middle and high levels. At later times (0130 to 0430 UTC), the magnitudes of rear-to-front acceleration gradually decreased with time. Front-to-rear acceleration can be noticed occurring at low levels and its depth slowly increased. Similar features were also found in the 10-11 June case (Gallus and Johnson 1992).

The balance between the pressure gradient acceleration and Coriolis force would produce rear-to-front acceleration at low levels below 850 hPa for all the times. There was almost no acceleration from 2230 to 0130 UTC and rear-to-front acceleration from 0300 to 0430 UTC at middle levels between 500 and 850 hPa. At upper levels, it would produce front-to-rear acceleration from 2230 to 0130 UTC and rear-to-front acceleration from

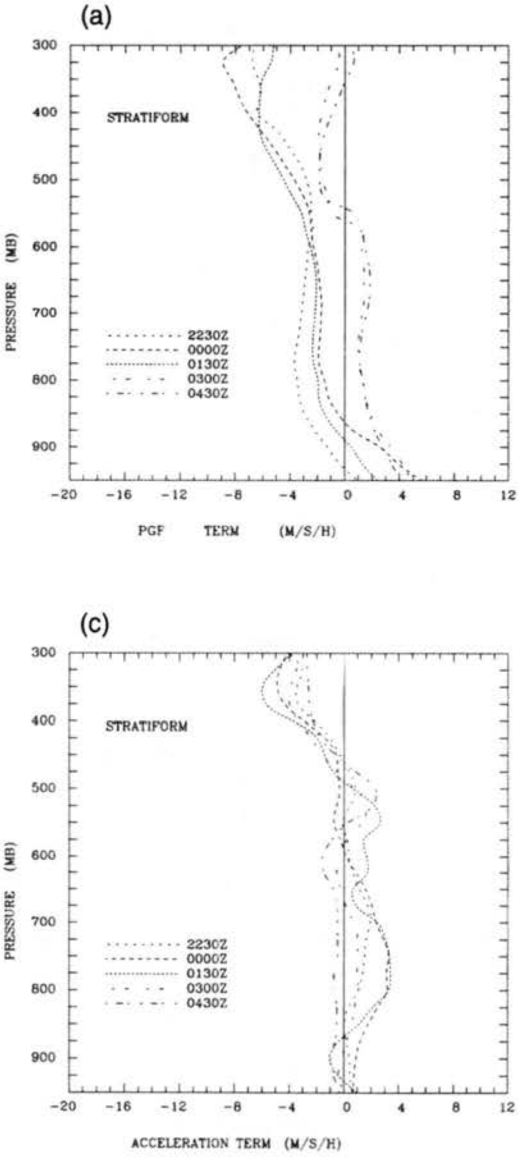

Figure 6.10: Vertical profiles of the momentum budget components averaged over the stratiform region from 2230 to 0430 UTC in the 26-27 June PRE-STORM case. a) the pressure gradient acceleration, b) Coriolis force, c) total acceleration, d) internal turbulent stresses $\bar{X}$. All units are m s^{-1} h^{-1} .

0300 to 0430 UTC. This situation was different from the results of the 10-11 June case (Gallus and Johnson 1992), which showed front-to-rear acceleration at nearly all levels. The difference may be attributed to the momentum budget evolution at different stages.

The vertical profiles of total acceleration in the stratiform region (Fig. 6.10c) are quite similar to those in the convective region. Front-to-rear acceleration took place at upper levels above 450 hPa. The intensity increased from the developing to mature stages and reached the maximum at 0130 UTC (about -6.0 m s^{-1} h^{-1}), then gradually decreased during the dissipating stage. Below 450 hPa, rear-to-front acceleration can be seen during early times. At later times, the total acceleration decreased and approached zero at middle and low levels.

In the stratiform region, the variation of the internal turbulent stresses with time was large. At low levels below 900 hPa, front-to-rear acceleration was generally dominant at each time. During early times (2230 to 0130 UTC), rear-to-front acceleration was present at middle and low levels between 650 and 900 hPa. Weak front-to-rear acceleration was occurring at high levels and some rear-to-front acceleration was occasionally indicated at 0130 UTC. During the dissipating stage (0300 to 0430 UTC), front-to-rear acceleration almost occurred at all levels except a shallow layer of rear-to-front acceleration around 500 hPa.

The vertical profiles of the u component relative to the ground and vertical momentum flux in the stratiform region from 2230 to 0430 UTC are shown in Figure 6.11. Strong negative wind shear was present above 675 hPa for each time (Fig. 6.11a). At low levels, however, the wind profiles were quite different. At 0130 UTC, positive wind shear was shown below 800 hPa and negative shear above, while at 0300 and 0430 UTC, weak positive wind shear occurred from the surface up to 700 hPa. During the early times (2230 and 0000 UTC), the wind profiles at low levels were quite variable with height.

The momentum transport in the stratiform region also indicated quite different patterns. At 2230 and 0000 UTC, the momentum flux was very small and there appeared almost no flux transport during the early stages in the stratiform region. At 0130 UTC, downgradient transport can be seen below 800 hPa with upgradient transport above 800

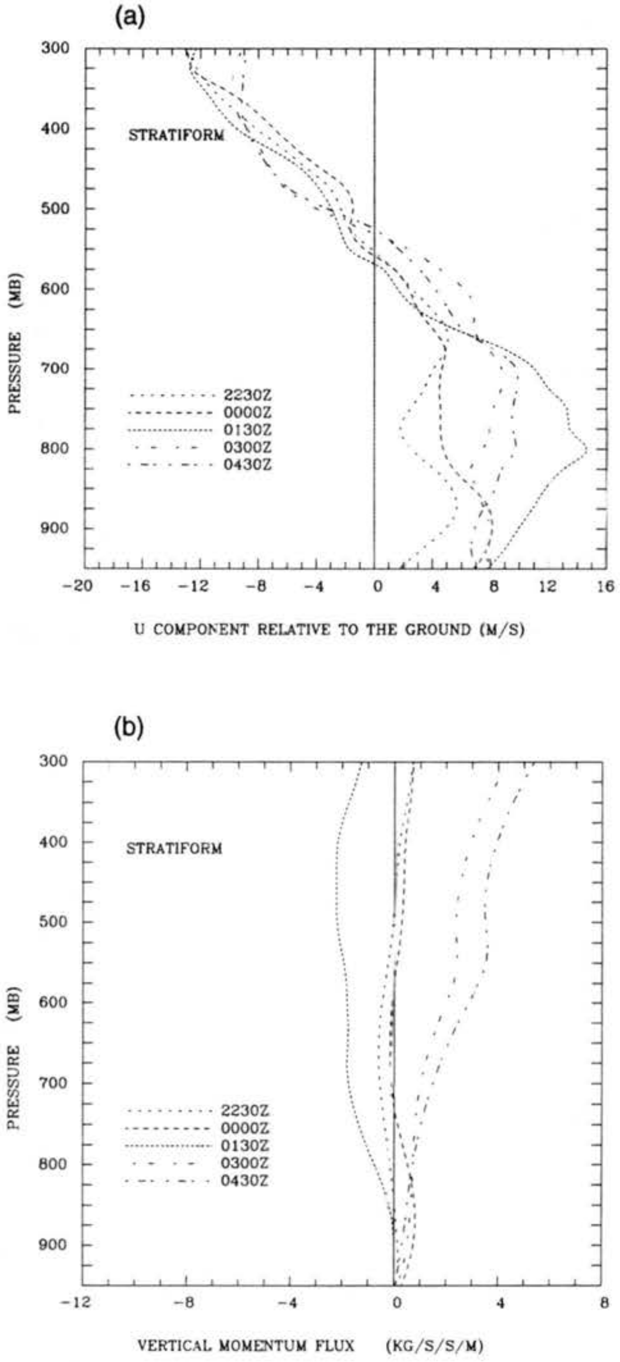

Figure 6.11: Vertical profiles of relative wind component relative to the ground normal to the squall line (a) (in unit of m s^{-1}) and vertical momentum flux (b) (in unit of kg m^{-1} s^{-2}) averaged over the stratiform region from 2230 to 0430 UTC in the 26-27 June PRE-STORM case.

hPa up to high levels. During the decaying stage, the vertical momentum flux was generally positive. Thus, upgradient momentum transport took place at low levels below 675 hPa, while downgradient transport occurred above.

Chapter 7

SECONDARY CIRCULATION FORCING AND FRONTOGENESIS

There have been many studies about secondary circulation and frontogenesis, usually concentrating on the interaction between frontogenesis and secondary circulation with the environment from the view points of kinematics and thermodynamics. Very few quantitative diagnostic studies have been performed to look at the diabatic heating effect, which may have similar or higher order importance on frontogenesis and forced secondary circulation. Rutledge (1989), using three-dimensional cloud model output, diagnosed the diabatic heating effect in the frontogenesis equation in the cross-front section of a frontal rainband. He found the diabatic heating process was important to the maintenance of the cross-frontal temperature gradient. The density contrast was generally maintained by heating associated with condensation ahead and cooling resulting from evaporation behind. Although the spatial and temporal distribution of diabatic heating is very difficult to determine, some researchers (e.g., Shapiro 1983; Trier 1987; Hertenstein and Schubert 1991, etc) tried to use simple heating profiles to parameterize the actual diabatic heating function and study the circulation patterns within mesoscale convective systems. Some interesting features were observed. However, there are limitations to this approach.

In this chapter, the apparent heat source Q_1, diagnosed from previous calculation, is used to approximately represent the diabatic heating effect. With the advantage that Q_1 has values over the entire PRE-STORM domain, the three dimensional heating features can be relatively accurately represented. The Sawyer-Eliassen secondary circulation equation is used as a diagnostic tool. Instead of trying to solve a streamfunction in the second-order partial differential equation, our main objective is to quantitatively compare the importance of the forcing terms on the right hand side of the equation. Miller's frontogenesis equation is also used to study the relative influence of the diabatic heating effect on frontogenesis. Section 7.1 will briefly introduce the Sawyer-Eliassen secondary circulation equation. Section 7.2 will discuss the evolution of each forcing term in the Sawyer-Eliassen equation and document the importance of the diabatic heating effect. Section 7.3 will use the Miller's frontogenesis equation to evaluate the diabatic heating effect on frontogenesis.

7.1 The Sawyer-Eliassen secondary circulation equation

If a frontal zone is sufficiently straight and along-front variations are small enough, the along-front wind component can be considered as geostrophic. Therefore, the ageostrophic circulation can be simply described in the cross-front section (Keyser and Shapiro 1986).

Under the assumptions of

$$| u_{ag} | \ll | u_g | \tag{7.1}$$

$$| \frac{du_{ag}}{dt} | \ll | \frac{du_g}{dt} | \tag{7.2}$$

$$| \frac{\partial u_{ag}}{\partial x} | \ll | \frac{\partial v_{ag}}{\partial y} | \simeq | \frac{\partial \omega}{\partial p} | \tag{7.3}$$

$$f = constant \tag{7.4}$$

The geostrophic momentum equation (Eliassen 1948), after averaging, can be written as:

$$\frac{d\overline{m}}{dt} = -\frac{\partial \overline{\phi}}{\partial x} + \overline{F}_x - \frac{\partial}{\partial p}\overline{\omega' m'} \tag{7.5}$$

$$\frac{d\overline{\theta}}{dt} = \overline{\dot{\theta}} - \frac{\partial}{\partial p}\overline{\omega'\theta'} \tag{7.6}$$

where

$$\frac{d}{dt} = \frac{\partial}{\partial t} + \overline{u}_g\frac{\partial}{\partial x} + (\overline{v}_g + \overline{v}_{ag})\frac{\partial}{\partial y} + \overline{\omega}\frac{\partial}{\partial p} \tag{7.7}$$

The bar represents an average over a 50 × 50 km^2 area. u_g and u_{ag} represent geostrophic and ageostrophic components along the line, where v_g and v_{ag} are geostrophic and ageostrophic components normal to the line. ω is verticl p velocity. f is Coriolis parameter. $m = u_g - fy$ is absolute momentum (Eliassen 1962), F_x is the frictional term along the front. $\dot{\theta}$ represents the diabatic heating effect and $-\frac{\partial}{\partial p}\overline{\omega' m'}$ and $-\frac{\partial}{\partial p}\overline{\omega'\theta'}$ are the vertical convergence of eddy transport. In the following paragraphs, for simplicity, the bar will be omitted except for turbulent terms.

The mass continuity equation can be written as:

$$\frac{\partial v_{ag}}{\partial y} + \frac{\partial \omega}{\partial p} = 0 \tag{7.8}$$

An ageostrophic streamfunction ψ can be introduced so that

$$v_{ag} = -\frac{\partial \psi}{\partial p}, \qquad \omega = \frac{\partial \psi}{\partial y} \tag{7.9}$$

By taking $\frac{\partial}{\partial p}$ of (7.5) and $\frac{\partial}{\partial y}$ of (7.6), followed by a series of algebra, we can get the Sawyer-Eliassen secondary circulation equation:

$$\begin{aligned}(-\gamma\frac{\partial \theta}{\partial p})\frac{\partial^2 \psi}{\partial y^2} &+ (2\frac{\partial m}{\partial p})\frac{\partial^2 \psi}{\partial y \partial p} + (-\frac{\partial m}{\partial y})\frac{\partial^2 \psi}{\partial p^2} + (\frac{\partial m}{\partial p}\frac{dln\gamma}{dp})\frac{\partial \psi}{\partial y} \\ &= -2J_{yp}(u_g, v_g) + \frac{\partial F_x}{\partial p} - \gamma\frac{\partial}{\partial y}(\frac{d\theta}{dt}) + F_t \end{aligned} \tag{7.10}$$

where

$$J_{yp}(u_g, v_g) = \frac{\partial u_g}{\partial y}\frac{\partial v_g}{\partial p} - \frac{\partial u_g}{\partial p}\frac{\partial v_g}{\partial y}, \tag{7.11}$$

$$\gamma = \frac{R}{fP_0}(\frac{P_0}{P})^{C_v/C_p}, \tag{7.12}$$

$$F_t = -\frac{\partial^2}{\partial p^2}\overline{m'\omega'} \tag{7.13}$$

The Sawyer-Eliassen secondary circulation equation is a linear, second order partial differential equation. It was first formulated by Sawyer (1956) to study the forcing of stretching deformation and then was expanded by Eliassen (1962) to investigate the forcing of both stretching and shearing deformation.

The coefficients of the second-order terms on the left hand side of the equation are static stability, baroclinicity and inertial stability, respectively. If $(-\gamma\frac{\partial\theta}{\partial p})(-\frac{\partial m}{\partial y})-(\frac{\partial m}{\partial p})^2 = \gamma P_2 > 0$, where P_2 is potential vorticity, the Sawyer-Eliassen secondary circulation equation is elliptic. Provided that the distributions of m, θ, and the forcing terms are known and the boundary conditions are specified, the streamfunction ψ is uniquely determined by the forcing terms. Positive (negative) values of the forcing correspond to relative minima (maxima) in ψ and are associated with a thermodynamically direct (indirect) circulation. When potential vorticity $P_2 < 0$, the transverse ageostrophic circulation may be self-excited, especially by symmetric baroclinic instability (Hoskins 1974; Orlanski and Ross 1977; Emanuel 1979).

Figure 7.1 shows the vertical cross-sections of γP_2 at 2230 and 0300 UTC, respectively. At 2230 UTC, two narrow vertical bands of negative potential vorticity were located at the leading edge and 175 km behind the leading edge. They connected with each other at upper levels between 200 and 300 hPa. Positive potential vorticity basically dominated other regions. By 0300 UTC, the two narrow vertical bands of negative potential vorticity can still be noticed at 100 km and 300 km behind the leading edge, but at this time they were generally concentrated at middle and low levels. At about 400 km behind the leading edge, the entire troposphere was dominated by negative potential vorticity. Positive potential vorticity was still dominant at other regions. At regions of negative potential vorticity, the Sawyer-Eliassen secondary circulation equation is hyperbolic and the transverse ageostrophic circulation will arise in response not only to the forcing terms,

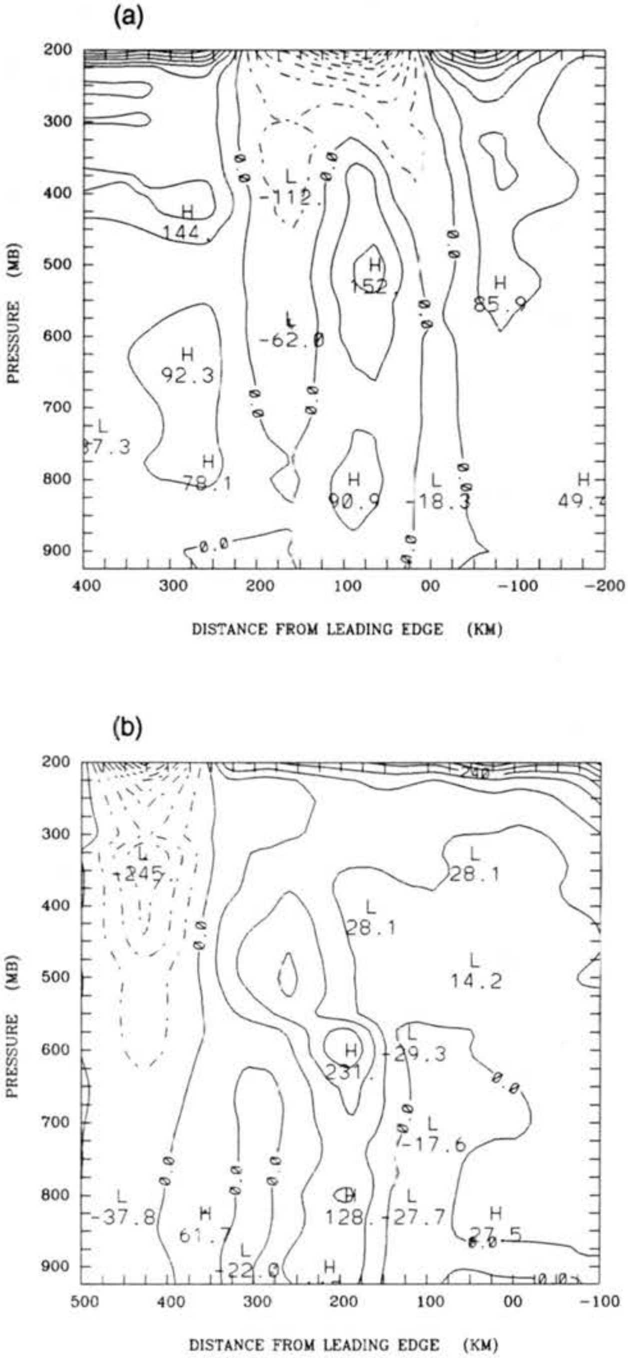

Figure 7.1: Vertical cross sections of γP_2 (in unit of m^2 s^{-2} Pa^{-2} × 10^{-8}), where P_2 is the potential vorticity. a) 2230 UTC, b) 0300 UTC.

but also to self-exciting instabilities, such as symmetric baroclinic instability. Hence, in this chapter, it is our intent to quantitatively evaluate each forcing term at the right hand side of the Sawyer-Eliassen equation, rather than propose a more general formulation for the streamfunction ψ to study its response to both forcing terms and self-exciting instabilities.

The Jacobian term (the first term) on the right hand side of the Sawyer-Eliassen secondary circulation equation can be separated into geostrophic stretching deformation and geostrophic shearing deformation terms. They are indications of the geostrophic forcing on the transverse ageostrophic circulation and were emphasized in Eliassen's (1962) study. The second term is the frictional term. It is small except near the surface and will not be considered in this case. The differential diabatic heating term (the third term) is an important forcing mechanism for generating a secondary circulation. It is usually ignored due to unavailability of data. In this study, we use observed grided data of Q_1 to approximately represent the diabatic heating effect in the Sawyer-Eliassen secondary circulation equation, rather than use simple analytic heating profiles. Their relationship can be written as follows:

$$Q_1 = c_p (P/P_0)^{R/c_p} (\frac{d\theta}{dt}) \tag{7.14}$$

The fourth term suggests additional circulation forcing by vertical Laplacian of turbulent motions. Although it might be important, especially at the region of strong convection and near clear air turbulence (Shapiro 1981), there is no data available in this study to assess its magnitude, so it is not considered here.

The circulation forcing on the right hand side of the Sawyer-Eliassen secondary circulation equation can be rewritten as follows:

$$Forcing = 2\gamma \frac{\partial v_g}{\partial y} \frac{\partial \theta}{\partial y} + 2\gamma \frac{\partial u_g}{\partial y} \frac{\partial \theta}{\partial x} - \frac{R}{f c_p P} \frac{\partial Q_1}{\partial y} \tag{7.15}$$

where the first term is geostrophic stretching deformation, the second is geostrophic shearing deformation and the third term represents the diabatic heating effect.

7.2 Circulation forcing

Figure 7.2 illustrates the vertical cross-sections of the forcing terms at 2230 UTC. The geostrophic stretching deformation (Fig. 7.2a) was generally quite weak. Negative forcing was located between 500 and 750 hPa within the squall line system and at middle and upper levels ahead of the leading edge. The low level cold front zone is specified by isentrope 300 K and 305 K. Around the frontal zone, there was weak positive forcing. The geostrophic shearing deformation showed a vertical band (about 100 km wide) of positive forcing just behind the leading edge. Ahead of the leading edge and behind the positive forcing band were two vertically distributed negative forcing bands. Compared with the two geostrophic forcing terms, the differential diabatic heating term (Fig. 7.2c) was about one order magnitude larger within the squall line, implying the dominance of the secondary circulation forced by the diabatic heating effect in the mesoscale convective system. A positive and negative couplet was quite pronounced within the system. About 50 km behind the leading edge, there was a vertical band of positive forcing (maximum was about 10.2×10^{-8} m s^{-2} Pa^{-1} at 525 hPa) with width of 200 km. Ahead of it was a 100 km wide vertical band of negative forcing (minimum was -14.9×10^{-8} m s^{-2} Pa^{-1} at 550 hPa). Outside the squall line, the forcing weakened and had magnitudes similar to those geostrophic forcing terms. The total forcing term (Fig. 7.2d) was similar to the differential diabatic heating term showing vertical bands (about 100 km) of positive forcing 50 km behind the leading edge and negative forcing ahead.

Figure 7.3 shows the forcing terms at 0300 UTC, when the squall line evolved into its dissipating stage. The geostrophic stretching deformation (Fig. 7.3a) was still quite weak. At middle and low levels, it was dominated by positive forcing except for a region of negative forcing between 700 and 850 hPa 300 km behind the leading edge. At upper levels between 300 and 400 hPa, there was a horizontal band of negative forcing. The geostrophic shearing deformation term (Fig. 7.3b) showed a vertical band of positive forcing around the leading edge, similar to that shown at 2230 UTC. Behind it was a band of negative forcing. Another region of positive forcing can be noticed at middle and

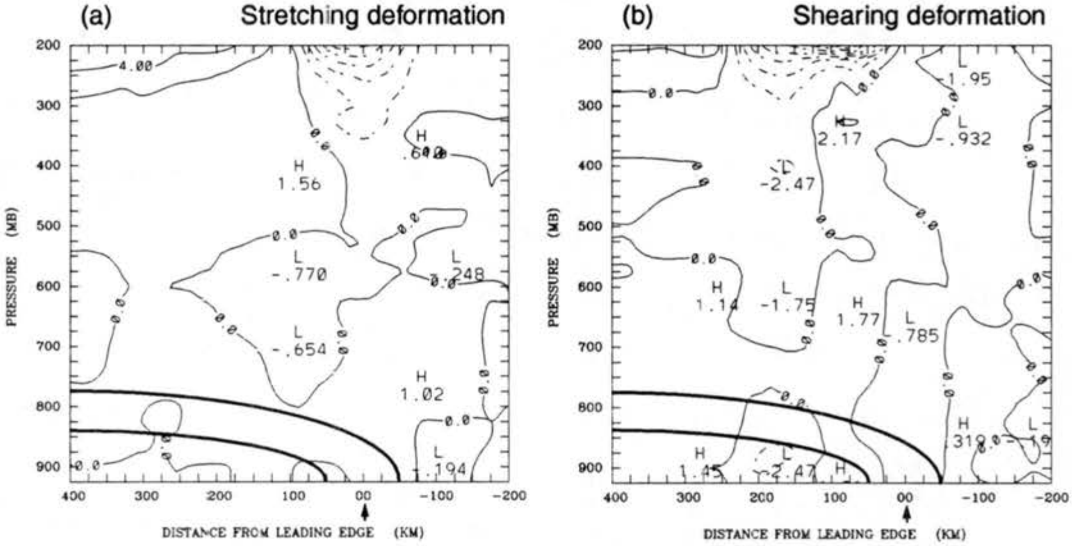

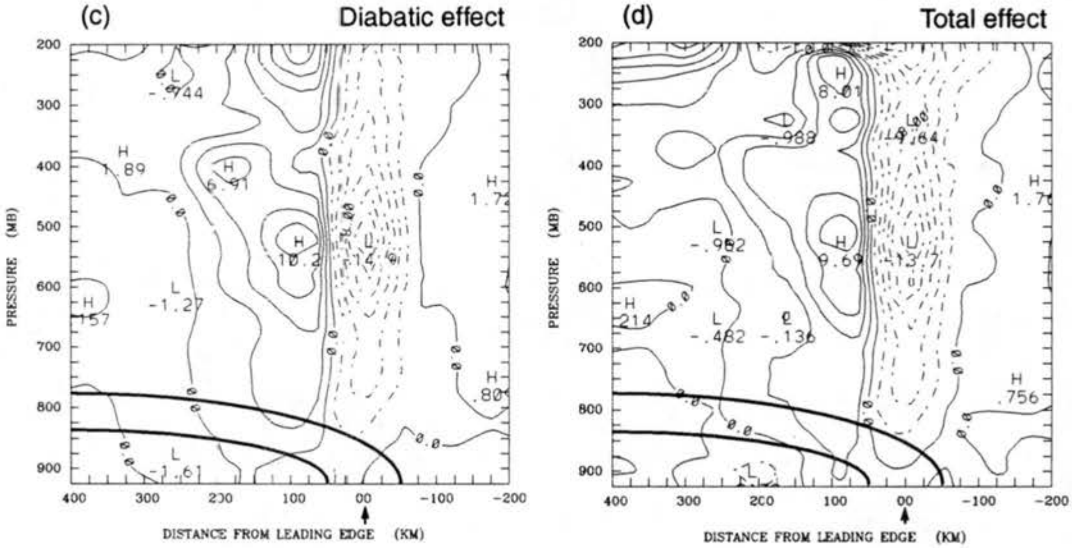

Figure 7.2: Vertical cross sections of forcing terms of the Sawyer-Eliassen secondary circulation equation at 2230 UTC (in unit of m s^{-2} Pa^{-1} $\times$ 10^{-8}). a) geostrophic stretching deformation, b) geostrophic shearing deformation, c) diabatic effect, d) combined geostrophic deformation and diabatic heating effect.

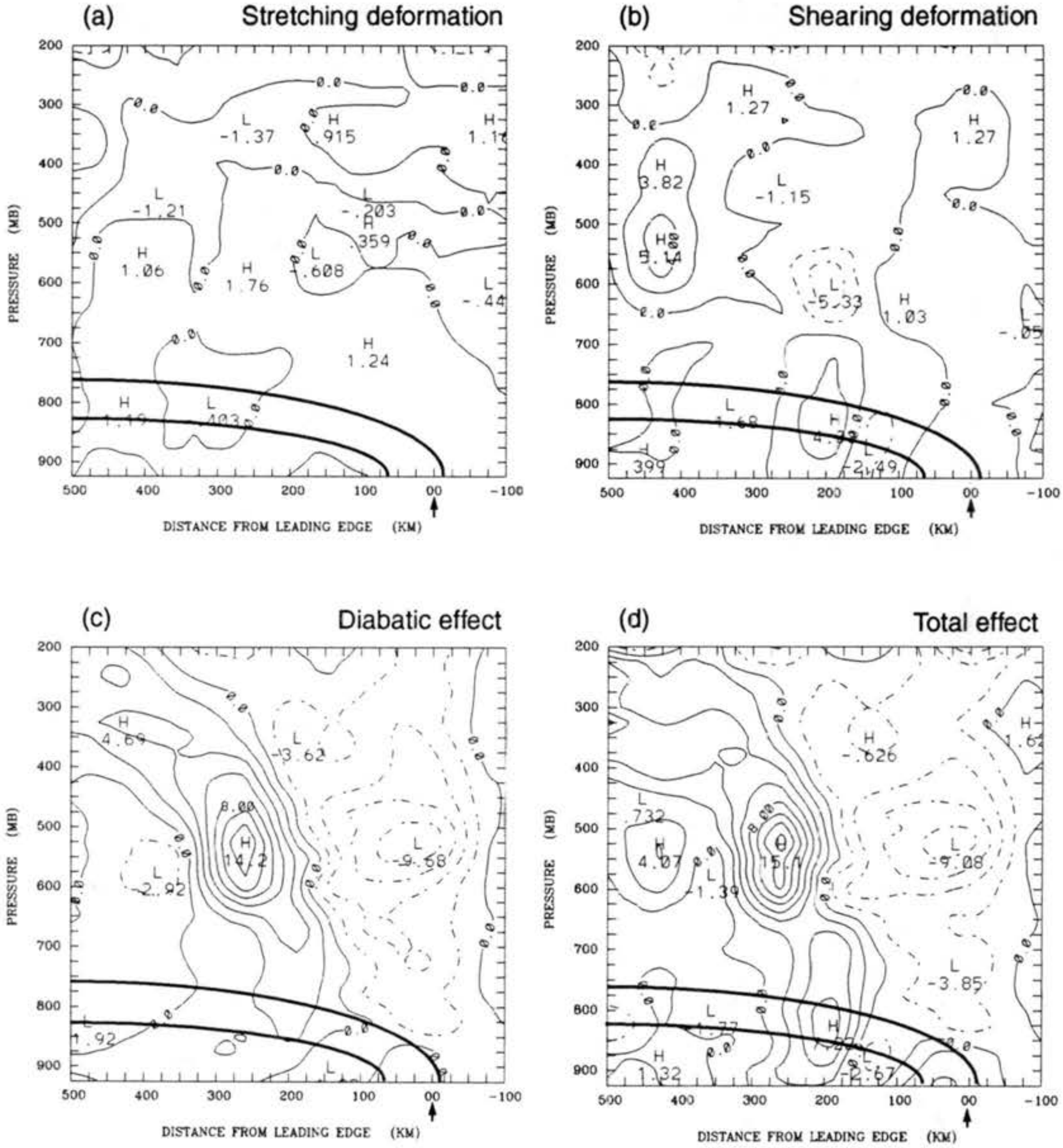

Figure 7.3: As in Fig. 7.2, except for 0300 UTC.

upper levels 400 km behind the leading edge. However, the large forcing value may not be real, but a result of data problems near the edge of the domain. The differential diabatic heating term was still the dominant forcing (see Figs. 7.3c and d). Within the squall line system, negative forcing dominated throughout almost the entire troposphere with the maximum intensity of 9.7×10^{-8} m s^{-2} Pa^{-1} located at 525 hPa. To the rear of the system was a 150 km wide rearward tilting band of positive forcing (the peak value was 14.2×10^{-8} m s^{-2} Pa^{-1} at 550 hPa).

In general, above the frontal zone around the squall line, the differential diabatic heating effect dominated the forcing terms at the right hand side of the Sawyer-Eliassen equation. Its forcing was the most intense at middle levels. At low levels around the cold front, geostrophic forcing terms had similar magnitudes as the differential diabatic heating term. It can be seen that the prominent effects of the diabatic heating at 2230 UTC are above the surface frontal zone. However, ~ 100 to 200 km behind the leading edge there was some positive forcing in the frontal zone, indicating the forcing of a thermally direct circulation. Physically, this forcing comes from condensational heating at the leading edge and low-level evaporative cooling to the rear, as also discovered by Rutledge (1989).

7.3 The frontogenesis equation

The frontogenesis equation (Miller 1948; Sanders 1955) is a useful tool to study frontogenetical effect. Assuming the y direction is pointing to cold air normal to the front, the frontogenesis equation can be written as the following:

$$\frac{d}{dt}(\frac{\partial\theta}{\partial y}) = \frac{1}{c_p}(\frac{P_0}{P})^{R/c_p}\frac{\partial Q_1}{\partial y} - \frac{\partial v}{\partial y}\frac{\partial\theta}{\partial y} - \frac{\partial\omega}{\partial y}\frac{\partial\theta}{\partial p} \tag{7.16}$$

The first term represents the differential diabatic heating effect. The second term is the kinematic effect of confluence deformation and the third term is the tilting effect.

If

$$\frac{d}{dt}(\frac{\partial\theta}{\partial y}) < 0, \qquad frontogenesis. \tag{7.17}$$

$$\frac{d}{dt}(\frac{\partial \theta}{\partial y}) > 0, \qquad frontolysis. \tag{7.18}$$

Figure 7.4 illustrates the vertical cross-sections of different effects on the frontogenesis equation at 2230 UTC. The differential diabatic heating term (Fig. 7.4a) was positive in a vertical band around the leading edge with width of about 100 km. The maximum intensity was located at 525 hPa with magnitude of 28.3 × 10^{-8} K m^{-1} s^{-1} . Ahead of it was a region with weak negative values. From 50 to 200 km behind the leading edge, negative values (the minimum value was -19.6 × 10^{-8} K m^{-1} s^{-1} at 550 hPa) occurred throughout most of the entire troposphere above the front. Farther rearward there was a region favoring weak frontolysis. At low levels around the cold front, negative values can be seen just ahead of the leading edge, supporting frontogenesis in front of the system. Behind the leading edge, there was a 100-km-wide region favoring frontolysis. Between 100 and 200 km behind the leading edge within the frontal zone, it was again dominated by frontogenetical effect. This could be explained physically in terms of condensation heating near the leading edge and evaporational cooling behind, as in Rutledge (1989). The kinematic effect of confluence term (Fig. 7.4b) was generally one order of magnitude smaller than the diabatic heating effect, however, there was weak frontogenesis in the frontal zone near the surface and ahead of it. Positive values can be noticed at middle levels between 500 and 750 hPa within the system. To the rear of the system there were primarily negative values. The spatial distribution of the tilting term (Fig. 7.4c) was quite similar to that of the diabatic heating term, except the sign was opposite. Near the leading edge, there was a negative-value band with maximum intensity of 27.2 × 10^{-8} K m^{-1} s^{-1}. Behind it (about 50 km behind the leading edge) there was a vertical band of positive values, favoring frontolysis. To a large extent, the differential diabatic heating term and the tilting term opposed each other above the frontal zone at middle and upper levels. However, at low levels around the frontal zone, some interesting features can be noticed. The tilting term indicated frontogenetical effect ahead of the leading edge and frontolytical effect within the frontal zone behind the leading edge. Therefore, all the three terms

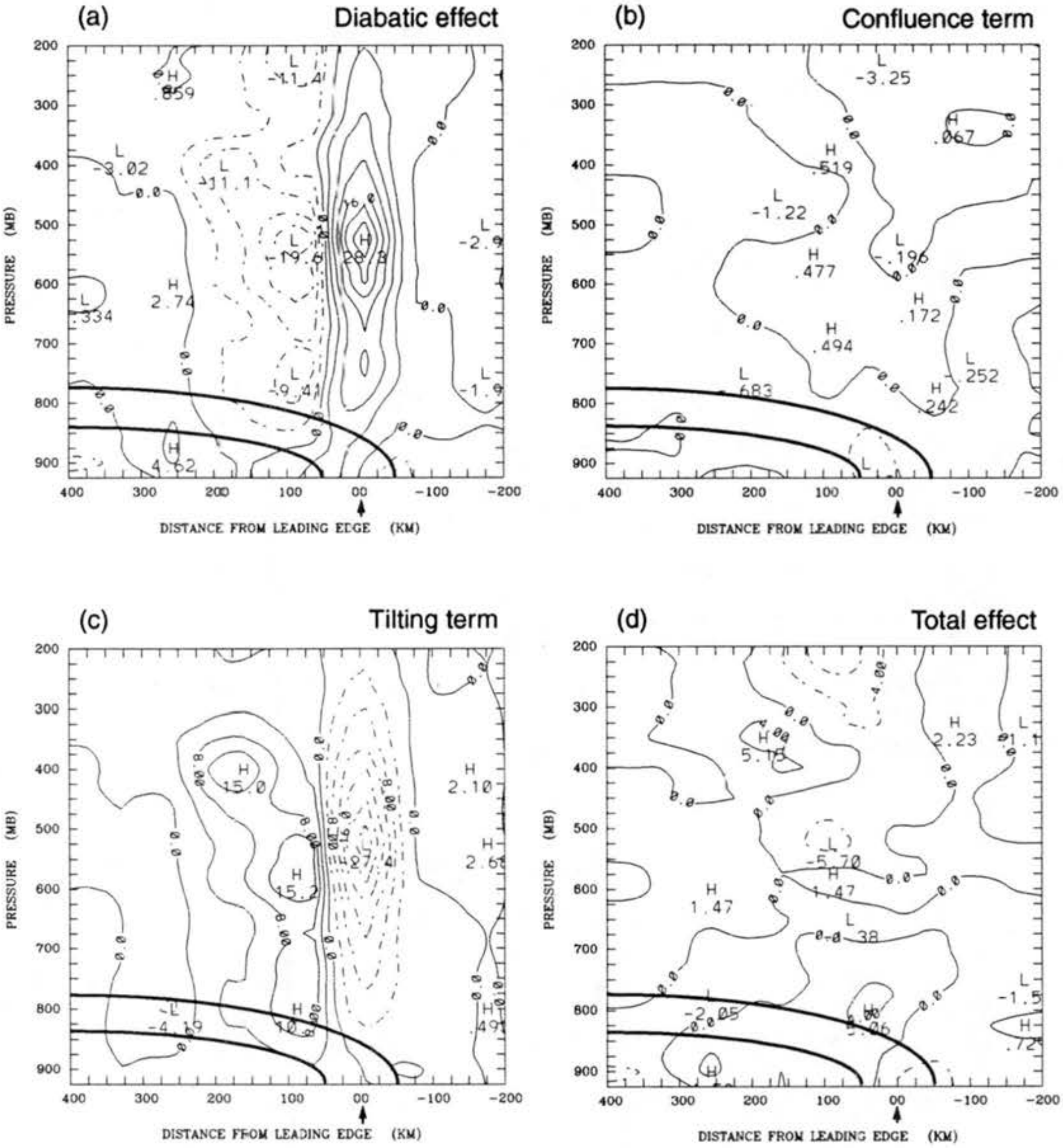

Figure 7.4: Vertical cross sections of contribution by different effects to the frontogenesis equation at 2230 UTC (in unit of K m^{-1} s^{-1} $\times$ 10^{-8}). a) differential diabatic heating effect, b) kinematic effect of confluence deformation, c) tilting term, d) the total effect.

showed frontogenetical effect ahead of the leading edge. Although the total effect (Fig. 7.4d) was generally quite weak, negative values were generally present at low levels around and ahead of the leading edge, suggesting a favoring condition for frontogenesis ahead of the front. Positive values occurred about 25 km behind of the leading edge, indicative of frontolysis effect. It is proposed that this pattern partly explains the movement of the surface front during the developing and early mature stages.

During the dissipating stage (0300 UTC) (Figure 7.5), the couplet of positive and negative bands became broader in the horizontal. The differential diabatic heating term (Fig. 7.5a) showed positive values within the squall line system and a negative vertical band behind. Weak frontogenetical effect can still be noticed in the frontal zone near the surface. But at this time, the frontolytical effect was present ahead of the leading edge. The tilting term (Fig. 7.5c) indicated a similar pattern with opposite sign. However, a frontolytical effect also occurred ahead of the leading edge at low levels, and even extended a little bit behind the leading edge. About 100 km behind the leading edge, it was generally dominated by positive values favoring frontolysis. Although it was weak, the confluence term (Fig. 7.5b) was generally dominated by negative values behind the leading edge, except several small regions of positive values. The total effect is shown in Fig. 7.5d. Within the frontal zone near the surface, the frontogenetic effect was restricted within a 100-km wide region. From surface to middle levels ahead of the leading edge, frontolysis was generally dominant, which might explain why the movement of both the front and the squall line almost ceased during the dissipating stage.

In general, the confluence term may have contributed to frontogenesis at low levels behind the leading edge during almost the entire lifetime, but its effect was generally quite small. The differential diabatic heating and tilting terms (both are manifestations of responses to the squall line), although were one order of magnitude larger than the confluence term, tended to oppose each other. Therefore, although the low level cold front contributed to triggering the intense convection within the squall line, any feedback to frontogenesis turned out to be small. At low levels during the system developing stage, the total effect indicated weak frontogenetic effect around and ahead of the leading edge

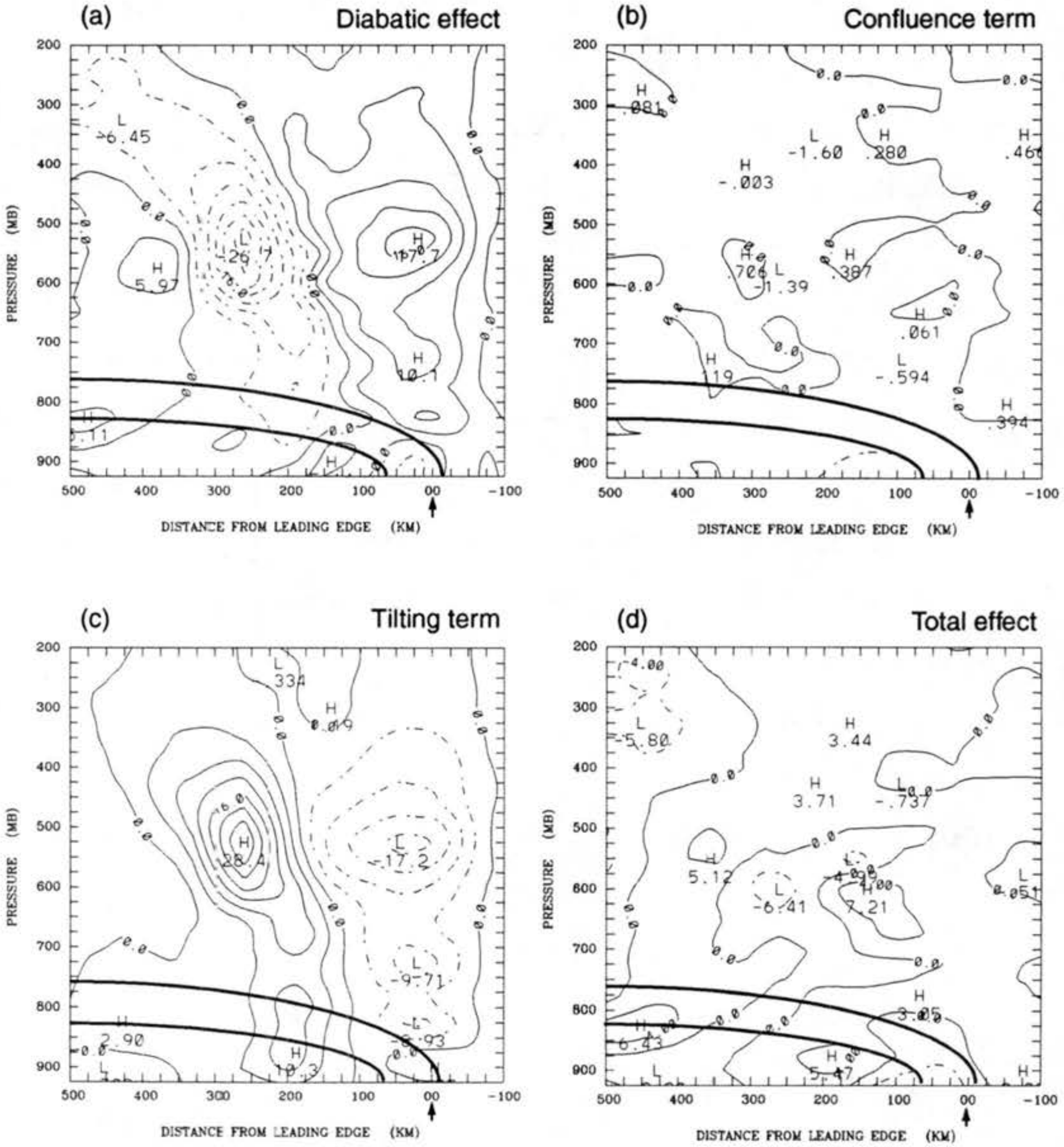

Figure 7.5: As in Fig. 7.4, except for 0300 UTC.

and frontolytic effect behind. But at the dissipating stage, weak frontogenesis was only present in a small region within the frontal zone near the surface, with frontolysis shown ahead of the leading edge and behind the system. This might help to explain why the movement of both the low level cold front and the squall line increased during the early times and decreased rapidly and almost ceased at the dissipating stage.

Chapter 8

SUMMARY

The 26-27 June PRE-STORM squall line was a slow moving mesoscale convective system followed by a low-level cold front. It was within the sounding network for most of its evolution from the developing, mature and dissipating stages. Composited rawinsonde data have been extensively used to perform heat, moisture and momentum budgets for six times at time intervals of 90 minutes. Few studies have been performed in such a long sequence of a squall line evolution due to data availability. Similarities and differences are found compared to other midlatitude and tropical squall line cases. Secondary circulation forcing and frontogenetical/frontolytical effects are also investigated to evaluate the importance of the contributions from diabatic heating.

There were generally four main relative flows within the system in the line-normal cross-section: A front-to-rear flow extending from ahead of the leading edge to upper levels to the rear of the system, a weak surface front-to-rear flow due to an overturning downdraft fed by divergence underneath the stratiform region, and a midlevel rear inflow jet, similar to the results determined from midlatitudinal and tropical cases. The basic difference from other studies was that there was a moderately strong rear-to-front flow induced by a low-level cold front present at low levels behind the system, which confined the system surface front-to-rear flow within a shallow layer near the surface. The front-to-rear flow at low levels ahead of the leading edge was much weaker throughout the evolution process compared to the 10-11 June case (Gallus and Johnson 1991), but the horizontal wind shear across the squall line within the system remained relatively strong.

During the developing and mature stages, the midlevel rear-to-front flow was not apparent and remained weak well behind the squall line. At the late mature and dissipating stages, it gradually strengthened at the back edge of the squall line and extended forward into the rear of the system, suggesting the important role played by the stratiform region. Therefore, the two rear-to-front inflows, resulting from different mechanisms, formed a deep layer of rear-to-front inflow behind the leading edge during the dissipating stage.

The relative flow structure along the squall line was nearly identical with the 10-11 June case (Gallus and Johnson 1991). At low levels behind the leading edge, the relative flow was generally dominated by northeastly flow. Southwesterly flow was dominant aloft within the system and increased toward the rear at upper levels.

Similar to many previous diagnostic results, a convergence band resulting from the front-to-rear flow and midlevel rear inflow extended rearward from low levels near the leading edge up to the rear of the system in the line-normal vertical cross-sections. At most times, the magnitudes of convergence reached their maximum at low levels around the leading edge, indicating the place of the main source of mass and moisture for system development and evolution. It gradually increased from the developing to the mature stages, and then slowly decreased during the dissipating stage. However, at midlevels behind the convective region, convergence generally increased from the developing and mature all the way to the dissipating stages, suggesting the influence of the stratiform region increased. The system rear inflow gradually strengthened and developed forward, converging more intensively with the opposing front-to-rear flow and supplying more mass and moisture to the developing mesoscale updraft and downdraft in the stratiform region. At upper levels, divergence generally dominated and its evolution with time was not large.

During the early developing stage, a narrow vertical band of upward motion corresponding to a narrow convective line was present around the leading edge over Oklahoma. Moderately strong compensating downward motion occurred ahead of and behind the system. A wide band of upward motion was noticed over Kansas where stratiform and convective regions co-existed. The squall line became symmetric during its later stages. The intensity of upward motion within the system gradually increased and reached the maximum at the mature stage. During the decaying stage, the upward motion weakened and the tilting of the system gradually increased, as the stratiform region developed. To the rear of the system, strong downward motion was evident and extended into the low levels of the system. Weak convergence and downward motion can also be noticed near tropospause above the squall line system. The evolution of vertical motion in the 26-27 June case was similar to many previous studies. Strong upward motion was present throughout almost the whole troposphere in the convective region. The peak intensity was located at middle levels between 500 and 600 hPa. In the stratiform region, upward motion at middle and upper levels was quite strong with peak values at 450 hPa. Weak upward motion was present at low levels and turned into downward at the dissipating stage.

In the 26-27 June case, the contribution to the Q_1 profiles at the developing and mature stages mainly came from the heating in the convective region. During the decaying stage, both convective and stratiform regions contributed nearly equally to the system averaged heating profiles. The heating peak was located at middle levels between 500 and 550 hPa throughout the developing and mature to the dissipating stages, considerably lower than the 10-11 June PRE-STORM squall line (400 hPa) (Gallus and Johnson 1991). It is proposed that the strength of updrafts may significantly affect the location of vertical heating peaks. The large-scale environment (Thompson et al. 1979) and the relative area covered by the convective and stratiform regions in the entire system may also be important factors contributing to the position of maximum heating.

The moisture budget clearly showed the contribution from the convective and stratiform regions at different stages. During the developing and early mature stages, a single drying peak was present at low levels around 700 hPa, much lower than the peak heating level. It reflects the fact that water vapor was condensed at low levels and the released latent heat was transported upward to the midlevels by the strong convective updraft. Between middle and low levels some drying features can still be noticed. Such a structure may be induced by two different mechanisms: (1) a midlevel drying feature generated by the trailing stratiform region, especially over the Kansas region, and (2) vertical eddy transport of water vapor within the convective region, as proposed by Dudhia and Moncrieff (1987) and Lafore et al. (1988). During the late mature and dissipating stages, a double-peak structure became very prominent. The midlevel drying peak was located at 475 hPa with a weak moistening region separating it from the low-level drying peak. The magnitudes of the midlevel drying peak remained nearly constant while the low-level drying peak gradually weakened with time. It is believed that the midlevel drying feature during the decaying stage was mainly contributed from the stratiform region.

The diagnosed precipitation rates from Q_1 and Q_2 generally underestimated the observed rates. In the convective region, the underestimation was about 20 % to 40 %, which was mainly due to resolution problem. In the stratiform region, the predicted rates were generally 0.5 to 1.0 mm h^{-1} smaller than those observed. Storage and resolution problems are believed to mainly contribute to the discrepancy.

During the developing and mature stages, the influence of the squall line on the geopotential height field was small. At the late mature and dissipating stages, a prominent, deep mesoscale low was present within the stratiform region, supporting the results of Brown (1979) and Gallus and Johnson (1992). There was also a mesohigh to the rear of the mesolow, which may be combined to explain most of the dramatic strengthening of the rear inflow at the back edge of the squall line during the dissipating stage.

In the convective region, the pressure gradient acceleration was generally directed from front to rear, with Coriolis acceleration opposing it at nearly all levels, similar to previous diagnostic studies (Sanders and Emanuel 1976; Gallus and Johnson 1992). The magnitudes of both pressure gradient acceleration and turbulent stress were smaller compared to the 10-11 June case, indicative of the weaker intensity of the 26-27 June case. But Coriolis acceleration was larger during the early stages, suggesting that it might be important during squall line's early development. The line-normal momentum flux in the convective region was generally negative, and negative wind shear was present above 600 hPa. Therefore, upgradient transport was present within most of its evolution, supporting the results shown by LeMone (1983) and Gallus and Johnson (1992). In the stratiform region during the dissipating stage, positive momentum flux can be seen at all levels, along with negative wind shear above 650 hPa, the momentum flux transport was downgradient.

The contribution of diabatic heating/cooling effect to secondary circulation forcing and frontogenetical/frontolytical effects was investigated using diagnosed Q_1 data. Above the low-level cold front within the system, compared to geostrophic stretching deformation and geostrophic shearing deformation terms, the contribution of the diabatic effect to secondary circulation forcing was about one order of magnitude larger, indicating the important role the diabatic effect played in the mesoscale circulation. At low levels around the cold front, the three terms contributed nearly equally to the forcing. In the frontogenesis equation, although the diabatic effect was more than one order of magnitude larger than the confluence term, it was strongly opposed by the tilting term within the squall line. Therefore, the feedback of the squall line to frontogenesis appeared to be small above the cold front, although the low-level cold front served as a triggering mechanism for the MCS. During the early stages within the frontal zone near the surface, frontogenesis occurred around and ahead of the leading edge, with frontolysis present behind. During the decaying stage, frontogenesis only occurred in a small region within the frontal zone, while frontolysis took place ahead and behind. This feature may help to explain why the movement of both the low-level cold front and the squall line increased during the early stages and decreased rapidly and almost ceased at the dissipating stage.

As in other budget studies using rawinsonde data, resolution is still a problem in the 26-27 June case. The small width of the squall line at early stages, unevenly distributed composited sounding stations due to slow movement of the squall line, affected the accurate calculation of ω, Q_1 , Q_2 and other diagnostic quantities. In future mesoscale experiments, methods to composite all the rawinsonde data, radar data, wind profiler data and other available data should be developed to yield more complete and accurate data sets.

In the 26-27 June case, for the first time the heat, moisture and momentum budgets of a midlatitude frontal squall line from the developing and mature throughout the decaying stages were calculated using mesoscale sounding data. Many mesoscale features (strengthening of the midlevel RTF flow, midlevel convergence maximum, and mesolow, etc) were illustrated as the stratifrom region developed, suggesting the important role played by the stratiform region. Further research will be done on the vorticity budget to investigate the evolution of vorticity components within the convective and stratiform regions. More budget studies of other cases should be performed to show evolution of heating and moistening features in entire squall line development, determine the factors affecting the locations of vertical heating and drying peaks, explain the double drying peak structure in the Q_2 profile and illustrate the interaction of squall lines with their following low level and/or upper level cold fronts.

REFERENCE

Anthes, R. A., and D. Keyser, 1979: Tests of a fine-mesh model over Europe and the United States. *Mon. Wea. Rev.*, 107, 963–984.

Augustine, J. A., and E. J. Zipser, 1987: The use of wind profilers in a mesoscale experiment. *Bull. Amer. Meteor. Soc.*, 68, 4–17.

Balsley, B. B., W. L. Ecklund, D. A. Carter, A. C. Riddle and K. S. Gage, 1988: Average vertical motions in the tropical atmosphere observed by a radar wind profiler on Pohnpei (7° N latitude, 157 ° E longitude), *J. Atmos. Sci.*, 45, 396–405.

Barnes, S. L, 1964: A technique for maximizing details in numerical weather map analysis. *J. Appl. Meteor.*, 3, 396–409.

Barnes, S. L, 1973: Mesoscale objective map analysis using weighted time- series observations. NOAA Tech. Memo. ERL NSSL-62, Norman, OK, 60 pp.

Barnes, S. L, and K. Sieckman, 1984: The environment of fast- and slow-moving tropical mesoscale convective cloud lines. *Mon. Wea. Rev.*, 112, 1782–1794.

Brown, J. M., 1979: Mesoscale unsaturated downdrafts driven by rainfall evaporation: A numerical study. *J. Atmos. Sci.*, 36, 313–338.

Chen, Y.-L., and E. J. Zipser, 1982: The role of horizontal advection of hydrometeors in the water budget of a large squall line system. Preprints, *12th Conference on Severe Local Storms*, San Antonio, Amer. Meteor. Soc., 355–358.

Chong, M., P. Amayenc, G. Scialom and J. Testud, 1987: A tropical squall line observed during the COPT 81 experiment in west Africa. Part I: Kinematic structure inferred from dual-Dopplar radar data. *Mon. Wea. Rev.*, 115, 670–694.

Chong, M., and D. Hauser, 1989: A tropical squall line observed during the COPT 81 experiment in West Africa: Part II: Water budget. *Mon. Wea. Rev.*, 117, 728–744.

Cunning, J. B., 1986: The Oklahoma-Kansas preliminary regional experiment for the STORM-Central. *Bull. Amer. Meteor. Soc.*, 67, 1478–1486.

Dudhia, J., and M. W. Moncrieff, 1987: A numerical simulation of quasi-stationary tropical convective bands. *Quart. J. Ry. Meteor. Soc.*, 113, 929–967.

Eliassen, A., 1948: The quasi-static equations of motion. Geofys. Publ., 17, No. 3, 44 pp.

Eliassen, A., 1962: On the vertical circulation in frontal zones. Geofys. Publ. (V. Bjerknes Memorial Vol.), 24, 147–160.

Emanuel, K. A., 1979: Inertial instability and mesoscale convective systems. Part I: Linear theory of inertial instability in rotating viscous fluids. *J. Atmos. Sci.*, 36, 2425–2449.

Esbensen, S. K., J.-T. Wang and E. I. Tollerud, 1988: A composited life cycle of nonsquall mesoscale convective systems over the tropical ocean. Part II: Heat and moisture budgets. *J. Atmos. Sci.*, 45, 537–548.

Fankhauser, J. C., 1974: The derivation of consistent fields of wind and geopotential height from rawinsonde data. *J. Appl. Meteor.*, 13, 637–646.

Frank, W. M., and J. L. McBride, 1989: The vertical distribution of heating in AMEX and GATE cloud clusters. *J. Atmos. Sci.*, 46, 3464–3478.

Fritsch, J. M., C. F. Chappell and L. R. Hoxit, 1976: The use of large-s cale budgets for convective parameterization. *Mon. Wea. Rev.*, 104, 1408–1418.

Fritsch, J. M., and R. A. Maddox, 1981: Convectively driven mesoscale weather systems aloft. Part I: Observation. *J. Appl. Meteor.*, 20, 9–19.

Gallus, W. A., Jr., and R. H. Johnson, 1991: Heat and moisture budgets of an intense midlatitude squall line. *J. Atmos. Sci.*, 48, 122–146.

Gallus, W. A., Jr., and R. H. Johnson, 1991: The momentum budget of an intense midlatitude squall line. *J. Atmos. Sci.*, 49, 422–450.

Gamache, J. F., and R. A. Houze, Jr., 1982: Mesoscale air motions associated with a tropical squall line. *Mon. Wea. Rev.*, 110, 118–135.

Gamache, J. F., and R. A. Houze, Jr., 1983: Water budget of a mesoscale convective system in the tropics. *J. Atmos. Sci.*, 40, 1835–1850.

Gamache, J. F., and R. A. Houze, Jr., 1985: Further analysis of the composite wind and thermodynamic structure of the 12 September GATE squall line. *Mon. Wea. Rev.*, 113, 1241–1259.

Gao, K., D.-L. Zhang, M. W. Moncrieff, and H.-R. Cho, 1990: Mesoscale momentum budget in a midlatitude squall line: A numerical case study. *Mon. Wea. Rev.*, 118, 1011–1028.

Hertenstein, R. F. A., and W. H. Schubert, 1991: Potential vorticity anomalies associated with squall lines. *Mon. Wea. Rev.*, 119, 1663–1672.

Hoskins, B. J., 1974: The role of potential vorticity in symmetric stability and instability. *Quart. J. Ry. Meteor. Soc.*, 100, 480–482.

Houze, R. A. Jr., 1977: Structure and dynamics of a tropical squall line system. *Mon. Wea. Rev.*, 105, 1540–1567.

Houze, R. A. Jr., C.-P. Cheng, C. A. Leary and J. F. Gamache, 1980: Diagnosis of cloud mass and heat fluxes from radar and synoptic data. *J. Atmos. Sci.*, 37, 754–773.

Houze, R. A. Jr., and C.-P. Cheng, 1981: Inclusion of mesoscale updrafts and downdrafts in computations of vertical fluxes by ensembles of tropical clouds. *J. Atmos. Sci.*, 38, 1751–1770.

Houze, R. A. Jr., 1982: Cloud clusters and large-scale vertical motions in the tropics. *J. Meteor. Soc. Japan*, 60, 396–409.

Houze, R. A. Jr., 1989: Observed structure of mesoscale convective systems and implications for large-scale heating. *Quart. J. Ry. Meteor. Soc.*, 115, 425–461.

Houze, R. A. Jr., B. F. Smull and P. Dodge, 1990: Mesoscale organization of springtime rainstorms in Oklahoma. *Mon. Wea. Rev.*, 118, 613–654.

Houze, R. A. Jr., and E.N. Rappaport, 1984: Air motions and precipitation structure of an early summer squall line over the eastern tropical Atlantic. *J. Atmos. Sci.*, 41, 553–574.

Johnson, R. H., 1980: Diagnosis of convective and mesoscale motion during Phase III of GATE. *J. Atmos. Sci.*, 387, 733–753.

Johnson, R. H., and G. S. Young, 1983: Heat and moisture budgets of tropical mesoscale anvil clouds. *J. Atmos. Sci.*, 40, 2138–2147.

Johnson, R. H., 1984: Partitioning tropical heat and moisture budgets into cumulus and mesoscale components: Implication for cumulus parameterization. *Mon. Wea. Rev.*, 112, 1590–1601.

Johnson, R. H., and P. J. Hamilton, 1988: The relationship of surface pressure features to the precipitation and air flow structure of an intense midlatitude squall line. *Mon. Wea. Rev.*, 116 1444–1472.

Johnson, R. H., W, A, Gallus, Jr. and M. D. Vescio, 1990: Near-tropopause vertical motion within the trailing stratiform region of a midlatitude squall line. *J. Atmos. Sci.*, 47, 2200–2209.

Johnson, R. H., and J. F. Bresch, 1991: Diagnosed characteristics of precipitation systems over Taiwan during the May–June 1987 TAMEX. *Mon. Wea. Rev.*, 119, 2540–2557.

Johnson, R. H., 1992: Heat and moisture sources and sinks of Asian monsoon precipitating systems. *J. Meteor. Soc. Japan*, 70, 353–372.

Keyser, D. A., and D. R. Johnson, 1984: Effects of diabatic heating on the ageostrophic circulation of an upper tropospheric jet streak. *Mon. Wea. Rev.*, 112, 1709–1724.

Keyser, D. A., and M. A. Shapiro, 1986: A review of the structure and dynamics of upper-level frontal zones. *Mon. Wea. Rev.*, 114, 452–499.

Kuo, Y.-H., and R. A. Anthes, 1984: Accuracy of diagnostic heat and moisture budgets using SESAME-79 field data as revealed by observing system simulation experiments. *Mon. Wea. Rev.*, 112, 1465–1481.

Kuo, Y.-H., and R. A. Anthes, 1984: Mesoscale budgets of heat and moisture in a convective system over the Central United States. *Mon. Wea. Rev.*, 112, 1482–1497.

Lafore, J.-P., J.-L. Redelsperger and G. Jaubert, 1988: Comparison between a three-dimensional simulation and Dopplar radar data of a tropical squall line: Transports of mass, momentum, heat and moisture. *J. Atmos. Sci.*, 45, 3483–3500.

Leary, C. A., and R. A. Houze, Jr., 1979: The structure and evolution of convection in a tropical cloud cluster. *J. Atmos. Sci.*, 36, 437–457.

Leary, C. A., and R. A. Houze, Jr., 1980: The contribution of mesoscale motions to the mass and heat fluxes of an intense tropical convective system. *J. Atmos. Sci.*, 37, 784–796.

LeMone, M. A., 1983: Momentum transport by a line of cumulonimbus. *J. Atmos. Sci.*, 40, 1815–1834.

LeMone, M. A., G. M. Barnes and E. J. Zipser, 1984: Momentum fluxes by lines of cumulonimbus over the tropical oceans. *J. Atmos. Sci.*, 41, 1914–1932.

Lewis, J. M., 1975: Test of Ogura-Cho model on a prefrontal squall line case. *Mon. Wea. Rev.*, 103, 764–778.

Lin, Y. J., T. C., Wang, R. W., Pasken, H. Shen and Z. S., Deng, 1990: Characteristics of a subtropical squall line determined from TAMEX dual- Dopplar data. Part II: Dynamic and Thermodynamic structures and momentum budgets. *J. Atmos. Sci.*, 47, 2382–2399.

Luo, H., and M. Yanai, 1984: The large-scale circulation and heat sources over the Tibetan plateau and surrounding areas during the early summer of 1979. Part II: Heat and moisture budgets. Mon. Wea. Rew., 112, 966–989.

Manning, K. W., 1991: An observational and modelling study of the 26-27 June 1985 PRE-STORM mesoscale convective system. M.S thesis, Atmos. Sci. Paper No. 501, Colorado State University, Department of Atmospheric Sciences, Fort Collins, CO 80523, 108pp.

McNab, A. L., and A. K., Betts, 1978: A mesoscale budget study of cumulus convection. *Mon. Wea. Rev.*, 106, 1317–1331.

Menard,, R. D., and J. M. Fritsch, 1989: A mesoscale convective complex-generated inertially stable warm core vortex. *Mon. Wea. Rev.*, 117, 1237–1261.

Miller, J. E., 1948: On the concept of frontogenesis. *J. Meteor.*, 5, 169–171.

Moncrieff, M. W., and M. J. Miller, 1976: The dynamics and simulation of tropcal cumulonimbus and squall lines. *Quart. J. Ry. Meteor. Soc.*, 102, 373–394.

Newton, C. W., and J. C. Fankhauser, 1964: On the movements of convective storms, with emphasis on size discrimination in relation to water budget requirements. *J. Appl. Meteor.*, 3, 651–688.

Nitta, T., 1972: Energy budget of wave disturbance over the Marshall Islands during the years of 1956 and 1958. *J. Meteor. Soc. Japan*, 50, 71–84.

O'Brien, J. J., 1970: Alternative solutions to the classical vertical velocity problem. *J. Appl. Meteor.*, 9. 197–203.

Ogura, Y., and Y.-L. Chen, 1977: A life history of an intense mesoscale convective storm in Oklahoma. *J. Atmos. Sci.*, 1458–1476.

Ogura, Y., and M.-T. Liou, 1980: The structure of a midlatitude squall line: A case study. *J. Atmos. Sci.*, 37, 553–567.

Ogura, Y., and D. Portis, 1982: Structure of the cold front observed in SESAME-AVE III and its comparison with the Hoskins-Bretherton frontogenesis model. *J. Atmos. Sci.*, 39, 2773–2792.

Orlanski, I., and B. B. Ross, 1984: The evolution of an observed cold front. Part II: Mesoscale dynamics. *J. Atmos. Sci.*, 41, 1669–1703.

Reed, R. J., and E. E. Recker, 1971: Structure and properities of synoptic-scale wave disturbances in the equatorial western Pacfic. *J. Atmos. Sci.*, 28, 1117–1133.

Riehl, H., and J. S. Malkus, 1958: On the heat balance in the equatorial trough zone. Geophysica, 6, 503–538.

Rutledge, S. A., and R. A. Houze, 1987: A diagnostic modeling study of the trailing stratiform region of a midlatitude squall line. *J. Atmos. Sci.*, 44, 2640–2656.

Rutledge, S. A., R. A. Houze, M. I Biggerstaff and T. Matejka, 1988: The Oklahoma-Kansas mesoscale convective system of 10-11 June 1985: Precipitation structure and single-Dopplar radar analysis. *Mon. Wea. Rev.*, 116, 1409–1430.

Rutledge, S. A., 1989: A severe frontal rainband. Part IV: Precipitation mechanisms, diabatic processes and rainband maintenance. *J. Atmos. Sci.*, 46, 3570–3594.

Rutledge, S. A., 1991: Middle latitude and tropical mesoscale convective systems. *Rev. Geophys.*, (*Supplement*) 29, 88–97.

Sanders, F., 1955: An investigation of the structure and dynamics of an intense surface frontal zone. *J. Meteor.*, 12, 542–552.

Sanders, F., and R. J. Paine, 1975: The structure and thermodynamics of an intense mesoscale convective storm in Oklahoma. *J. Atmos. Sci.*, 32, 1563–1579.

Sanders, F., and K. Emanuel, 1977: The momentum budget and temporal evolution of a mesoscale convective system. *J. Atmos. Sci.*, 34, 322–330.

Sawyer, J. S., 1956: The vertical circulation at meteorological fronts and its relationship to frontogenesis. Proc. Roy. Soc. London, A234, 346–362.

Shapiro, M. A., 1981: Frontogenesis and geostrophically forced secondary circulations in the vicinity of jet stream-frontal zonal systems. *J. Atmos. Sci.*, 38, 954–973.

Shapiro, M. A., 1983: Mesoscale weather systems of the central United States. The National STORM program: Scientific and Technological Bases and Major Objectives, R. A. Anthes, Ed. University Corporation for Atmospheric Research. Boulder, Colorado, 3.1–3.77.

Smull, B. F., and R. A. Houze, Jr., 1987: Dual-Dopplar radar analysis of a midlatitude squall line with a trailing region of stratiform rain. *J. Atmos. Sci.*, 44, 2128–2148.

Smull, B. F., and R. A. Houze, Jr., 1987: Rear inflow in squall lines with trailing stratiform precipitation. *Mon. Wea. Rev.*, 115, 2869–2899.

Smull, B. F., and J. A. Augustine, 1989: Structure and environment of a non-squall mesoscale convective complex observed during PRE-STORM. *24th Conf. onRadar Meteorology*, Tallahassee, Florida, 502–505.

Srivastava, R. C., T. J. Matejka and T. J. Lorello, 1986: Doppler radar study of the trailing anvil region associated with a squall line. *J. Atmos. Sci.*, 43, 356–377.

Stumpf, G. J., 1988: Surface pressure features associated with a mesoscale convective system in O. K. PRE-STORM. M.S. thesis, Colorado State University, Dept. of Atmos. Sci., 148pp.

Tao, W.-K., and S.-T. Soong, 1986: A study of the response of deep tropical clouds to mesoscale processes: Three-dimensional numerical experiments. *J. Atmos. Sci.*, 43, 2653–2676.

Thompson, R. M., Jr., S. W. Payne, E. E. Recker, and R. J. Reed, 1979: Structure and properities of synoptic-scale disturbances in the intertropical convergence zone of the estern Atlantic. *J. Atmos. Sci.*, 36, 53–72.

Tollerud, E. I., and S. K., Esbensen, 1985: A composite life cycle of nonsquall mesoscale convective systems over the tropical ocean. Part I: Kinematic fields. *J. Atmos. Sci.*, 42, 823–837.

Trier, S. B., D. B. Parsons and J. H. E. Clark, 1991: Environment and evolution of a cold-frontal mesoscale convective system. *Mon. Wea. Rev.*, 119, 2429–2455.

Wang, T. C., Y. J. Lin, R. W. Pasken and H. Shen, 1990: characteristics of a subtropical squall line determined from TAMEX dual-Dopplar data. Part I: Kinematic structure. *J. Atmos. Sci.*, 47, 2357–2381.

Webster, P. J., and G. L. Stephens, 1980: Tropical upper-tropospheric extended clouds: Inferences from winter MONEX. *J. Atmos. Sci.*, 37, 1521–1541.

Weisman, M. L., and J. B. Klemp, 1982: The dependence of numerically stimulated convective storms on vertical wind shear and buoyancy. *Mon. Wea. Rev.*, 110, 504–520.

Yanai, M., S. Esbensen and J. Chu, 1973: Determination of bulk properities of tropical cloud clusters from large-scale heat and moisture budgets. *J. Atmos. Sci.*, 30, 611–627.

Zhang, D.-L., and K. Gao, 1989: Numerical simulation ofan intense squall line during 10-11 June 1985 PRE-STORM. Part II: Rear inflow, surface pressure perturbations and stratiform precipitation. *Mon. Wea. Rev.*, 117, 2067–2094.

Zhang, D.-L., K. Gao and D. B. Parsons, 1989: Numerical simulation of an intense squall line during 10-11 June 1985 PRE-STORM. Part I: Model verification. *Mon. Wea. Rev.*, 117, 960–994.

Zipser, E. J., 1977: Mesoscale and convective-scale downdrafts as distinct components of squall line structure. *Mon. Wea. Rev.*, 105, 1568–1589.